UNIVERSITÀ DEGLI STUDI DI PADOVA

UNIVERSITÀ DEGLI STUDI DI PADOVA

DIPARTIMENTO DI SCIENZE CHIMICHE
CORSO DI LAUREA MAGISTRALE IN SCIENZA DEI MATERIALI

Tesi di Laurea Magistrale in
Scienza dei Materiali

Recycling Carbon-based Wastewater Filters for Hydrogen Storage: a sustainable approach

Relatore: Chiar.ma Prof.ssa Antonella Glisenti
Controrelatore: Chiar.mo Prof. Christian Durante

Laureanda: Chiara Pierantoni
Matricola: 2024131

ANNO ACCADEMICO 2022-2023

CONTENTS

ABSTRACT

Looking at the energy mix in recent years, it becomes clear that there is a need to make an energy transition towards renewable sources, especially in the transportation sector. Hydrogen, carrying high gravimetric energy density and being non-pollutant and regenerative in nature, presents itself as the perfect candidate for substituting fossil fuels and addressing the fluctuations of natural energy sources, acting as an energy vector. However, the implementation of an energy system based on hydrogen ("Hydrogen Economy") is impaired by some technical difficulties, regarding, most of all, its storage. As a matter of fact, hydrogen is characterized by an extremely low volumetric energy density, which requires the development of advanced techniques for its storage and transportation. Compared to traditional compressed and liquified hydrogen, storage in solid state materials has shown to be more effective and safer, while also optimal for mobile applications. Among all the materials studied for this application, activated carbons (ACs) have sparked a lot of interest due to their extremely high surface area and porosity, along with them being inexpensive and having good availability for industrial purposes. Additionally, they show higher adsorption reversibility when compared to other studied materials like metal hydrides. In particular, this research work focused on a particular type of AC, recycled from wastewater filters, which was studied to evaluate its performance in the storage of hydrogen. For this purpose, different parameters were investigated for the optimization of this material. First, the influence of granulometry was investigated with samples ground at different particle sizes. A chemical activation with KOH was performed to increase the spent activated carbon's specific surface area (SSA), and, lastly, a doping process was performed to introduce N heteroatoms using urea as a nitrogen precursor. For all samples, extensive analysis of the textural parameters was performed by gas adsorption, while hydrogen uptake measurements were performed to evaluate the material's performance in H_2 storage.

Chapter 1 presents a brief overview on Hydrogen Storage and ACs, followed by an in-depth explanation of the gas adsorption mechanism and its functionality in the characterization of the texture of porous solids. Chapter 2 is dedicated to the experimental procedures followed and the instrumentation used for the characterization of the materials. Chapter 3

presents the results relative to the characterization analyses, while Chapter 4 presents the final results obtained with the hydrogen uptake measurements.

1 INTRODUCTION

1.1 A brief overview on Hydrogen Storage and Active Carbons

1.1.1 Hydrogen Economy

Nowadays, the energy sector is facing several challenges, including global rising energy consumption, depleting reserves at an alarming rate, North-South disparities in energy supply, environmental hazards related to climate change, and the possibility of geopolitical war as a result of reliance on fossil fuels and nuclear energy.

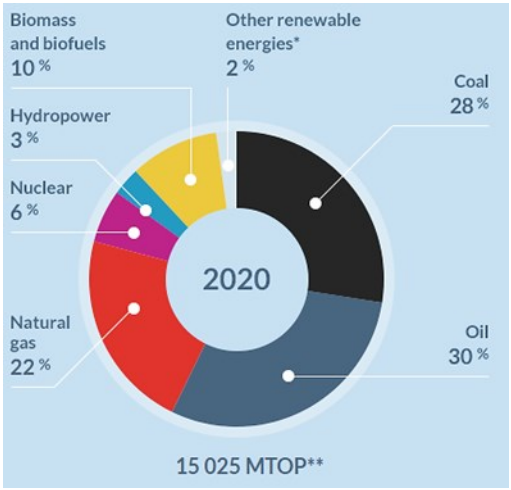

Figure 1.1: International Energy Agency (IEA) energy sources mix used in 2020 [1].

As shown in **Figure 1.1**, fossil fuels continue to play the main role in the world's energy demand. Nevertheless, the limits and inadequacy of non-renewable primary energy carriers like uranium, natural gas and oil in a long-term perspective are predictable given the steady increase in energy consumption due to the growing population and evolving lifestyles. In particular, world gross domestic product (GDP) grew by a factor of 23 in the twentieth century and resource use rose by a factor of eight (UNEP 2011 [2]); as a result, these resources are expected to last for a few decades at the estimated usage rates [3]. The use of fossil fuels has seriously impacted the environment and, therefore, has increased interest in clean and sustainable energy sources. Undoubtedly, there will be a growing need in the

upcoming decades to utilize renewable resources at an ever-increasing rate. It must also be taken into account that energy production from solar or wind is based on natural factors such as sunlight and wind patterns, which are not constant or plannable. The fluctuating nature of renewable energy, such as solar, wind, and hydropower, poses challenges for maintaining a stable and reliable power supply. The inconsistency can result in mismatches between the supply and demand of energy, resulting in complications like intermittency: electricity may not be available when it's most needed, and there may be a surplus energy production during periods of low demand [4]. In this context, hydrogen, because of its outstanding properties, emerges as a promising solution acting as an energy carrier or storage medium [5]. A hypothetical idea of a system where hydrogen is the principal energy carrier is called the Hydrogen Economy or Hydrogen Energy System [6]. John Bockris was the first person to use the term "hydrogen economy" during his presentation in 1970 at General Motors (GM) Technical Center, and an illustration of this can be observed in **Figure 1.2**.

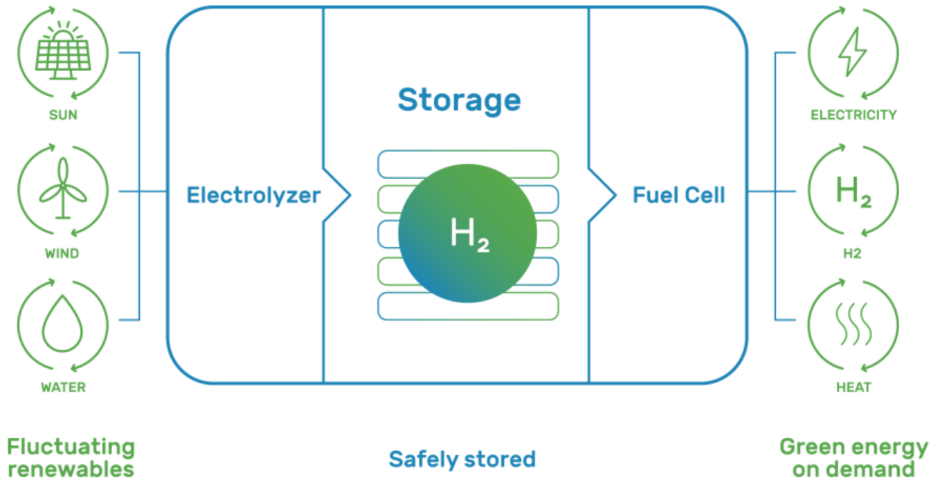

***Figure 1.2**:* Hydrogen Economy System illustration [7].

In such a system, hydrogen would be produced through electrolysis, a process that involves the splitting of water into H_2 and O_2, using electricity generated from renewable sources. Hydrogen would then act as an energy vector, playing a key role in the storage of surplus renewable energy during times of excess production and later use to generate electricity back in fuel cells or provide power for various applications when renewable sources are not actively producing energy. The interest in hydrogen as a fuel is ascribed to its remarkable attributes: it carries high gravimetric energy density, emits zero pollutants during usage, and is regenerative in nature [8]. Consequently, hydrogen is anticipated to be a highly

efficient alternative to current fossil fuels, applicable across various sectors such as transport, industrial, residential commercial and power generation [6].

In particular, the transportation sector necessitates a profound shift in fuel selection, as depicted in **Figure 1.3**, which shows that, as of 2015, 96% of the energy consumption in transport was related to the use of non-renewable sources. The urgency of this change is even more clear considering the need to align with the imperatives outlined by Europe's "Fit for 55" Initiative, which sets ambitious goals, targeting zero emissions from cars by 2035 [9].

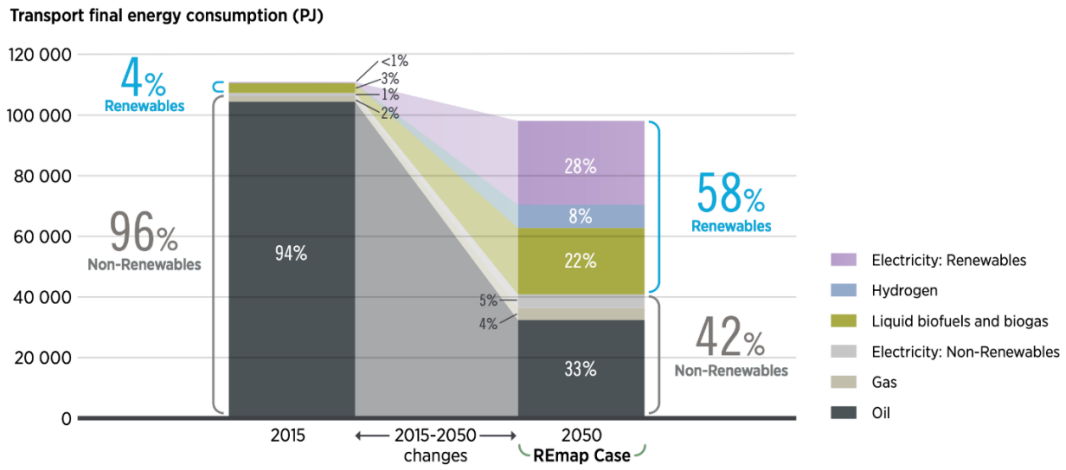

Figure 1.3: Up-to date role of fossil fuel in transportation sector; new targets for 2050 [10].

1.1.2 Hydrogen Storage

Despite hydrogen's considerable advantages, the difficulties linked to hydrogen production, storage, and transportation severely limit the spreading of these technologies [11]. In particular, hydrogen storage stands as main problem preventing a hydrogen economy system from being implemented. In order to have a full understanding of the challenges research has to tackle, we have to take a look at H_2 volumetric energy density. As pointed out in **Figure 1.4**, it is really low at standard temperature and pressure (approximately 1.3 kWh/L for 700 bar H_2 at 15°C compared to 8.8 kWh/L for gasoline), which makes storage and transit difficult. A net contrast emerges when considering instead gravimetric energy density. In fact, we can appreciate the remarkable energy content within a single kilogram of hydrogen (~120 MJ, which is around 33.3 kWh), if compared to other traditional fuels. Thus, H_2 results in an attractive option for applications where weight is a critical factor, such as in aviation, aerospace, and long-range transportation.

Thus, being a volumetrically diluted fuel when compared to traditional fossil ones, it is necessary to develop technologies which allow for hydrogen storage at both high volumetric and gravimetric energy densities [12].

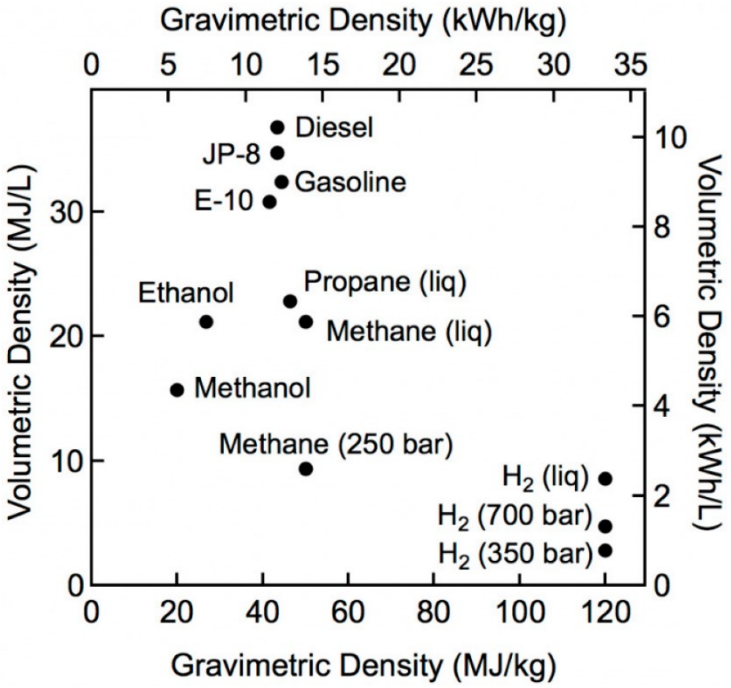

***Figure 1.4**:* Comparison of gravimetric density and volumetric density for several fuels [13].

Conventionally, hydrogen is stored as compressed gas in high pressure cylinders or as a cryogenic liquid in cryogenic containers. Due to the massive amount of energy required for hydrogen compression and the cost related to liquifying hydrogen and storing it in expensive high-pressured and cryogenic temperature tanks, solid-state storage has been deeply investigated in the last decade [11]. In addition, this approach presents significantly lower safety risks compared to compressed or liquid H_2. In solid state storage hydrogen is stored either through chemisorption in form of hydrides (Metal Hydrides, Complex Hydrides and Chemical Hydrides) or through physisorption as molecular hydrogen adsorbed on the solid surfaces of high surface area materials such as Metal-Organic Frameworks (MOFs) and porous carbons. Such materials then allow the stored hydrogen to be released whenever required by thermal stimulation or any other technique [8].

This research project was focused, in particular, on evaluating carbon-based system suitability for hydrogen storage. It is worth it to highlight that this technology holds the potential for a significant impact on the future of hydrogen-powered vehicles [14]. The current technology utilizes Hydrogen Internal Combustion Engines (Hydrogen ICE) or Hydrogen Fuel Cells (FC). In essence, both methods of converting hydrogen energy necessitate the storage

of hydrogen in quantities that guarantee satisfactory vehicle mileage [15]. Storing enough hydrogen (4-10 kg) onboard a light-duty vehicle to achieve a 500 to 800 km driving range is still a significant challenge. The U.S. Department of Energy (DOE) has set targets to achieve in hydrogen storage for onboard light-duty vehicles, material-handling equipment, and portable power applications [16]. In particular, besides energy density, hydrogen storage systems have to address requirements related to cost, durability/operability, charge/discharge rates, fuel quality, efficiency, and safety, which may limit the widespread commercialization of hydrogen vehicles. In **Table 1.1,** some of the several parameters necessaries for the storage system are reported.

Table 1.1: Technical System Targets: Onboard Hydrogen Storage for Light-Duty Fuel Cell Vehicles [17].

STORAGE PARAMETER	UNITS	2020	2025	ULTIMATE
System Gravimetric Capacity				
Usable, specific-energy from H_2 (net useful energy/max system mass)	kWh/kg (kg H_2/kg system %)	1.5 (4.5)	1.8 (**5.5**)	2.2 (**6.5**)
System Volumetric Capacity				
Usable energy density from H_2 (net useful energy/max system volume)	kWh/L (kg H_2/L system %)	1.0 (3.0)	1.3 (4.0)	1.7 (5.0)
Storage System Cost				
Storage system cost	$/kWh net ($/kg H_2)	10 (333)	9 (300)	8 (266)
Durability/Operability				
Operating ambient temperature	°C	-40/60 (sun)	-40/60 (sun)	-40/60 (sun)
Operational cycle life (1/4 tank to full)	cycles	1,500	1,500	1,500
Charging/Discharging Rates				
System fill time	min	3–5	3–5	3–5
Fuel Quality				
Fuel quality (H_2 from storage)	% H_2	Meet or exceed SAE J2719		

The DOE targets act as crucial reference points in this research, guiding the evaluation of the materials used and their potential for future industrial applications. In this study, activated carbon sourced from exhausted water filter produced from Think:Water company has been employed and its performances in hydrogen storage have been evaluated.

1.1.3 Activated Carbons and Waste-To-Treasure Approach

Activated carbon (AC) is a highly porous form of mainly amorphous carbon produced through the activation of carbonaceous materials, such as coconut shells or wood, through physical or chemical methods. It is renowned for its exceptional adsorption properties and low mass density. AC shows an impressively vast internal surface area (it can range between few hundred to over 3000 m^2/g) and a microstructure rich in micropores (< 2 nm diameter) that enable it to effectively capture and retain a wide range of molecules and pollutants from gases, liquids, and solutions. Its remarkable adsorption capacity and versatility make it a key material extensively used in many applications, including water purification, air filtration, gas separation, and the removal of impurities in various industrial processes.

Among the variety of carbonaceous materials investigated in the literature for hydrogen storage, such as carbon nanotubes (CNTs), carbon nanofibers (CNFs), or carbon nanohorns (CNHs) [8], AC caught attention due to its appealing features like being inexpensive and having good availability for industrial purposes; besides, it shows higher hydrogen adsorption compared to CNTs at almost same operating conditions, as reported by Rzepka et al. [18]. Furthermore, compared to metal hydrides, AC can desorb hydrogen at moderate temperatures and pressures (regeneration), as required by the DOE targets. In this way, activated carbon offers superior reversibility in the loading and unloading process compared to other investigated materials like metal hydrides. This is attributed to its weak interaction between the surface and hydrogen molecules characteristic of physisorption mechanisms, in contrast to the stronger interactions involved in chemisorption mechanisms found in complex and metal hydrides [8]. The hydrogen storage capacity of these materials typically ranges between 0.5-5wt% [19], and can be developed via activation treatments or doping. Activation of AC can be either physical, which consists in two consecutive thermal steps, namely pyrolysis/carbonization and successive gasification, or chemical, which instead consists of a single thermal step after impregnation of the carbon with an activating agent, such as $ZnCl_2$, NaOH or KOH. The latter strategy is the one that has proven to result in

higher surface areas for the same precursors [20]. In particular, using KOH as an activating agent is known to be among the best methods for obtaining ACs having high surface area and narrow pores [21]. Regarding doping instead, improvements in the hydrogen storage capacity of ACs have been accomplished via either doping with heteroatoms, with N and B being the most studied ones due to their effectiveness [22], or via doping with metal nanoparticles such as Pt [23] and Pd [24]. In **Table 1.2**, hydrogen storage capacity values of different pure and doped/treated ACs are compared.

***Table 1.2**:* Experimental hydrogen storage capacity values of pure and doped/treated AC [8].

Adsorbent	Hydrogen storage (wt%)	Conditions-temp, pressure	Reference
AC	0.67	303 K, 10 MPa	[25]
AC	1.4	77 K, 0.1 MPa	[26]
AC	1.6	296 K, 13 MPa	[27]
AC	4.5	77.4 K	[28]
AC	5.7	77 K, 3 MPa	[25]
AC (KOH-treated)	6.6	77 K, 4 MPa	[21]
AC (Ni-doped)	1.8	77 K, 0.1 MPa	[26]
AC (Pt-doped)	2.3	298 K, 10 MPa	[23]
AC (Pd-doped)	5.5	298 K, 8 MPa	[24]

It is of significance to underline that the storage capacity appears to be proportional to the specific surface area (SSA) and the volume of micropores. Unlike mesopores (2-50 nm) and macropores (>50 nm), micropores are directly responsible for interacting with H_2 molecules [8]. These aspects though will be discussed more in depth later in Chapter 4.

In the course of this work, a peculiar type of AC was used, extracted from exhausted water filters. As already mentioned, the very high surface area of activated carbons makes them really attractive as adsorbents for different types of pollutants, especially in water purification [29]. In particular, the carbon studied in this work was granular activated carbon (GAC) used for the dechlorination of water. This is a process in which AC acts as a reducing agent, turning chlorine into a non-oxidative chloride ion through a catalytic redox reaction [30]. Once the effectiveness of the material decreases below 80%, the filter is deemed as exhausted, and is disposed. This material was instead recovered and ground for the purpose of this work, in order to study its potential regeneration and reuse in the field of hydrogen storage, as illustrated in **Figure 1.5**.

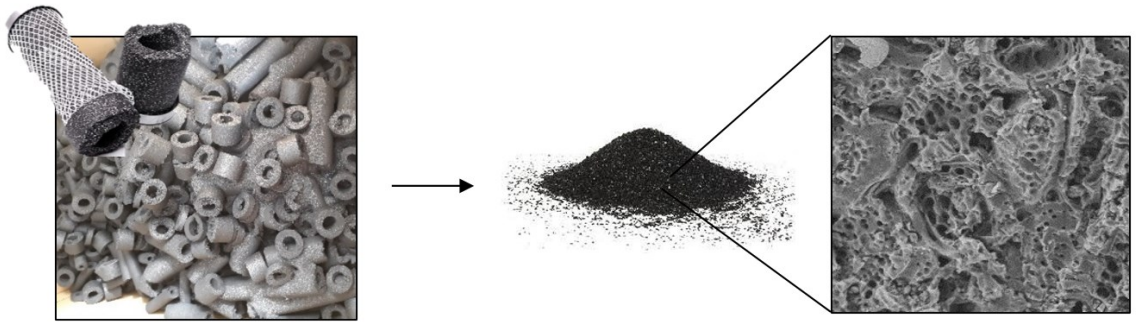

***Figure 1.5**:* Illustration of the recovery process of AC from exhausted water filters.

This "Waste-To-Treasure" approach proposes the recycle of carbon waste as low cost materials that can be converted in high added value materials leading to a low impact on the environment. This is quite relevant when considering that the disposal of processing residual requires about 0.50 €/kg, and that the amount of waste from processing filters for water purification is roughly estimated around 120 tons/year in Europe originating more than 400000 kg/year of CO_2. Thus, disposing the adsorbent may have adverse environmental impact, which should be mitigated through regeneration and reuse processes that allow for its recycling and recovery [31]. The recycled AC, also referred to Spent Activated Carbon (SAC) was studied at different particle sizes, in order to evaluate the influence of its granulometry and porosity on its hydrogen storage performance. After this first textural optimization, which also involved chemical activation of some of the samples with KOH, a successive doping process was performed to additionally improve the H_2 adsorption capacity of the material. All of these aspects will be discussed more in depth later in this work. To further highlight the attention directed towards the environmental implications of this project, it was additionally chosen to dope the studied material following a particularly green procedure. This involved doping the SAC with N heteroatoms using urea as a nitrogen precursor, which is indeed an available, non-toxic and low-cost reagent [32].

1.2 Gas Adsorption

1.2.1 Preliminary definitions

Gas Adsorption is a well-established technique for the characterization of the texture of porous solids and fine powders. In 1985 IUPAC [33] classified pores according to their size as:

- macropores: pores with width exceeding 50 nm;
- mesopores: pores of width between 2 nm and 50 nm;
- micropores: pores with widths equal or under 2 nm.

A further classification [34] divided the last of these into ultramicropores (width < 0.7 nm) and supermicropores (width > 0.7 nm). Gas adsorption is one of the most used tool for characterizing the Specific Surface Area (SSA) and Pore Size Distribution (PSD) for pores with sizes comprised between 0.3 and 300 nm.

In general, adsorption is defined as the enrichment of molecules, atoms or ions in the vicinity of an interface, and in the case of gas/solid systems this happens in the vicinity of the solid surface and outside the solid structure. The adsorptive is defined as the adsorbable substance in the fluid phase, while it's called adsorbate after being adsorbed on the surface of the solid, which is the adsorbent instead. Adsorption can be physical or chemical, in which cases it is respectively called physisorption or chemisorption. While the latter involves the formation of a chemical bond between the adsorbate and a specific site of the adsorbent, and will not be dealt with in this thesis work, physisorption is a general phenomenon, that occurs whenever an adsorbable gas is brought in contact with the surface of an adsorbent. Being based on weak van der Waals interactions (dispersion forces, ion-dipole, ion-induced dipole, dipole-dipole and quadrupole interactions), with adsorption enthalpies of around 5-40 kJ/mol, differently from of chemical bonds (40-800 kJ/mol), physisorption is most suitable for surface area determination due to the following reasons:

- low heats of adsorption result in no disruption of the structure of the surface during adsorption measurement;
- more than one layer of adsorbate can be adsorbed, unlike chemisorption;
- pore size distribution and pore volume can be calculated since pores can be completely filled by the adsorptive;
- equilibrium is achieved rapidly since the kinetics of these processes is fast, due to them being non-activated;

- physisorption is fully reversible, making it possible to study both the adsorption and the desorption process, defined as the converse process in which the amount of adsorbed gas progressively decreases;
- physical interactions are non-specific, as such, the whole surface can be calculated instead of specific active sites.

The amount adsorbed on a solid surface W depends on the temperature T, pressure p and the gas/surface interaction potential E. Usually, the quantity adsorbed is measured at constant T, and as such, a plot of W versus p is referred to as the sorption isotherm of a particular gas-solid interface. The different processes that happen during an adsorption measurement are represented in **Figure 1.6.** As the gas is first brought in contact with the surface, at low pressures, the gas molecules start being physically adsorbed on the most energetically favourable sites of the surface. In this first stage, micropores tend to be filled first, since the pore walls are so close that their adsorption potentials overlap, generating potential wells which gas molecules are strongly attracted to. As gas pressure is increased in stage 2, the molecules keep covering the surface and the walls of meso and macropores until one monolayer is statistically formed. This is the point in which the surface area of the adsorbent is generally calculated. In stage 3, raising the pressure over this point causes the beginning of multi-layer coverage and the gradual filling of pores, starting from the smaller mesopores. At stage 4, a further pressure increase results in the complete coverage of the sample surface and the filling of all pores, at which point the pore size distribution of the material can be studied. The sorption behavior of micropores is very different from the one present in meso- and macropores. As mentioned above, micropores are so small that the potential curves of the pore walls overlap. The sorption behavior is then dominated only by the interaction between gas molecules and pore walls, and the resulting micropore filling process is thought to be a continuous volume filling process [35]. In the case of mesopores and bigger pores instead, since the pore walls are farther apart, the pore potential is not dominant in the core of the pores. The adsorption behavior then depends not only on fluid-walls attraction, but also on the interactions between fluid molecules. This results in multi-layer adsorption and in these pores being filled through capillary (pore) condensation. This is a phenomenon in which gas condenses to a liquid-like state in pores at a pressure less than the bulk fluid's saturation value P_0, and it is an example of a shifted bulk transition under the influence of attractive fluid-wall interactions [36], [37].

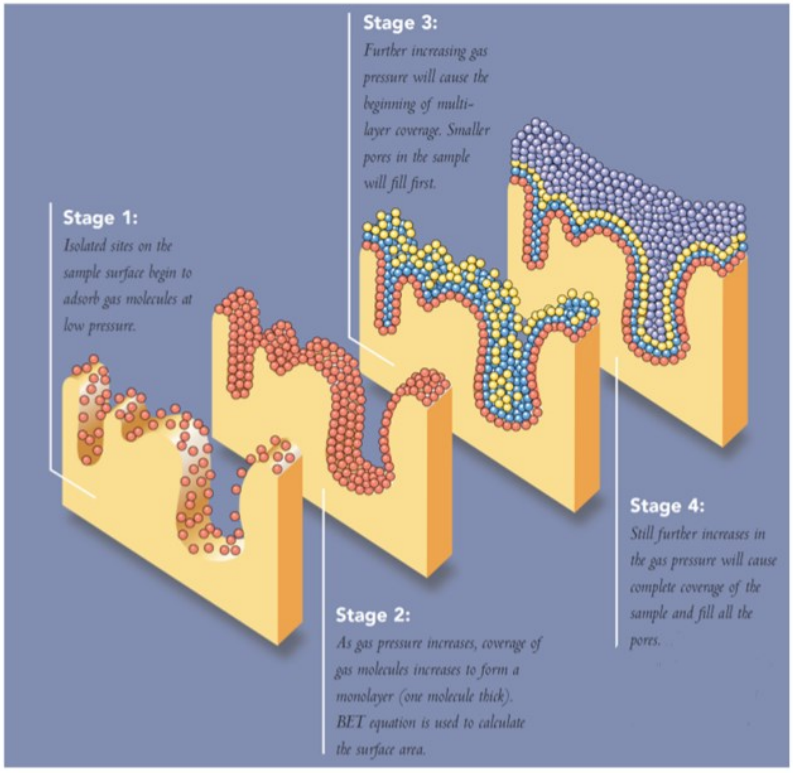

Figure 1.6: Illustration of the various stages of gas adsorption on an adsorbent surface [38].

1.2.2 Classification of adsorption isotherms

In 1985 IUPAC [33] proposed a classification of six adsorption isotherms, based upon an extensive literature survey performed by Brunauer, Deming, Deming and Teller [39]. This was successively refined in 2015 [34], as illustrated in **Figure 1.7**, after the identification of new types of isotherms. All of these reflect the points discussed in the previous paragraph and are related to the pore structure of the material. The isotherms, as suggested by IUPAC, are displayed in graphical form with the amount adsorbed plotted against the equilibrium relative pressure (p/p^0), where p^0 is the saturation pressure of the pure adsorptive at the operational temperature. The reversible Type I isotherms are observed in the case of microporous solids with relatively small external surfaces, as it is the case for some activated carbons. The curve is concave to the p/p^0 axis, with a steep uptake at very low relative pressure, and the amount adsorbed approaches a limiting value as $p/p^0 \rightarrow 1$. This is due to micropore filling, which occurs at very low pressure due to the narrow pore width resulting in high adsorption potential and enhanced adsorbent-adsorptive interactions. Once this

process is completed, the limiting value is reached, as this is governed by the accessible micropore volume rather than by the internal surface area. For nitrogen and argon adsorption at 77 K and 87 K, Type I(a) isotherms are obtained with materials having mostly narrow micropores (width ≤ 1 nm), while Type I(b) are associated with a broader pore size distribution, including wider micropores and narrow mesopores (width ≤ 2.5 nm).

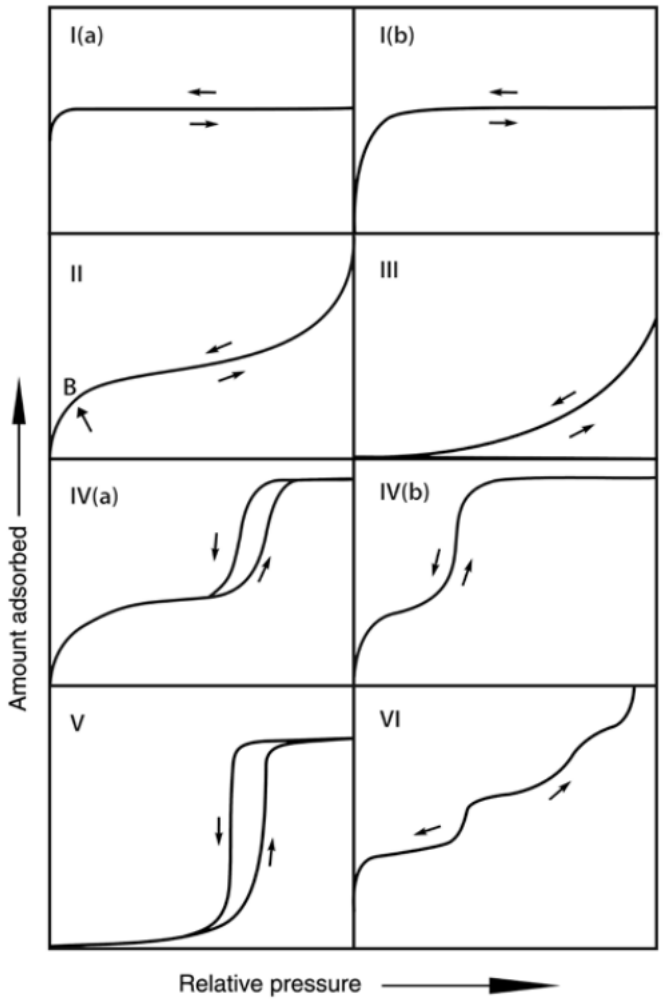

Figure 1.7: Classification of physisorption isotherms [34].

Reversible Type II isotherms are typically obtained in the case of non-porous or microporous adsorbents. Its shape is characterized by an apparently unlimited increase as $p/p^0 \rightarrow 1$, which is the result of unrestricted monolayer-multilayer adsorption that can occur in pores that are so large that they are not completely filled at saturation pressure (~ 300 nm). The inflection point or knee of the isotherm (called Point B) indicates the stage at which monolayer coverage is complete and multilayer adsorption begins to occur. A less sharp curvature is indicative of a significant amount of overlap of these two last phenomena.

The reversible Type III isotherm is convex to the p/p^0 axis in its entire range and as such does not present a Point B, indicating no identifiable monolayer formation. This is indicative of weak attractive adsorbant-adsorptive interactions, and adsorbate-adsorbate interactions playing an important role, resulting in molecules clustering around the most energetically favored sites. The amount adsorbed is finite as saturation pressure is reached.

Type IV isotherms are typical of mesoporous materials, where the adsorption behaviour is determined by both adsorbent-adsorptive and adsorbate-adsorbate interactions. The first part of the curve, analogously to the Type II, corresponds to monolayer-multilayer adsorption on the mesopore walls. This is then followed by a vertical growth associated with pore condensation, and a final saturation plateau of variable length being reached once all mesopores are filled. In the case of the Type IV(a) a hysteresis loop between the adsorption and desorption curve can be observed, which is associated with the presence of capillary condensation. This occurs when the pore width exceeds a certain critical width, which varies according to the adsorption system and temperature ($\sim$ 4 nm for nitrogen at 77 K). When this is not the case, reversible Type IV(b) isotherms are observed. These are also obtained with conical and cylindrical mesopores that are closed at the tapered end.

Type V isotherms show pore condensation and hysteresis, but with an initial part of the curve similar to Type III, indicative of weak adsorbent-adsorptive interactions.

The reversible Type VI is a special case, which represents layer-by-layer adsorption on a highly uniform non-porous surface, particularly by spherically symmetrical, non-polar adsorptives. The sharpness of the steps depends on the system on the temperature, while the step-height indicates the capacity for each adsorbed layer.

1.2.3 Adsorption hysteresis

The permanent and reproducible hysteresis loops observable in the multilayer range of physisorption isotherms are generally associated with pore condensation. This is due to either adsorption metastability or pore network effects. Different studies [40], [41] found that in an open-ended pore hysteresis is caused by the development of metastable states of the pore fluids associated with the nucleation of the liquid phase that occurs during capillary condensation transition, making this a delayed process. While adsorption involves a process of multilayer formation followed by pore condensation, desorption happens via evaporation of the pore fluid. Assuming a pore of finite length (which is always the case in real adsorbents) evaporation can occur via a receding meniscus. Therefore, since nucleation is not

involved, metastability is not expected to occur, and thermodynamic equilibration is established on the desorption stage, which represents a reversible liquid-vapour transition.
In more complex pore structures, hysteresis can result from network effects and pore blocking. This is the case for wide pores that access the surface only through narrow necks (e.g. ink-bottle pores). During desorption, the pore will remain filled until the lower vapour pressure characteristic of the neck is reached. The desorption branch can therefore provide useful information on the size distribution of pore necks. Studies [36], [37], [42] have revealed that if the neck diameter is smaller than a critical size, which is 5-6 nm for nitrogen at 77 K, the mechanism of desorption from larger pores involves cavitation. This phenomenon consists in the spontaneous nucleation and growth of gas bubbles in the metastable condensed fluid, determined by the tensile strength of the capillary condensed liquid. Because of the tensile strength effect (TSE) macroscopic meniscus cannot exist below a certain mechanical stability limit and therefore spontaneous evaporation of the pore liquid occurs. This results in the desorption curve closing at a fixed p/p^0 value depending on the specific adsorptive and temperature (around 0.4-0.5 for nitrogen at 77 K), and therefore being of no use for the determination of information about the pore neck size.
Figure 1.8 shows the types of hysteresis loops identified by IUPAC related to the pore structure and adsorption mechanism.

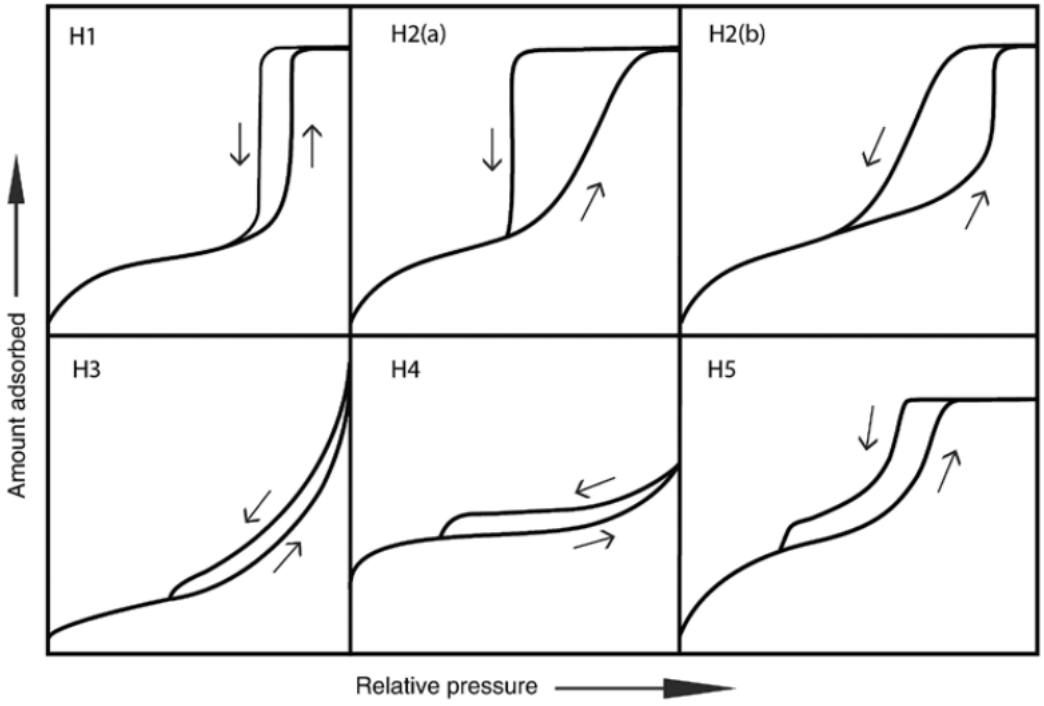

Figure 1.8: Classification of hysteresis loops [34].

The Type H1 loop is characteristic of materials with a narrow range of uniform mesopores, and the steepness of the curve indicates the delayed condensation on the adsorption branch. Type H2 are instead observed in more complex pore structures, where network effect become more important. The steep desorption branch of H2(a) loops is due to either pore blocking associated to a narrow range of pore necks or cavitation. The reduced steepness in Type H2(b) is instead indicative of a larger distribution of the pore neck sizes. Type H3 loop is characterized by a Type II adsorption isotherm and a lower limit of the desorption branch caused by cavitation. Such loops are obtained with non-rigid aggregates of plate-like particles or in the case of materials with macropores which are not completely filled with pore condensate. The same abrupt ending of the desorption loop due to cavitation is observed in Type H4 loop, where the adsorption branch is a composite of Types I and II. This is generally the case for micro-mesoporous carbons. Cavitation is also present in Type 5H loop, which has an unusual and distinct shape associated with the presence of both open and partially closed mesopores.

1.2.4 Assessment of specific surface area (SSA) and pore size distribution (PSD)

1.2.4.1 The Brunauer, Emmet and Teller (BET) Theory [43]

The Brunauer–Emmett–Teller method is the most widely used procedure for evaluating the surface area of porous and finely-divided materials. It was theorized by Brunauer, Emmett and Teller, who, in 1938, extended Langmuir's theory,[44] which, using a kinetic approach, was able to describe the type I isotherm with the assumption that adsorption was limited to a monolayer. With the BET theory instead, multilayer adsorption was first modelled. It is based on some assumptions regarding the solid-gas interaction: a multilayer can be formed, the heat of adsorption for the first layer is higher than successive layers, the adsorption energy must be constant on the whole surface, lateral interactions of adsorbed molecules are negligible, the adsorption energy of the layers that follow the first one is equivalent to the condensation energy, and the uppermost molecule in adsorbed stacks are in dynamic equilibrium with the vapor. If such conditions are met, it is possible to apply the BET model, which is represented by the following equation:

$$\frac{1}{W\left[\frac{p}{p^0}-1\right]} = \frac{1}{W_m C} + \frac{C-1}{W_m C}\left(\frac{p}{p^0}\right) \qquad (eq.\,1.0)$$

Where:

W = weight adsorbed;

W_m = weight adsorbed in a complete monolayer;

p = pressure of the adsorbed gas;

p^0 = gas saturation pressure;

C = BET constant, related to the strength of the interaction between the first layer and the surface. It is defined as an exponential, so C > 0.

Note that the quantities W and W_m can be rewritten as Volumes (V and V_m), Number of molecules (N and N_m) or moles n and monolayer capacity n_m

The determination of surface areas from the BET theory is a straightforward application of this equation. Plotting $\frac{1}{W\left[\frac{p}{p^0}-1\right]}$ versus $\frac{p}{p^0}$, as shown in **Figure 1.9**, will yield a straight line usually in the range $0.05 \leq \frac{p}{p^0} \leq 0.3$, which is the relative pressure range in which a complete monolayer of gas molecules is expected to be generally formed on the adsorbent's surface, before the progressive adsorption of successive layers.

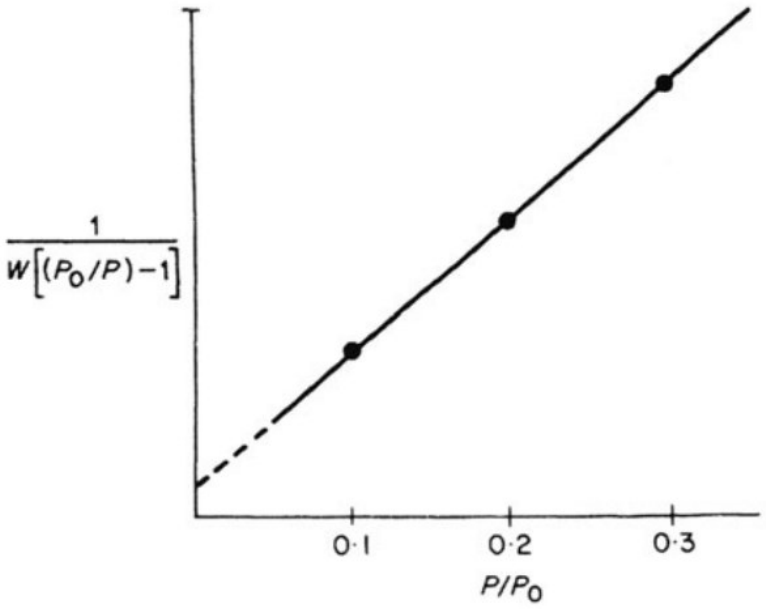

Figure 1.9: Typical BET plot [45].

The slope s and the intercept i of a BET plot are, respectively,

$$s = \frac{C-1}{W_m C} \qquad (eq.1.1)$$

$$i = \frac{1}{W_m C} \qquad (eq.1.2)$$

By solving the equation, the weight adsorbed in a monolayer W_m can obtained, which is

$$W_m = \frac{1}{s+i} \qquad (eq.1.3)$$

and the BET constant C,

$$C = \frac{s}{i} + 1 \qquad (eq.1.4)$$

The specific surface area (SSA) a_S can then be calculated as follows:

$$a_S = \frac{W_m N_A \sigma_A}{MM\ m} \qquad (eq.1.5)$$

Where:

a_S = Specific surface area, cm^2/g;

W_m = weight adsorbed in a complete monolayer, g;

N_A = Avogadro's number, mol^{-1};

σ_A = cross-sectional adsorbate area, cm^2;

MM = adsorbate molecular weight, g/mol;

m = sample mass, g.

The relative pressure range indicated above for the application of the BET theory (0.05-0.3) usually proves to be incorrect for the determination of the SSA of the SAC samples. This can be immediately noted by the calculation of negative C BET constants, which is an erroneous result, since, as mentioned above, the C constant is defined as an exponential, and as such must be a positive number. This is also quite expected and frequent when dealing with microporous materials. What happens is that the presence of very small micropores, which are filled at extremely low pressures, renders the individuation of the linear BET range much more difficult, since the monolayer-multilayer adsorption and micropore

filling are quite impossible to separate.[34] Having such energetic sites that are immediately filled puts of lot of strain on the BET model of complete monolayer formation. To remedy this problem, a particular procedure[46] was followed, which involved following these criteria:

- The quantity C should be positive;
- The BET application range should be restricted to the region of relative pressure in which the term $W(1-\frac{p}{p^0})$ continuously increases with $\frac{p}{p^0}$. This is known as Rouquerol transform, and is conveniently shown in the *ASAP 2020 Plus* software right alongside the BET plot;
- The $\frac{p}{p^0}$ value corresponding to W_m should be within the selected BET range.

1.2.4.2 Density Functional Theory (DFT) and Non-Local Density Functional Theory (NLDFT)

Density Functional Theory (DFT) is a microscopic modelling method which can describe the configuration of the adsorbed phase at the molecular level, and is considered to be one of the most reliable approach to pore size analysis over the complete nanopore range [36], [47]. Density functional theory models have been developed into powerful methods for the description of the sorption and phase behaviour of fluids confined to porous materials [34], [45]. These methods are based on the fundamental principles of statistical mechanics as applied to the molecular behaviour of confined fluids. By describing the distribution of adsorbed molecules in pores on a molecular level, they offer detailed information on the local fluid structure near the surface of the adsorbent. They allow the calculation of equilibrium density profiles of a fluid adsorbed on surfaces and in pores, from which the adsorption/desorption isotherm and other various properties can be derived for model systems. Since the fluid-solid interaction potential is dependent on the model of the pore, different pore shape models (cylinder, slit, spherical and others) have been developed for a wide variety of materials. The use of DFT and NLDFT models has proven to be of fundamental importance in overcoming the problems encountered while analyzing the pore distribution of microporous materials. What was found was that the use of classical methods based on macroscopic assumptions like the Barrett-Joyner-Halenda (BJH) method, and semi-empirical methods like the

Horvath-Kawazoe (HK) leads to an underestimation of the actual size of the pores of up to 25-30% [34], [45]. This is mainly due to the following reasons:

- The mechanism of pore filling is not correctly described, since they assume that pore filling occurs in a discontinuous way at a definite pressure characteristic of the pore's size, while this is actually thought to be a continuous process;
- In these theories it is assumed that the thermophysical properties of the strongly confined liquid-like pore fluid, do not differ from the properties of the corresponding bulk liquid, which is questionable from a statistical thermodynamics point of view for small finite systems.

As can be observed in **Figure 1.10** and **Figure 1.11**, this is an extreme simplification of the actual pore fluid behaviour.

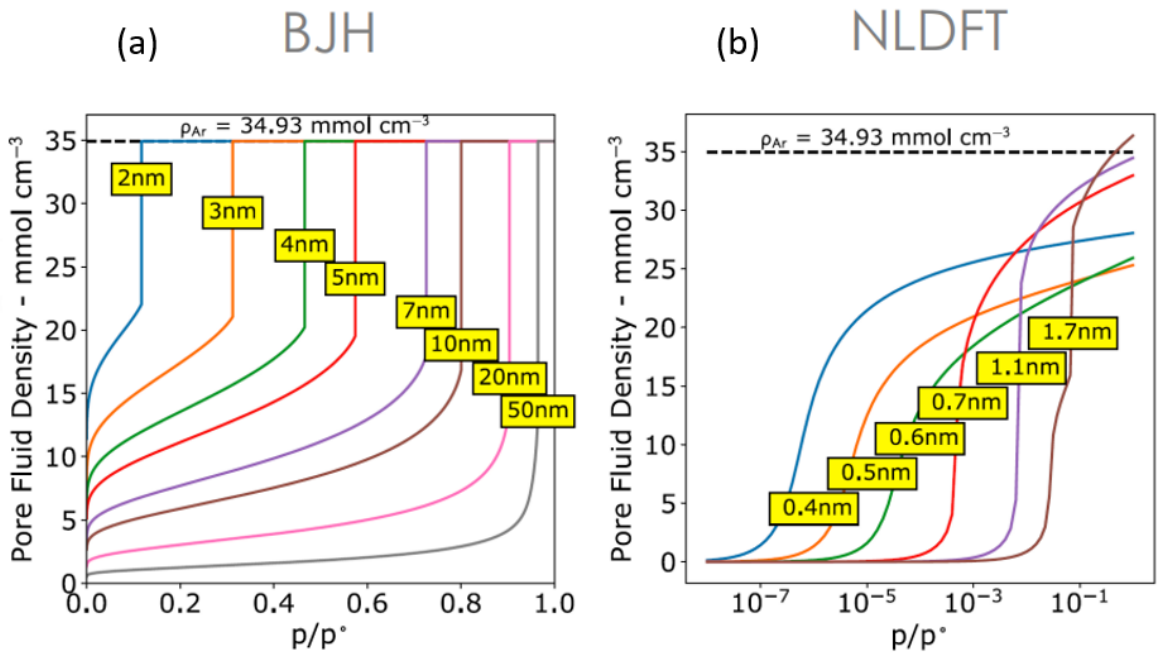

***Figure 1.10:* (a)** Pore fluid density of Ar in pores of different sizes assumed with the BJH method; **(b)** Pore fluid density of Ar in pores of different sizes calculated by NLDFT models.

Figure 1.10 clearly illustrates that, following the assumptions of the BJH method, the pore is thought to be gradually filled by the gas by increasing the pressure, up until a certain relative pressure is reached, which is characteristic for each pore size (written in yellow over each curve), where the pore is considered completely saturated and the pore fluid density is the same as the bulk Ar density. A much more correct and thorough description of the actual density profile is obtained with the NLDFT model, which shows that in none of the various pore sizes the density of the fluid settles to the bulk liquid value

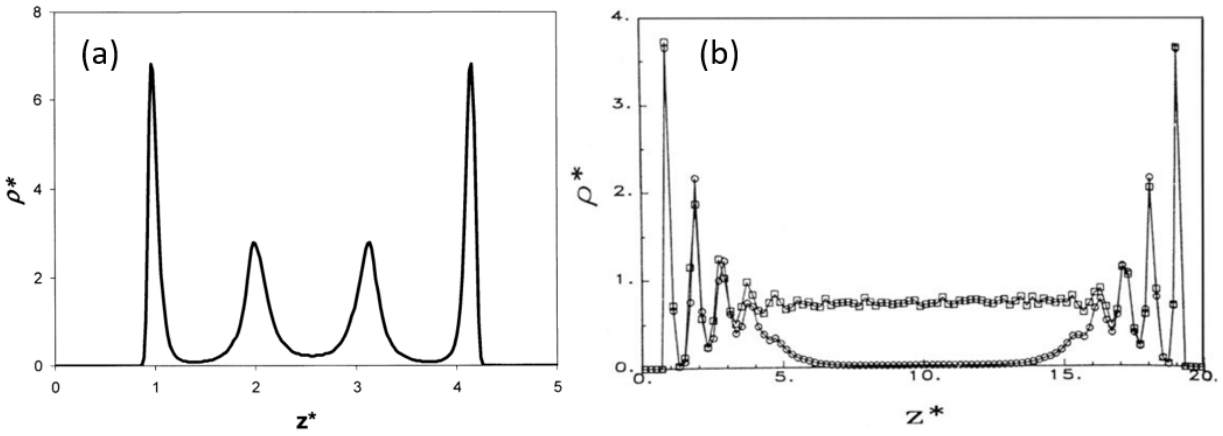

Figure 1.11: **(a)** Characteristic density profile of a fluid confined to a slit-pore of pore width 5σ, where σ is the diameter of one molecule[45]; **(b)** Characteristic density profile of coexisting gas (circles) and liquid configurations (squares) in a slit pore of width 20σ, where σ denotes the molecular diameter[45].

. In **Figure 1.11** instead, one can observe how the assumptions of the classical thermodynamical models can be valid for the case of large pores, but not for small ones. Figure (a) shows characteristic density profile of a fluid confined to a slit-pore of pore width 5σ, where σ is the diameter of one molecule. The fluid shows characteristic density oscillations, which correspond to the formation of the different layers throughout the complete narrow pore space, which demonstrates the strong potential. Additionally, one can note that only two layers can build up on each pore wall on such a small pore. In contrast, mesopores reveal a bulk-fluid like region in the core of the pore, like it can be seen in Figure (b). That is observed in the absence of the characteristic oscillations near the pore walls, which suggests that in wide mesopores the core fluid can be considered to be bulk-like. This results in the effectiveness of classical macroscopic theories like BJH in the determination of the pore size analysis for the case of mesoporous materials.

In the case of DFT and NLDFT, the local density ρ(r) of the pore fluid is calculated using the grand canonical ensemble, which gives an accurate description of the thermodynamics of the system consisting of an adsorbed fluid in equilibrium with a bulk gas phase. ρ(r) is obtained by minimizing of the correspondent grand potential function Σ[ρ(r)], which is given by the following term:

$$\Omega[\rho(r)] = F[\rho(r)] - \int dr\, \rho(r)\big(\mu - V_{ext}(r)\big) \qquad (eq.1.6)$$

Where $F[\rho(r)]$ is the intrinsic Helmholtz free energy functional in the absence of any external field and $V_{ext}(r)$ is the potential imposed by the walls. Once ρ(r) is calculated, the

adsorption isotherm can be calculated, along with other thermodynamic properties. While the fluid-fluid interaction parameters are determined as so to reproduce the bulk properties, the solid-fluid interactions parameters can then be obtained by fitting the calculated adsorption isotherm on a planar surface to the standard isotherm. In order to determine the pore size micro and mesoporous materials, the equilibrium density function ρ(r) of the fluid in the model pore is integrated to obtain different isotherms, which constitute a kernel. This is defined as a set of isotherms calculated for a set of pore sizes in a given range for a given adsorptive, which constitute the model database. The PSD can be obtained by solving the general adsorption isotherm (GAI) equation, which correlates the experimental adsorption isotherm with the kernel of the theoretical adsorption or desorption isotherms. For this purpose, the GAI is expressed in the form:

$$N\left(\frac{p}{p^0}\right) = \int_{W_{MIN}}^{W_{MAX}} N\left(\frac{p}{p^0}, W\right) f(W) dW \qquad (eq. 1.7)$$

Where

$N\left(\frac{p}{p^0}\right)$ = experimental adsorption isotherm data;

W = pore width;

$N\left(\frac{p}{p^0}, W\right)$ = kernel of theoretical isotherms in pores of different widths;

$f(W)$ = pore size distribution function.

Since the equilibrium density profiles are known for each pressure along the isotherm, no assumption has to be made regarding the pore filling mechanism, which results in these models being applicable for both micro and mesopores. However, this type of analysis is only useful if the given experimental adsorptive/adsorbent system is compatible with the chosen DFT/NLDFT kernel. In fact, as said before, each kernel is specific for a specific adsorptive/adsorbent, temperature, pore shape, and other factors, which, if are not matched properly with the experimental isotherms, could lead to significant error in the determination of PSD. In contrast with the DFT, which fails to take into account the short-range correlations in narrow, the NLDFT provides a much more accurate description of this case and of the strong oscillations characteristic of the density profile of a fluid at a solid fluid interface, as shown previously in **Figure 1.11**. Despite this, conventional NLDFT models pose a problem in the fact that generally a smooth and homogeneous surface of the pore

wall is assumed. This does not take into account the chemical and geometrical heterogeneity of the pore walls, and results in small steps in the calculated isotherm due to layering transition, which instead would not be present in heterogeneous surfaces. These drawbacks have been assessed with the introduction of two-dimensional NLDFT models[48], also called 2D-HS NLDFT model. As shown in **Figure 1.12**, the theoretical isotherms calculated with the 2D-HS model are much smoother and better represent the actual equilibrium density profile of the confined fluid.

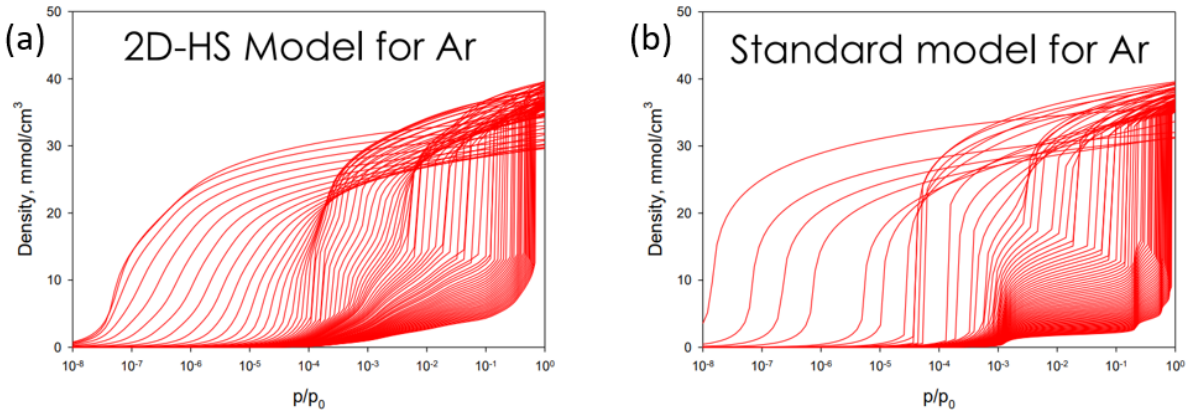

Figure 1.12: **(a)** Theoretical isotherms expressed in terms of the fluid densities calculated with the 2D-HS NLDFT model for Ar; **(b)** Theoretical isotherms expressed in terms of the fluid densities calculated with conventional DFT models for Ar.

2 EXPERIMENTAL

2.1 SAC Samples

The SACs were extracted from exhausted water filters produced from the Think:Water Company in Cittadella (PD). Thanks to Professor Andrea Santomaso and his research group of the Department of Industrial Engineering (DII) the waste material was ground to different particle size, ranging from 2.83 mm to 0.3 mm, with different ranges obtained through sieving process. A complete set of all the different samples is reported in **Table 2.1**. These untreated samples were denominated as "Raw". For the rest of this thesis work, each sample will be named after their particle size value in mm.

Table 2.1: List of available samples and relative particle size.

Particle Size (mm)
2.83-2
2-1.4
1.4-1
1-0.8
0.8-0.6
0.6-0.5
0.5-0.4
0.4-0.3
<0.3

2.2 Synthesis of the samples

2.2.1 Chemical Activation of SAC

To develop the pore network and raise the SSA of the samples, a chemical activation with KOH was performed on the samples. This method was chosen due to its lower activation temperatures and higher yield compared to other activation methods (such as chemical activation with other activation agents and physical activation, as already explained in Paragraph 1.1.3) and its efficiency in generating micropores and small mesopores into the framework of various structured carbons [49]. The activation mechanism is complex and not yet well understood, due to the large number of variables in both the experimental parameters and the reactivity of different precursors used. This process first involves solid-solid reactions, to then proceed via solid-liquid reactions. Otowa et al.[50] proposed that below 700 °C several simultaneous/consecutive reactions happen, some of which are shown in eq. 2.1-2.4, which result in H_2, H_2O, CO, CO_2, K_2O and K_2CO_3 as main products. At 400 °C KOH dehydrates to transform into K_2O (eq. 2.1), then H_2 is emitted from the reaction of carbon with H_2O (eq. 2.2). The CO_2 produced in eq. 2.3 reacts with K_2O to form K_2CO_3.

$$2KOH \rightarrow K_2O + H_2O \quad \text{(eq. 2.1)}$$

$$C + H_2O \rightarrow CO_2 + H_2 \quad \text{(eq. 2.2)}$$

$$CO + H_2O \rightarrow CO_2 + H_2 \quad \text{(eq. 2.3)}$$

$$CO_2 + K_2O \rightarrow K_2CO_3 \quad \text{(eq. 2.4)}$$

Linares-Solano et al. [51] theorized that the prominent global reaction stoichiometrically occurring between carbon and KOH to be the following:

$$6KOH + 2C \rightarrow 2K + 3H_2 + K_2CO_3 \quad \text{(eq. 2.5)}$$

Since the standard Gibbs free energy change ($\Delta G°$) of this reaction is positive at room temperature and becomes negative at ca. 570 °C, the mechanism of KOH activation starts with the reaction in eq (2.5) but then further proceeds via the reaction of metallic K with KOH to K_2O [52]. At 600 °C, the KOH is completely consumed, and the K_2CO_3, which starts forming at 400 °C (eq. 2.4 and 2.5), starts decomposing into CO_2 and K_2O at 700 °C

(eq.2.6), to ultimately disappear at 800 °C. The as-produced CO_2 can also be reduced by C to form CO at high temperatures (eq.2.7). C also reduces K_2O and K_2CO_3 to produce metallic K once temperatures are over 700 °C (eq. 2.8 and 2.9).

$$K_2CO_3 \rightarrow K_2O + CO_2 \quad \text{(eq. 2.6)}$$

$$CO_2 + C \rightarrow 2CO \quad \text{(eq. 2.7)}$$

$$K_2CO_3 + 2C \rightarrow 2K + 3CO \quad \text{(eq. 2.8)}$$

$$C + K_2O \rightarrow 2K + CO \quad \text{(eq. 2.9)}$$

Considering this, three main activation mechanisms have been accepted: (i) the pore network is generated by the etching of the carbon framework by the redox reactions between the various potassium compounds as chemical activating reagents with carbon (eq 2.5, 2.8 and 2.9); (ii) the formation of H_2O (eq. 2.1) and CO_2 (eq. 2.3 and 2.6) further contributes to the development of porosity through the gasification of carbon, i.e. physical activation (eq. 2.2 and 2.7); (iii) the metallic K obtained in eq. 2.5, 2.8 and 2.9 intercalates into the carbon lattices of the carbon matrix during the activation, and expands the C lattice, as shown in **Figure 2.1**. After washing the product to remove the intercalated metallic K and other K compounds the carbon lattice cannot return to its previous nanoporous structure, and thus high microporosity is generated.

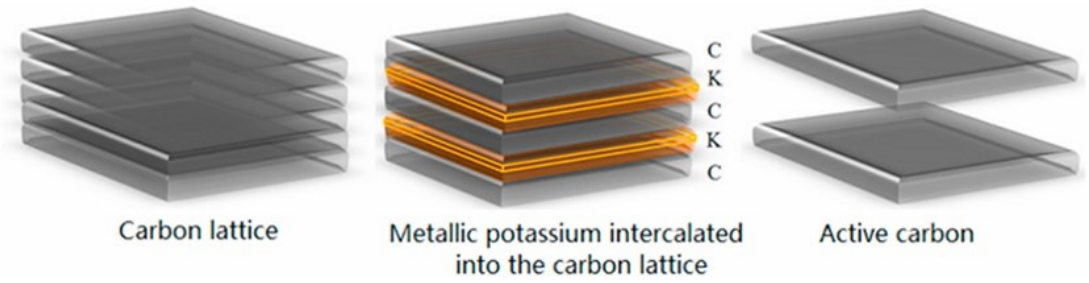

***Figure 2.1**:* Activation mechanism by the penetration of metallic K into the carbon lattices, consequent expansion of the lattices by the intercalated metallic K, and final removal of these from the carbon matrix [49].

The SACs were activated using a one-step chemical activation, as described in the work of Park et al., who, in particular, focused their attention on developing an activation process for the regeneration of spent activated carbon used in wastewater treatment, just as in the case of this study [53]. Park et al. followed a process that involved the reaction with KOH and successive washing of the product, which was performed following two different

pathways, named Case 1 and Case 2. In Case 1, the sample was washed with solely tap water, while in Case 2 an acid wash was carried out before ultimately using water, in order to investigate the effectiveness of acetic acid into the removal of the ashes that are produced during activation. This was also tried considering that some works concluded that the presence of acidic functions enhances the hydrogen storage capacity of ACs[22]. In this work, both of these different paths were followed to further test the results obtained in the mentioned article. In particular, the 1:2 AC/KOH ratio was chosen to focus on low KOH concentrations to achieve a high ratio of microporosity and minimize the amount of activating compound used [54]. Before use, the SACs were dried at 100 °C for 24 h. Successively, 2,5 g of the solid phase of the SAC was mixed with a solid phase of potassium hydroxide (Sigma-Aldrich, ≥85%, pellet), at a SAC/KOH weight ratio of 0.5. The samples were gradually heated under N_2 atmosphere at a rate of 5 °C/min until 750 °C and kept at that temperature for 1 h, and then heated up to 850 °C at a rate of 5 °C/min and held for 3 h. The chemically activated SACs obtained were then divided into two samples. For Case 1, the sample was washed using a Büchner funnel with 500 mL of tap water, repeating the process five times. The as-obtained product was denominated SAC-W. For Case 2, the sample was treated with 500 mL of 0.5 M acetic acid and then washed with 500 mL of water three times. This product was denominated SAC-AcOH instead. Both products were dried at 100 °C for 12 h.

2.2.2 Doping with N Heteroatoms

In order to improve the hydrogen adsorption capacity of the material, the chemically activated SAC was doped with N heteroatoms. The selected SAC sample was functionalized using urea as a nitrogen precursor by a two-step procedure described in the work of Quílez-Bermejo et al., illustrated in **Figure 2.2** [32]. This was chosen due to being a straightforward post-functionalization methodology that involved the use of urea, an available, non-toxic and low-cost reagent. In their study, they efficiently obtained selective doping with graphitic nitrogen for the ORR catalytic reaction, in contrast with traditionally N-doped carbon materials, that are obtained with purely graphitic N require complex methodologies and the use of N-containing carbon precursors, making it impossible to extend the synthetic route to other carbon materials. Considering the good results obtained in their work for the purpose of increasing the catalytic activity of AC for the ORR reaction, this same procedure was used to verify the effectiveness of the same doping process in increasing the hydrogen

storage capacity of the SAC. The only modification applied in this work was the use of an inert atmosphere instead of using synthetic air during the first doping step due to availability. This also allowed the evaluation of possible negative repercussions on the nitrogen functionalization of the material.

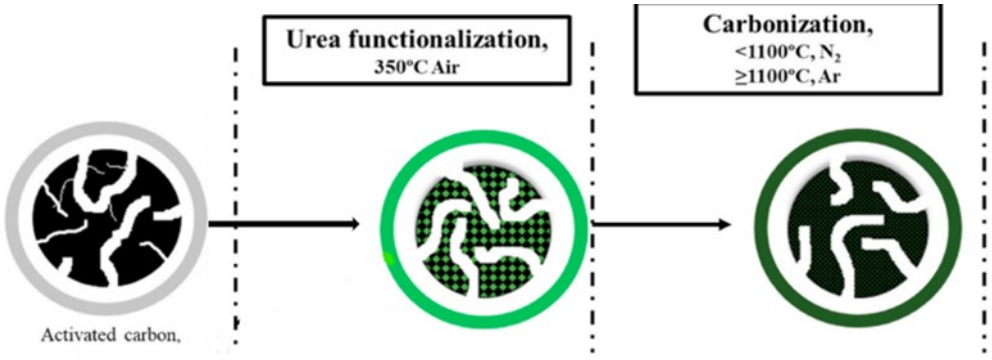

Figure 2.2: Schematic representation of the experimental procedure [32]

First, AC and urea (Sigma-Aldrich, 99.0-100.5%) were physically mixed in mass ratios 1:2 and subjected to heat treatment in a alumina boat up to 350 °C for 3 h with a heating rate of 5 °C/min under N_2 atmosphere, and then cooled to room temperature. After urea functionalization, the sample was heat treated up to 1100 °C in a tubular furnace with a heating rate of 2.5 °C/min under Ar atmosphere. In order to evaluate the N composition of the sample at various temperatures, carbonization at 900 °C was performed, in N_2 atmosphere instead of Ar.

2.3 Characterizations

2.3.1 Surface Area and Porosimetry Analysis

The specific surface area (SSA) and pore size distribution (PSD) of the samples were investigated by performing N_2 and CO_2 adsorption measurements with a Micromeritics ASAP 2020 Plus Adsorption Analyzer. The SSA was calculated by means of the Brunauer-Emmett-Teller (BET) model, while the PSD was obtained employing DFT and NLDFT models.

2.3.1.1 Micromeritics ASAP 2020 Plus-Physisorption

The ASAP 2020 Plus is a high-performance adsorption analyzer for measuring surface area, pore size, and pore volume of powders and porous materials. This instrument is especially suited for the characterization of microporous (0.35 to 2 nm) and mesoporous (2 to 50 nm) materials using gas adsorption analysis, but it can be used for a wide variety of porous and non-porous materials, such as adsorbents, catalysts, zeolites, and MOFs. All of these can be investigated with superior accuracy and resolution by employing standard methods (provided by the instrument's software) or user customized protocols. The main features of this instrument, which is illustrated in **Figure 2.3**, are the following:

- *Degas system*, comprised of two programmable stations, which allow for two simultaneous automated sample preparations.
- *Analysis station*, programmable with different specific analysis for the sample of interest.
- *p^0 sensor*, which provides p^0 values at the same conditions as the adsorption measurement and speeds up the analysis.
- *Six analysis gas inlets*, with associated vapor and helium free-space port, so as to provide an increased flexibility and automated selection of pretreatment, backfill, and analysis gases.
- *Isothermal Jacket Cold Zone Control*, designed in order to ensure a constant, accurate and reproducible thermal profile along the full length of both the sample and saturation pressure (p^0) tubes. This is achieved by installing on the analysis tube the Isothermal Jacket, which is made of a porous material that fills up with liquid nitrogen along all of its length. This allows for the maintenance of a constant cryogen level on sample tube and P_0 tubes during analysis while evaporation on cryogen occurs.
- *Dewar*, durable and refillable with N_2, for up to 60 hours' time of analysis.
- *Dual independent vacuum systems,* one associated to the analysis system and the other to the degas system, to allow simultaneous analysis and preparation of different samples.
- *Transducer system,* that yields unequalled stability, fast response, and low hysteresis for better accuracy and signal to noise improvement.
- *Manifold*, which is coated, monolithic, temperature-controlled, and made of stainless-steel, and as such provides a non-contaminating, inert surface area.

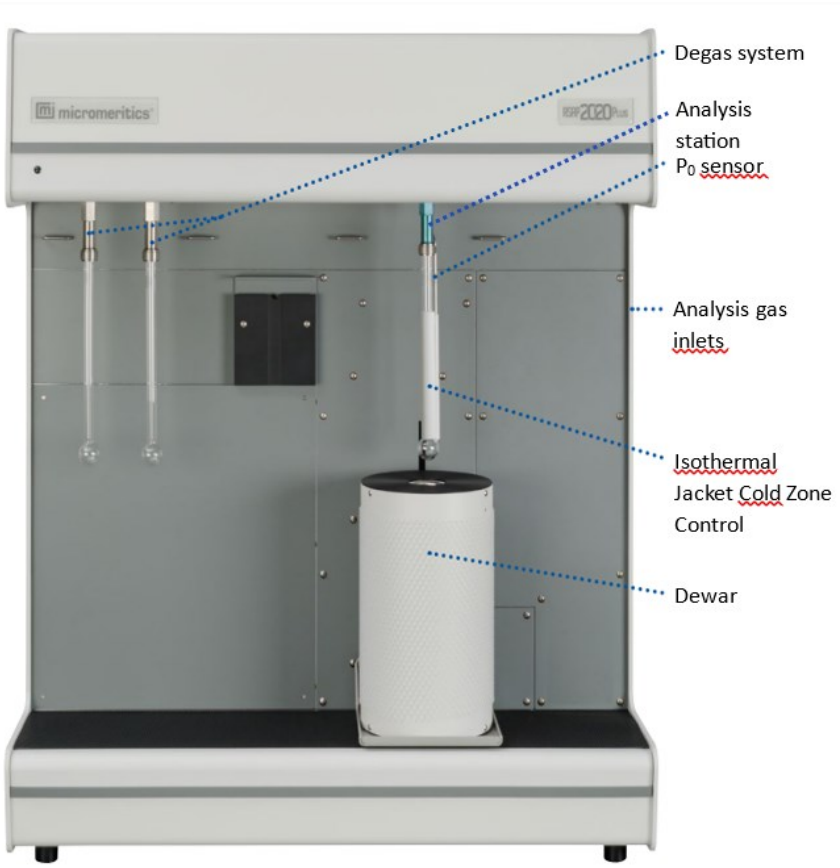

Figure 2.3: Representation of the Micromeritics ASAP 2020 Plus-Physisorption instrument [55].

In particular, as mentioned above, the ASAP 2020 Plus Physisorption instrument is particularly suited for the analysis of microporous materials. The most important features that allow for such complex and precise analysis are:

- The presence of two different pumps, a Rotary Vacuum pump and a Turbomolecular High-vacuum pump, of which the latter allows for achieving a vacuum level of less than 3.8×10^{-9} mmHg absolute pressure [56] and a relative pressure level of the order of 10^{-7}.
- A system of multiple pressure transducers that work alternatively and in unison to ensure the most precise pressure measurements. Said system is comprised of 1000, 10 and 0.1 mmHg transducers.

These features deliver accurate porosity data on pores between 0.35 and 3 nm and provide a comprehensive selection of micropore reports.[56]

The Asap 2020 is a static volumetric vacuum apparatus, and the general procedure for its measurements is the following: after vacuum is obtained, known amounts of gas are admitted stepwise through the manifold into the sample cell. At each step, the gas gets adsorbed

by the sample and the pressure falls until equilibrium is reached between the adsorbate and the remaining gas in the sample cell. Once equilibrium is achieved, the amount of gas adsorbed is measured as the difference between the amount of gas admitted and the quantity of gas filling the void volume. The adsorbed amount (or volume) is computed by applying the general gas equation. The determination of the amount adsorbed requires that the manifold volume and the void volume (or free space) is accurately known. The Free Space is the volume of the sample cell which is not occupied by the adsorbent, and is determined by expanding a non-adsorbing gas such as helium inside the sample cell prior to the analysis and by applying the general gas equation. Since the analysis tube is not completely immersed in liquid hydrogen, the Free Space is calculated at both room temperature and analysis temperature. The pressure is gradually raised up to the saturation pressure value p^0, and point-by-point the quantity of adsorbed gas is determined by the instrument to obtain the adsorption branch. After reaching saturation, the pressure is gradually decreased and the quantity of gas adsorbed is measured to obtain the desorption curve. The result of this process, which is performed at constant and controlled temperature, is a plot of the quantity adsorbed per gram of the sample versus the relative pressure p/p^0 (or alternatively the absolute pressure p). As such, the sample's isotherm adsorption and desorption curve are obtained.

2.3.1.2 Adsorption/Desorption Isotherms

The ASAP 2020 was used to determine the sample's adsorption and desorption isotherms. Nitrogen was used at its boiling temperature of 77 K (temperature maintained by filling the dewar with liquid nitrogen), with σ_A assumed to be 0.162 nm^2 (based on the assumption of a close-packed monolayer). This was chosen due to is availability and well-defined Point B usually generated with nitrogen isotherms.

The different samples are first weighed in order to have around ~ 60 m^2 in the analysis tube. This is done by simply dividing said value by the expected SSA, and ensures an optimized analysis, since surface areas that are excessively small are more difficult for the instrument to detect, but also ones that are too high could make the analysis time excessively long.

The sample is beforehand degassed in order to eliminate any polluting gases or compounds that are physically adsorbed on the surface. This is necessary to ensure a reproducible initial state of the adsorbent surface. All of the samples were degassed through high vacuum pumping at 200°C at 500 µmHg for 8 h. This temperature was chosen for being the highest

one that ACs can be heated to without causing a structural change to the structure. In order to further prevent this problem, a special heating program was used, which involved the slow removal of most of the preadsorbed water at temperatures below 100°C (90°C used), then followed by an increase of the temperature until the final outgassing temperature is reached. This is done specifically to avoid potential structural damage of the sample due to surface tension effects and hydrothermal alteration (so called "steaming").[45]

Successively, the sample is weighed again to assess the mass loss during degassing, and the analysis is performed. In the preliminary phase of the analysis, Free Spaces were measured for all of the samples using helium as a non-adsorbing gas.

A first set of N_2 adsorption and desorption measurements were first obtained for all Raw and some Activated samples using a relative pressure p/p^0 range 0.002-1, without being able to go further down in pressure because of instrument malfunction. The different pressures at which the instrument was instructed to measure the corresponding amount of gas quantity adsorbed and take as points were chosen in order to have a greater number of points in the pressure ranges where more curvature was expected. An example of such isotherms, obtained for the 2.83-2 Raw sample, can be observed in **Figure 2.4**.

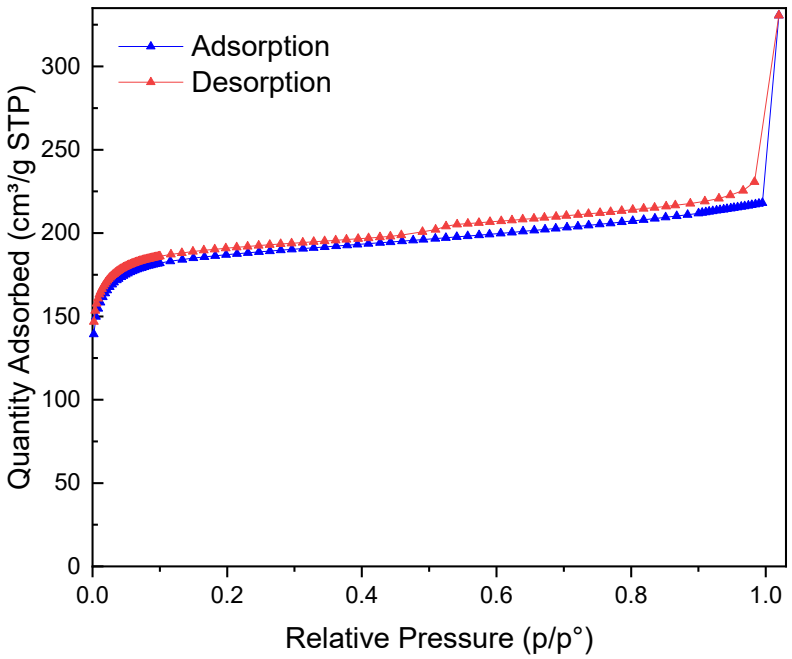

Figure 2.4: 2.83-2 Raw N_2 adsorption and desorption isotherm.

Unfortunately, these isotherms were not satisfactory, since they match mostly with the type I isotherm, but all of the first vertical part of the curve present at low relative pressures could not be obtained. This results in the loss of all the information that could be deduced

from the curve about the pore size distribution of the micropores, which are the ones that fill first at very low pressure. Furthermore, by looking at these isotherms, one can observe that the point corresponding to $p/p^0 = 1$ is a fictitious point, in which a lot of gas condensation occurs, so it's not an accurate point for measuring adsorption inside the pores and should be excluded from the analysis.

A second set of isotherms was then obtained using a different method that involved using the Dosing function in the Analysis file of the instrument; by dosing a specific small quantity of gas in the sample tube and then measuring the pressure, the instrument was able to start the analysis from relative pressures of about $10^{-6}/10^{-7}$. The dose of gas to be injected was calculated from the first set of obtained isotherms for each sample, by taking the value of quantity of gas adsorbed at 0.01 relative pressure and dividing it by 30. The Dosing function was then set to be active up until the 0.01 relative pressure value, to then be followed by a normal pressure table from 0.01 to 0.995 for adsorption, and from 0.995 to 0.1 for desorption. This method proved to be successful in particular for the activated samples, providing such isotherms as the one shown in **Figure 2.5** for the 2-1.4 A sample, in which the dots corresponding to the point were made to be smaller for clarity.

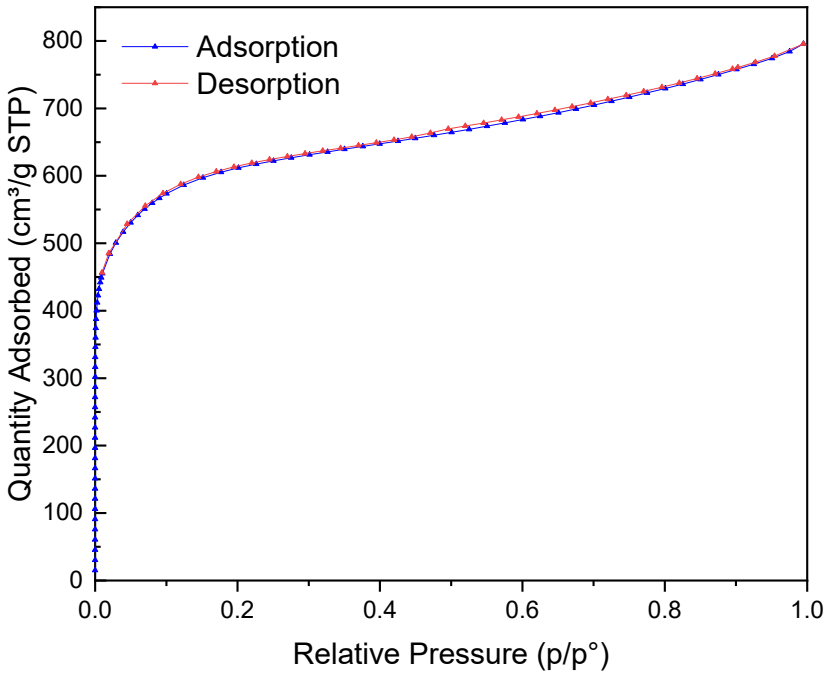

Figure 2.5: 2-1.4 A N_2 adsorption and desorption isotherm.

Unfortunately, the same could not be said for most of the Raw samples. In fact, while trying to perform the analysis, the instrument could not find the level of equilibrium necessary to acquire a point, resulting in an infinite and null analysis. This problem was first tried to be solved by "forcing" the analysis, by reducing the Equilibration Time of the instrument from 999 h to 1 h, in order to make it forcibly acquire points. This proved useful for a couple of samples, for which curves like the one in **Figure 2.5** were obtained, but not for all of the others, for which isotherms like the one reported in **Figure 2.6** were obtained.

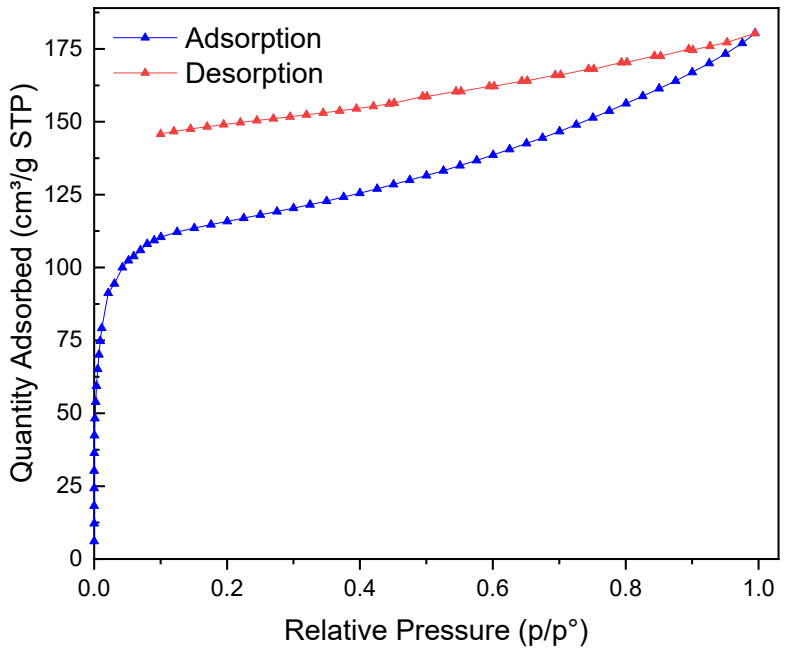

Figure 2.6: *2*-1.4 Raw N_2 adsorption and desorption isotherm.

As it can be observed, the desorption curve never reconnects with the adsorption branch, but instead straying farther and farther from it as the pressure is reduced. This renders the isotherm completely unreliable for the determination of the SSA and PSD of the samples, since this forced analysis did not obtain sufficiently equilibrated points to give a satisfactory curve. These problems are caused by the permanent quadrupole moment of the N_2 molecule, which is largely responsible for the specific interaction with a variety of surface functional groups (as for example hydroxyl groups,[57] which are expected to be found on an activated carbon surface[58]) and exposed ions,[34] and also for the formation of a well-defined monolayer on most surfaces. This quadrupolar nature of the nitrogen molecule affects both the orientation of the adsorbed gas molecule on the adsorbent surface and the pressure at which pores, in particular micropores, are filled, shifting it down to potentially

very low p values. This quadrupole-surface interaction can then be quite problematic in the case of some materials, like for microporous carbons. This is due to the presence in such materials of an often-wide distribution of pore sizes including very small micropores, in the range of ultramicropores (pore widths < 0.7 nm). These can be really hard to fill since 0.7 nm is the thickness of the N_2 molecule, and the filling of pores ranging in these dimensions occurs at relative pressures of 10^{-7} to 10^{-5}, where the rate of diffusion and adsorption equilibrium is very slow.[45] Furthermore, preadsorbed N_2 molecules near the entry of an ultramicropore could block further adsorption, and the specific interactions with surface functional groups could shift the pore filling pressure so that it is not clearly correlated with the pore size and structure. These factors lead to the time-consuming measurement and under-equilibrated adsorption isotherms shown above, which would result in erroneous result of the analysis. One other phenomenon to be considered is the low-pressure hysteresis (LPH) observed in non-rigid materials [34], [45]. While physisorption isotherms are generally expected to be completely reversible in the monolayer, or micropore filling, range, that is not the case for certain microporous materials such as clays, coals, and some activated carbons, for which the desorption curve does not reconnect with the adsorption one and hysteresis is observed even down to the lowest attainable pressures, like for the isotherm shown in **Figure 2.6**. This phenomenon is one other consequence of the strong interaction between the N_2 molecule's quadrupole moment and the adsorbent's surface; the adsorbate molecules can irreversibly enter and bind to pores of molecular dimension and can produce inelastic distortion in the adsorbent structure. In such cases, the application of standard methods for the determination of SSA and PSD could lead to meaningless results. As was long recognized, [59]–[61] using CO_2 adsorption analysis at 273.15 K can eliminate problems of this type. This is because of this molecule's very high critical temperature (32 K above analysis temperature) and saturation pressure (26200 torr), so the relative pressure measurements required for the micropore analysis are achieved in the range of moderate absolute pressures (1-760 torr). The elevated temperatures and pressures then eliminates the diffusion problems that are encountered with nitrogen analysis, since the CO_2 molecule has around the same size as N_2, but much more thermal energy, which allows it to fill smaller pores, even down to 0.4 nm, and achieve faster adsorption equilibrium. Considering these facts, CO_2 adsorption analyses were performed on all Raw samples. Firstly, they were degassed following the same procedure used in the case of N_2 adsorption. In these analyses, the dewar was filled with a mixture of water and ice instead of liquid nitrogen in order to maintain the 273.15 K temperature. The high saturation pressure of CO_2 also does so that

the relative pressure range of the analysis has an upper limit of 0.03, corresponding to the maximum absolute pressure that can be measured by the Asap 2020 Plus instrument with its 1000 mmHg transducer. This results in a pore size range measurable with this technique to pore diameters up to 1.5 nm. An example of such an isotherm can be observed in **Figure 2.7** for the case of sample 0.6-0.5 Raw. In order to obtain these CO_2 isotherms only the Dosing function was used, which was adjusted during the course of the analysis to obtain a sufficient number of points, while also preventing the measurements from becoming too much time consuming. For each sample, the corresponding N_2 and CO_2 curves are then matched and analyzed using apposite models in order to obtain detailed information about the carbon microstructure.

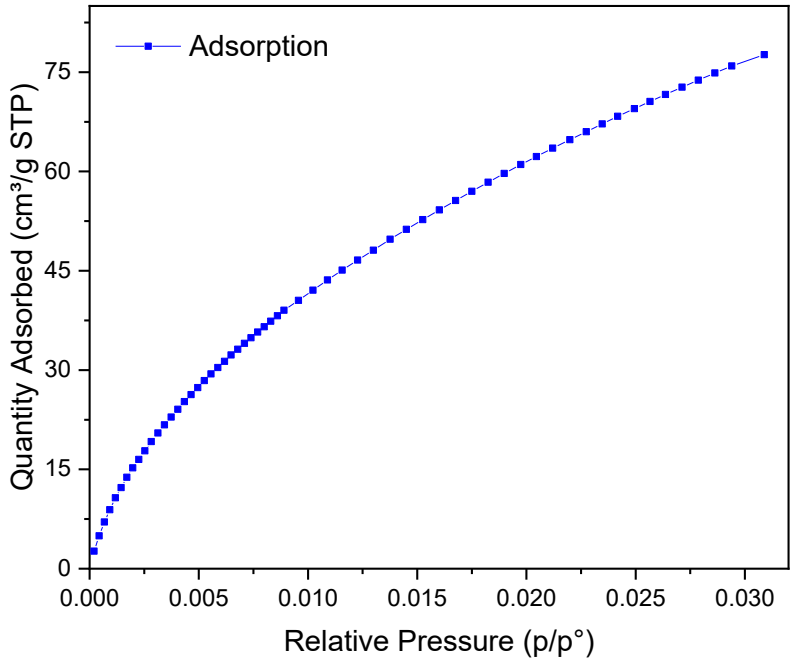

Figure 2.7: 0.6-0.5 Raw CO_2 adsorption isotherm.

All of the isotherms previously discussed and obtained can be studied by applying specific mathematical models (featured on the instrument's software) in order to obtain information on the morphology and structural properties of the sample.

2.3.1.3 SSA and PSD Measurements

The samples' SSA was determined with the instrument by means of the Brunauer-Emmett-Teller (BET), while their PSD was evaluated using Non-Local Density Functional Theory (NLDFT) models available on the instrument's software.

As mentioned in Paragraph 1.2.4.1, the classic BET application range $0.05 \leq \frac{P}{P_0} \leq 0.35$ proved to be incorrect, since the software's calculations offered negative C values. In order to correct this, the procedure previously described in that same Paragraph for the application of the BET theory in the case of microporous materials was followed. This resulted in all of the BET application ranges being shifted down to lower relative pressure values, where linearity of the BET plot could be observed, and the C constant were calculated as positive. The general range observed to be working was found at around $0.01 \leq \frac{P}{P_0} \leq 0.1$, with some degree of variability for each different sample.

Considering what was mentioned in Paragraph 1.2.4.2 the HS-2D-NLDFT model was used for the determination of the PSD of all the samples analyzed with N_2, in order to have a more accurate description of the chemically and geometrically heterogeneous pore surface. For Raw samples instead, a particular NLDFT model was used, which is capable of matching the isotherms obtained with N_2 and CO_2 and obtain the complete PSD of the sample. For the N_2 curve, the aforementioned HS-2D-NLDFT model was used, (HS-2D-NLDFT, Carbon, N2,77) while for CO_2 a specific model (CO2@273-Carbon, NLDFT). In all of these cases, the models were chosen with slit pore geometry, as this is the case for pores that are generally considered to be present in carbon materials [62].

2.3.2 Scanning Electron Microscopy (SEM) and Energy-Dispersive Spectroscopy (EDS)

Scanning electron microscopy (SEM) is a widely used technique for high-quality topographical images of materials under study. In SEM, a focused beam of high-energy electrons, accelerated by a voltage of a few kV is scanned across the surface of a sample; the interaction between the beam and the material produces, among other things, the emission of secondary electrons, i.e., weakly bound electrons from the conduction band. These are then collected by the detector, and this results in the development from the sample scan of an image of the surface at high resolution (of the order of nm). By looking at the images obtained with the SEM it is possible to observe the surface morphology of the analyzed material. In the course of this study, SEM images were obtained with a Zeiss SUPRA 40VP microscope.

This instrumentation also implemented the possibility to perform Energy-dispersive spectroscopy (EDS), which, instead of secondary electrons, detects the X-rays produced by the interaction between the electron beam and the sample. This allows a quantification of the

elements present in a given section of the sample. The SEM and EDS setup can be observed in **Figure 2.8**.

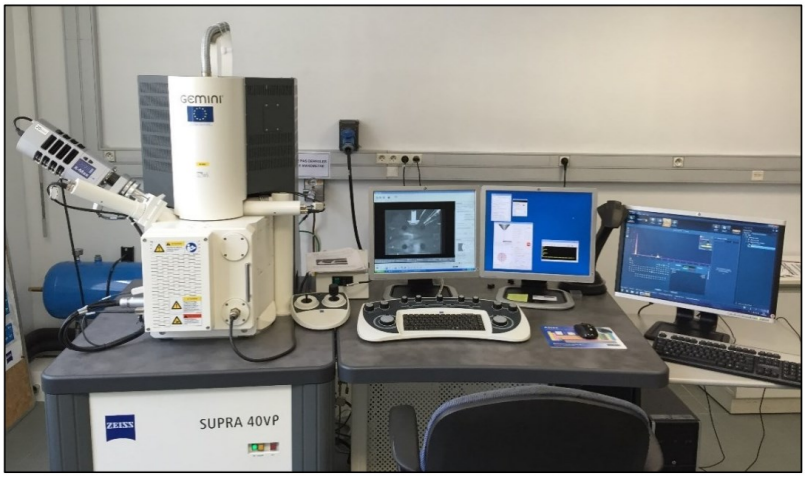

***Figure 2.8**:* Zeiss SUPRA 40VP microscope instrumental setup.

SEM images were acquired with an Electron High Tension (EHT) set to 5kV, while for EDS this was set to 20 kV. This was chosen since higher voltages penetrate deeper in the material, so the lower value allows obtaining images that better represent the surface of the material, while raising the tension up to 20 kV for EDS aids the quantification of materials that emit higher energy X-rays and as such need higher excitation energies to be detected.

2.3.3 X-ray Photoelecton Spectroscopy (XPS)

XPS is a technique that allows to identify the elements that compose a surface, along with their chemical states. Its core principle lies in the photoelectric effect described by Einstein in 1905[63], which stated that the atoms of a sample irradiated with sufficiently high energy photons can ionize and emit photoelectrons, the number of which is directly proportional to the intensity of the incident light. Provided that the photoelectron is emitted from the surface of the sample and it does not undergo inelastic scattering, its kinetic energy (KE) can be easily calculated by subtracting from the energy of the incoming photons (hv) the electron-atom binding energy (BE) and the sample's work function in vacuum Φ_S:

$$KE = hv - BE - \Phi_S \qquad (eq. 11)$$

This formula is corrected considering that the kinetic energy analyzer, which is responsible for the collection of the photoelectrons, also possesses a work function Φ_A, which shifts the

measured value of kinetic energy KE' from its real value KE. Being in electrical contact, the Fermi level of the sample and the analyzer are at the same level, and as such:

$$KE' = KE - (\Phi_A - \Phi_S) = hv - BE - \Phi_S - (\Phi_A - \Phi_S) = hv - BE - \Phi_A \quad (eq.12)$$

Which solved for the photoelectron BE gives the result:

$$BE = hv - KE' - \Phi_A \quad (eq.13)$$

The output of the XPS analysis is a spectrum with peaks that arise at specific binding energies. This technique allows a qualitative and quantitative analysis of the elements present in the sample by comparing the experimentally obtained peaks with the ones present in literature.[64] The chemical state of the elements can also be determined considering that a more oxidized element has a lower electron density compared to its neutral or reduces counterparts; this results in the remaining electrons being subject to lower shielding of the nuclear positive charges, and, as a consequence, a higher BE. As mentioned before, the XPS technique is based on the collection of photoelectrons that do not undergo inelastic scattering. This renders the XPS analysis capable of only assessing the extreme surface of a sample, down to ~10 nm, since only in the outmost ~20 atomic layers photoelectrons are able to elastically arise from the surface. During the course of this study, (XPS) was performed with a Thermo Scientific ES-CALAB QXi spectrometer, shown in **Figure 2.9**, along with a schematic illustration of the XPS process.

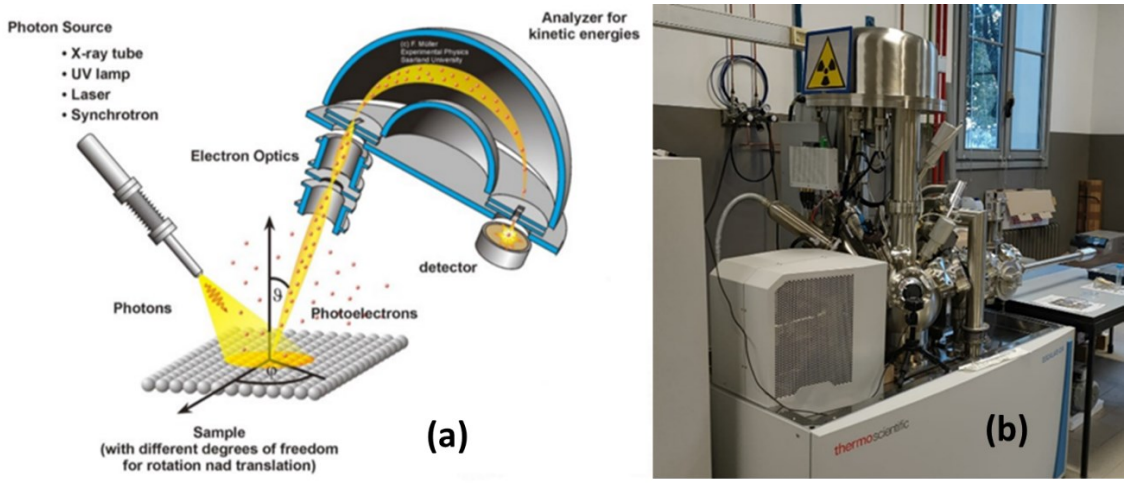

Figure 2.9: (a) Scheme of the typical XPS setup and illustration of the process [65]; **(b)** Thermo Scientific ES-CALAB QXi spectrometer.

The technique was performed using a monochromatized Al Kα source (hν=1486.68 eV) and a charge compensation gun. Survey spectra were acquired at 100 eV pass energy, 0.5 eV/step and 25 ms/step dwell time; spectral regions have been collected at 20 eV pass energy, 0.1 eV/step and 25 ms/step dwell time Elemental quantification was carried by the integration of the photopeaks, with the *Avantage* software after Shirley-type background subtraction.

2.3.4 X-Ray Diffraction (XRD)

X-Ray diffraction (XRD) is a fundamental technique for characterizing the structure of materials. When a monochromatic X-ray beam interacts with a crystalline solid, it scatters off the atoms within the solid. The resulting scattered waves, having the same wavelength, interfere with each other, either constructively or destructively, generating a diffraction pattern. When the scattered waves are in-phase constructive interference occurs ,leading to a doubling of the wave's amplitude, while, on the contrary, when the waves are out-of-phase and cancel each other out, destructive interference occurs. The condition for achieving constructive interference is described by Bragg's law:

$$n\lambda = 2d_{hkl}lsin\theta \qquad (eq.14)$$

Where n is an integer representing the order of reflection, λ is the wavelength of the incident radiation, d_{hkl} is the distance between crystallographic planes with Miller indices h, k, and l, and θ is the diffracting angle. X-ray diffractograms provide valuable information about the structure and microstructure of materials. The position of the peaks allows for the calculation of interplanar distances using Bragg's law (Equation 14) and can be compared to databases like the Powder Diffraction File (PDF-4) to determine the crystalline structure. The presence of a preferred crystallographic orientation can instead be deduced from the intensity of the peaks. In single-crystalline or textured films, only peaks corresponding to the same family of planes are detected, while in non-textured polycrystalline films, multiple peaks are identified due to the varying orientations of the grains within the sample. By looking at the shape of the peaks, information can be obtained about the microstructure, including the presence of defects, non-uniform deformations, and the size of the crystallites. In this study, powder XRD analysis was performed with a Bruker D8 Advance diffractometer (illustrated in **Figure 2.10**) in Bragg–Brentano geometry was employed, with

a Cu Kα source (λ=0.154 nm). The patterns were acquired in the range of 2θ=10-80°, with steps of 0.02° and dwell time of 0.35 s/step. For the analysis of the acquired data, *Diffrac.EVA 6.0* software was used.

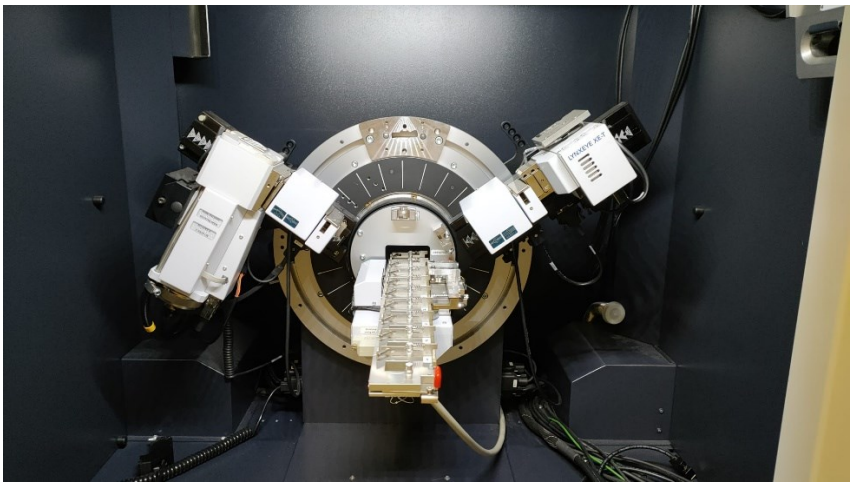

Figure 2.10: Bruker D8 Advance diffractometer.

2.3.5 CHNSO analysis

In order to obtain highly reliable data on the bulk composition of the samples, elemental CHNSO analysis was performed. Organic Elemental Analyzer "OEA" is a simultaneous technique for the determination of Carbon, Hydrogen, Nitrogen and Sulfur, contained in organic and inorganic materials in solid, liquid and gas form. In this analysis, a few mg of the sample are weighed in a tin capsule and then introduced into the combustion reactor by an autosampler. Once inserted, the special furnace is heated at 1020 °C, then a small volume of pure Oxygen is added to the system and helps burn the sample. This then undergoes reduction using copper to convert it into elemental gases. Finally, a separation column and TCD detector allow the determination of elements. The sample's Carbon, Hydrogen, Nitrogen and Sulfur composition is as such obtained as weight % with Oxygen ultimately determined as the difference. For this analysis, a Thermo Fisher FLASH 2000 CHNS/O Analyzer instrument was used, an illustration of which can be observed in **Figure 2.11**.

Figure 2.11: Thermo Fisher FLASH 2000 CHNS/O Analyzer.

2.3.6 Hydrogen uptake measurements

For the evaluation of the samples' hydrogen adsorption capacity, isotherms of the samples were obtained with H_2 as adsorptive gas, using the ASAP 2020 Physisorption instrument previously mentioned in Paragraph 2.3. To have a source of pure hydrogen, necessary for this analysis, a Cinel AD-300 hydrogen generator (purity > 99,99999% [66]) was connected to one of the inlets of the ASAP 2020 instrument. As such, the hydrogen adsorption capacity calculated is obtained through volumetric determination under static conditions. Prior to the analysis the chosen samples were weighed and degassed following the same process described in paragraph 2.3.1.2 for the determination of N_2 isotherms. The procedure followed for the analysis is the one described in the Micromeritics Application note 136 [67]Since the critical temperature of hydrogen is 33.20 K, and as such it is a non-condensing gas, the isotherms were obtained using the absolute pressure of the adsorbed gas instead of the relative one. The pressure table was chosen in order to have an appreciable and well-defined curve. In this case, differently form the N_2 and CO_2 isotherms, only the adsorption curve was obtained, and the final pressure reached was the maximum one suggested by Micromeritics for this instrument, which is 850 mmHg, so as to assess the maximum quantity of hydrogen that the material is capable of adsorbing at the highest obtainable pressure. All the analyses were performed at 77 K. For all chosen samples, H_2 adsorption isotherms were obtained, an example of which is shown in **Figure 2.12** for sample 1-0.8 AcOH.

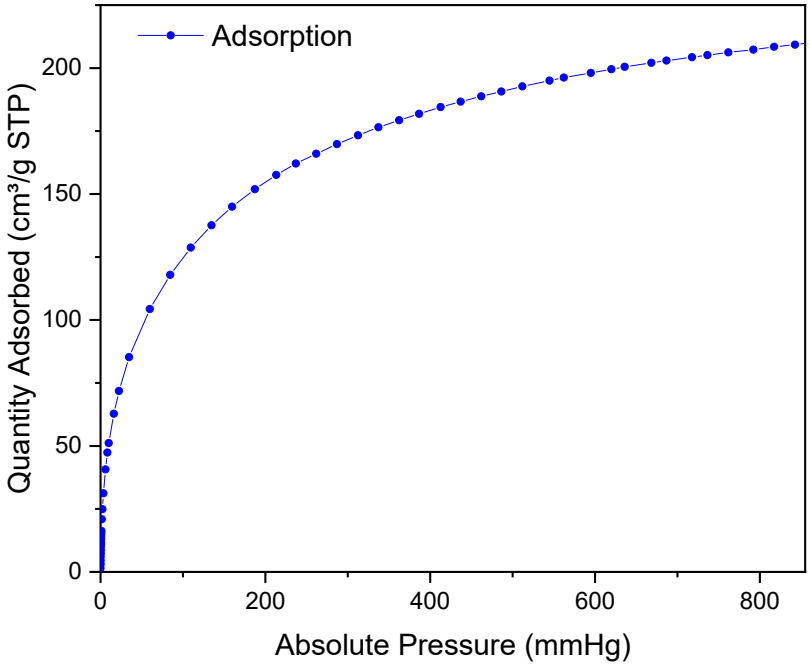

Figure 2.12: 1-0.8 AcOH H_2 adsorption isotherm.

From the isotherms, consequently, the hydrogen adsorption capacity was determined, as weight percent of hydrogen per gram of sample. An example of the curves obtained can be observed in **Figure 2.13(a)** In **Figure 2.13(b)** instead, in order to better appreciate the increase of the quantity of adsorbed hydrogen at low pressures, the hydrogen uptake is presented with the absolute pressure in logarithmic scale plotted against the hydrogen uptake.

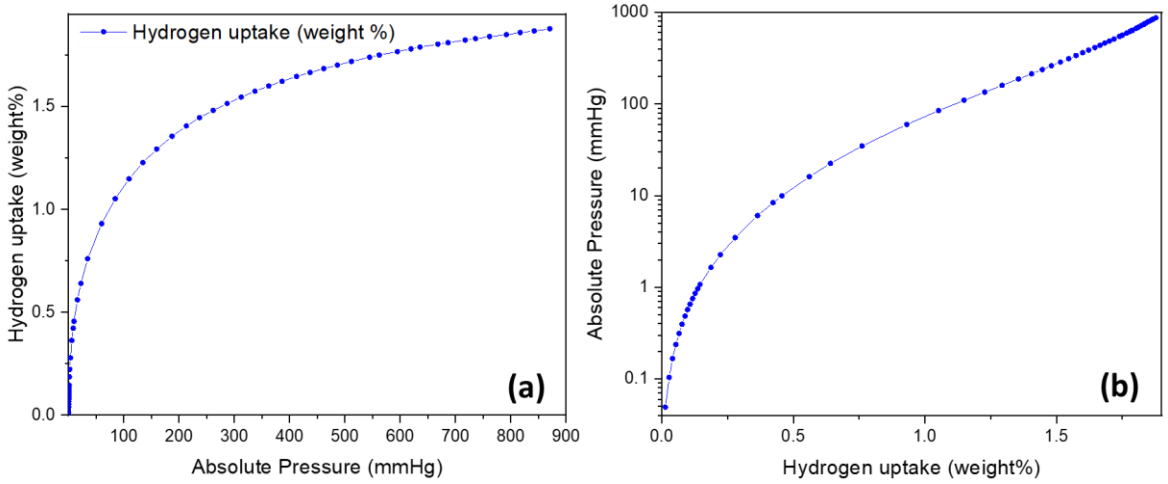

Figure 2.13: *(a)* 1-0.8 AcOH Hydrogen uptake versus absolute pressure; (b) 1-0.8 absolute pressure in log scale versus hydrogen uptake.

3 CHARACTERIZATIONS

3.1 Raw samples

3.1.1 Adsorption Isotherms

First, adsorption and desorption isotherms for all Raw samples were obtained, in order to determine their SSA and PSD. As explained in Paragraph 2.3.1.2, a lot of difficulties were encountered in the process of obtaining these, due to the quadrupolar nature of the N_2 molecule, which interacts too strongly with the surface of carbon materials. This, at the very low pressures required to fill very small micropores, results in a hampered diffusion and equilibration process, and consequently in analyses that are excessively time-consuming, under-equilibrated, and erroneous. After attempting to use nitrogen to characterize the low relative pressure region of the isotherm, CO_2 at 273.15 K was chosen as an adsorptive to remedy the problems associated with the use of N_2 at 77 K, for the reasons explained in the same paragraph mentioned above. This proved to be a successful solution, and, for each Raw sample, two different isotherms were obtained:

- N_2 adsorption and desorption isotherm in the p/p^0 range 0.002-1, that characterize the material's macro, meso- and bigger micropores;
- CO_2 adsorption isotherm in the p/p^0 range 0-0.03, that characterize the material's micropores.

Due to the curves being extremely close in x-y values, the isotherms are presented separately for each Raw sample in **Figure 3.1-3.9** for clarity. To better appreciate the quantity of gas adsorbed at the lowest pressures, and to have a comprehensive view of the sum of the CO_2 and N_2 adsorption curves, these are also reported as an ensemble with the x axis in Log10 scale for each sample in **Appendix A**. The linear scale is instead unsuitable for showing both isotherms in the same graph, due to the CO_2 curve being of a much smaller range compared to the N_2 one. Nonetheless, this scale was chosen due to it being coherent with the IUPAC isotherms classification, and as such much more useful for determining information about the material analyzed.

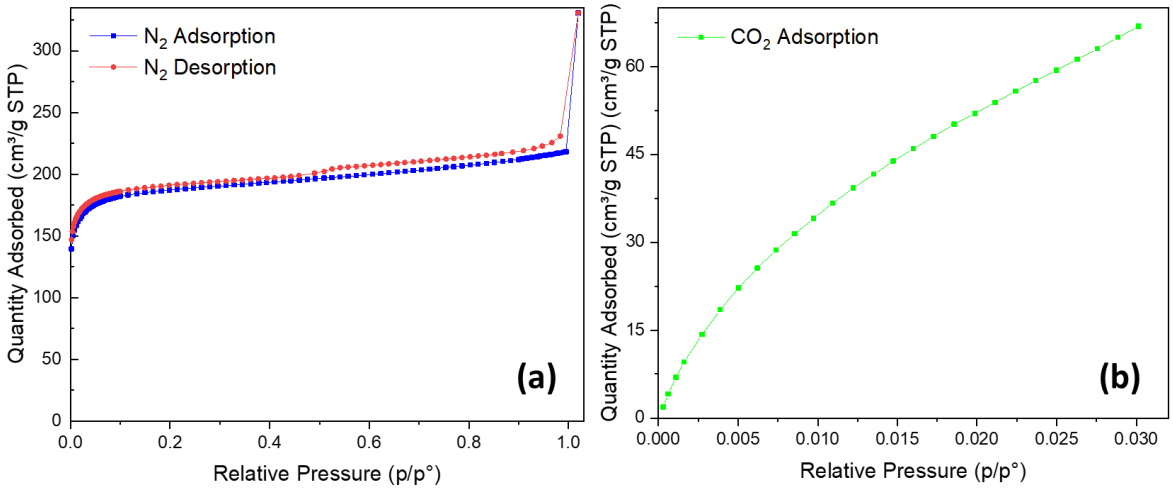

Figure 3.1: (a) N_2 adsorption and desorption isotherm for sample 2.83-2 Raw; (b) CO_2 adsorption isotherm for sample 2.83-2 Raw.

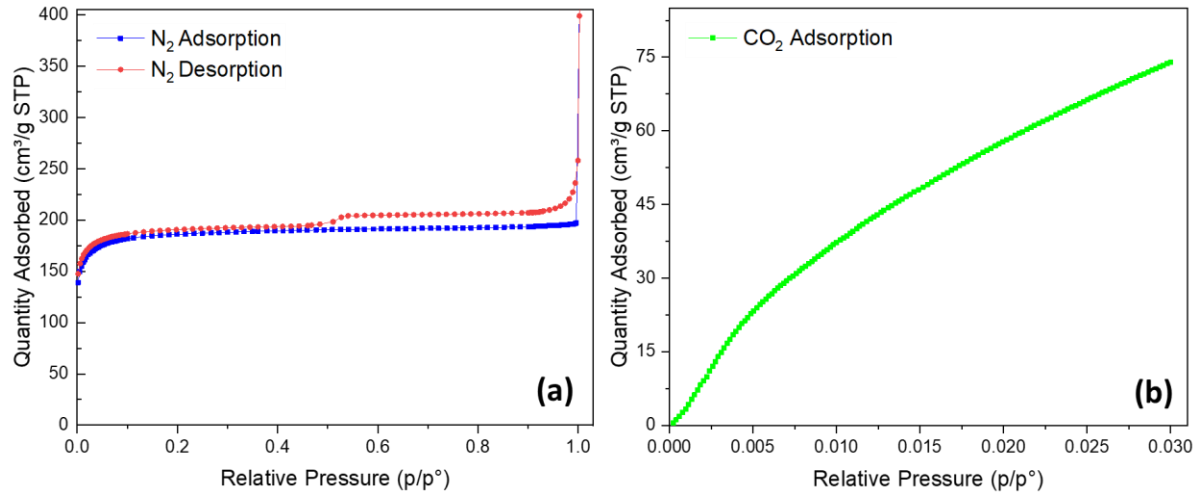

Figure 3.2: (a) N_2 adsorption and desorption isotherm for sample 2-1.4 Raw; (b) CO_2 adsorption isotherm for sample 2-1.4 Raw.

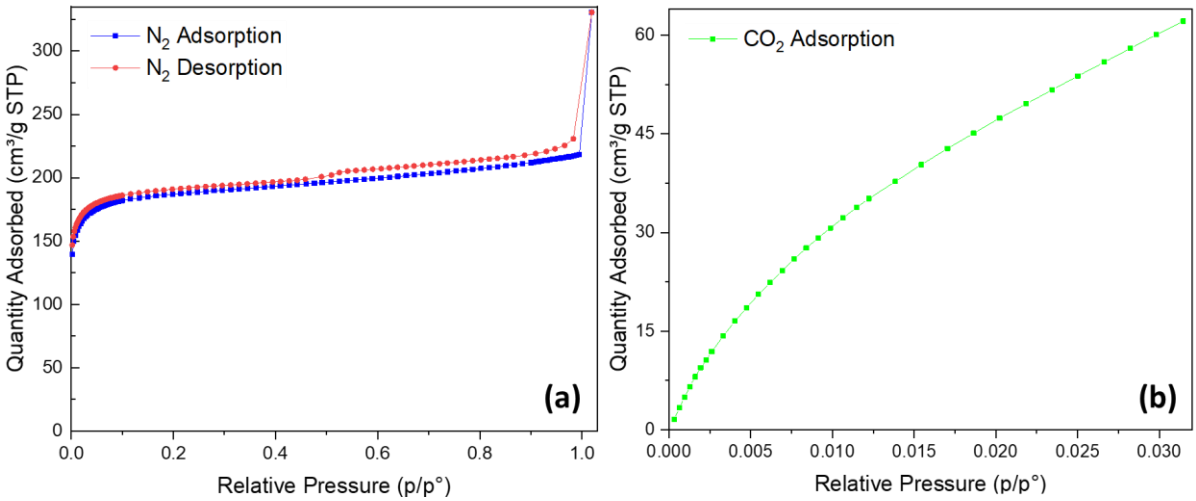

Figure 3.3: (a) N_2 adsorption and desorption isotherm for sample 1.4-1 Raw; (b) CO_2 adsorption isotherm for sample 1.4-1 Raw.

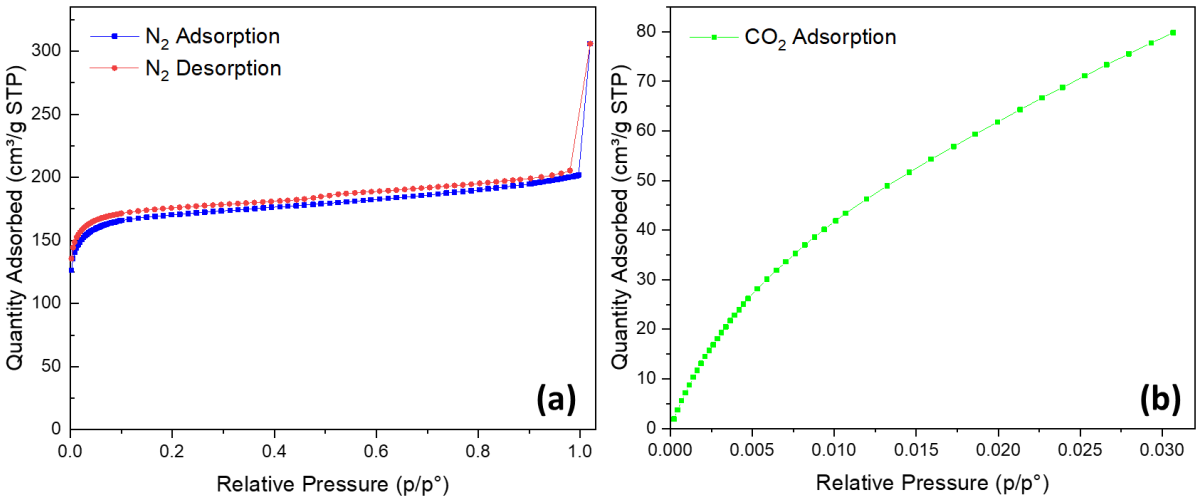

Figure 3.4: (a) N_2 adsorption and desorption isotherm for sample 1-0.8 Raw; (b) CO_2 adsorption isotherm for sample 1-0.8 Raw.

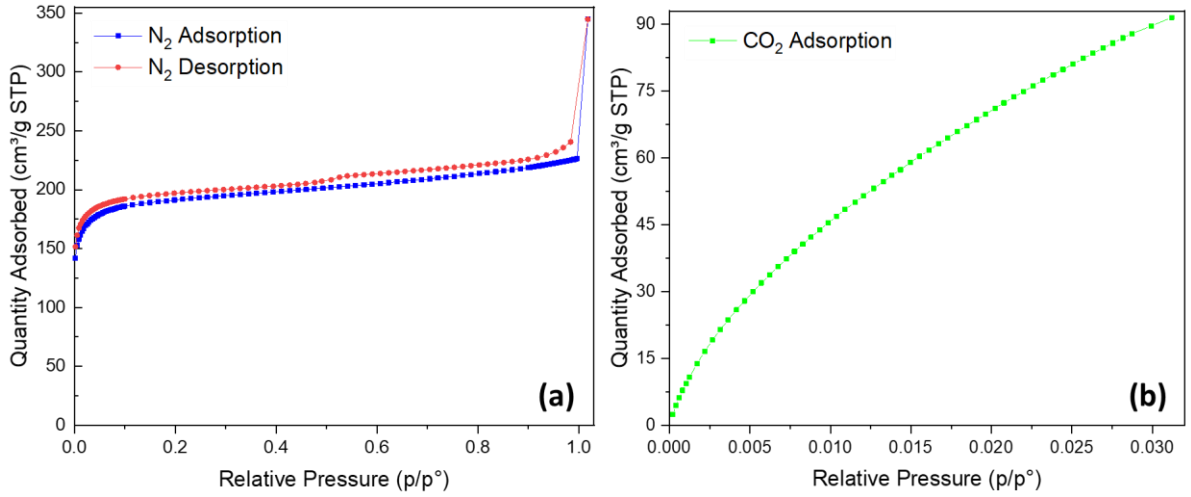

Figure 3.5: (a) N_2 adsorption and desorption isotherm for sample 0.8-0.6 Raw; (b) CO_2 adsorption isotherm for sample 0.8-0.6 Raw.

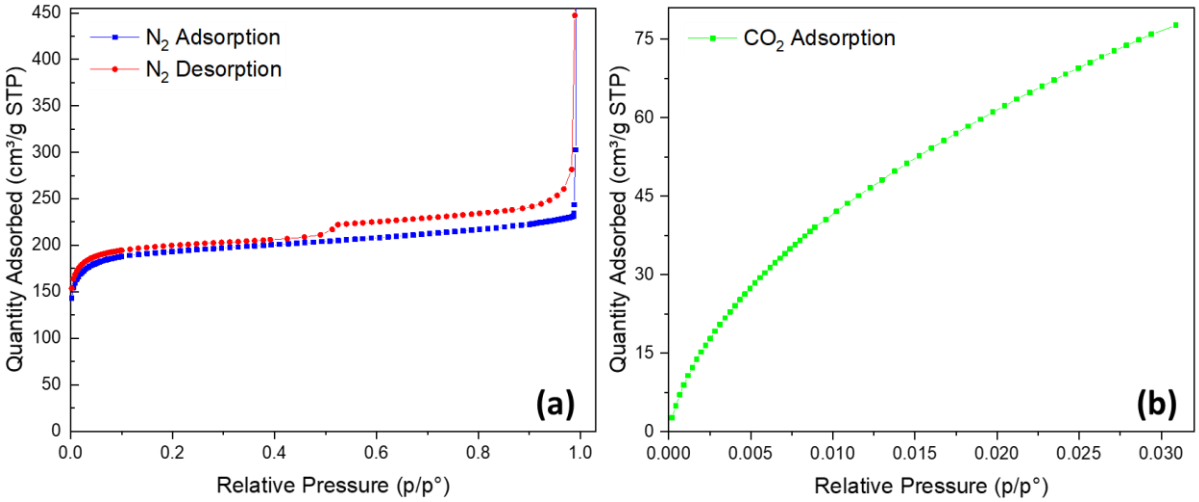

Figure 3.6: (a) N_2 adsorption and desorption isotherm for sample 0.6-0.5 Raw; (b) CO_2 adsorption isotherm for sample 0.6-0.5 Raw.

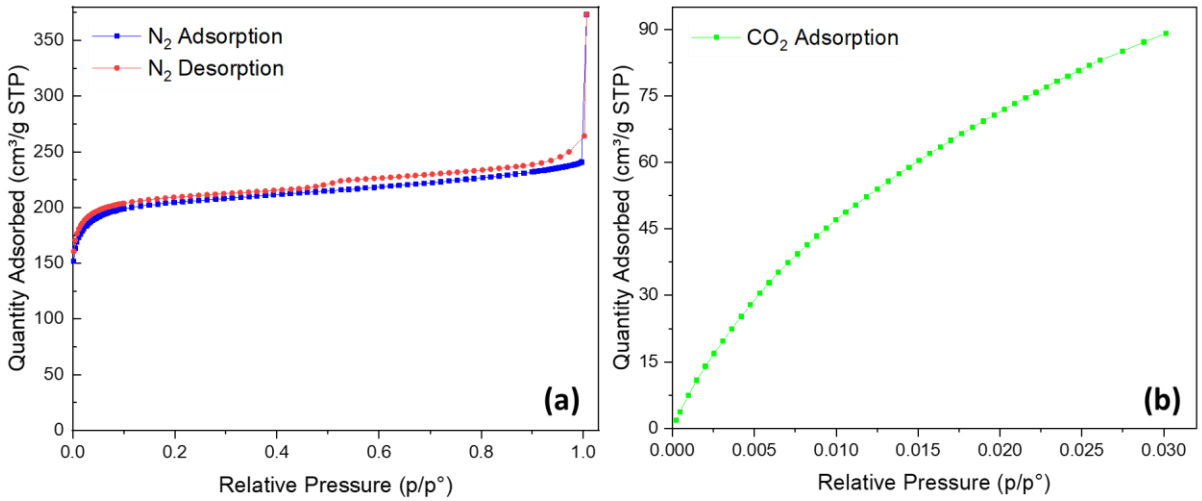

Figure 3.7: (a) N_2 adsorption and desorption isotherm for sample 0.5-0.4 Raw; (b) CO_2 adsorption isotherm for sample 0.5-0.4 Raw.

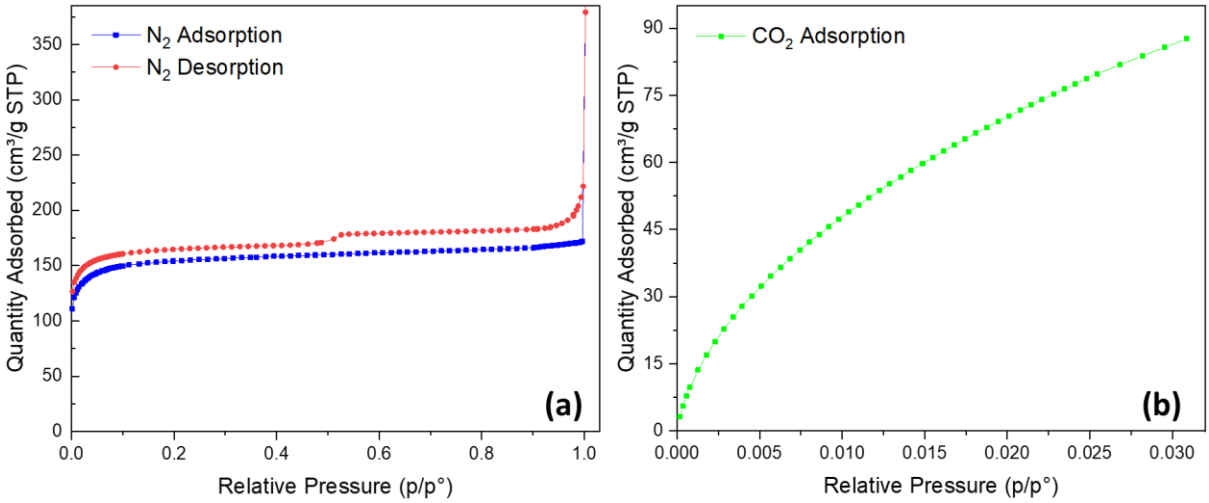

Figure 3.8: (a) N_2 adsorption and desorption isotherm for sample 0.4-0.3 Raw; (b) CO_2 adsorption isotherm for sample 0.4-0.3 Raw.

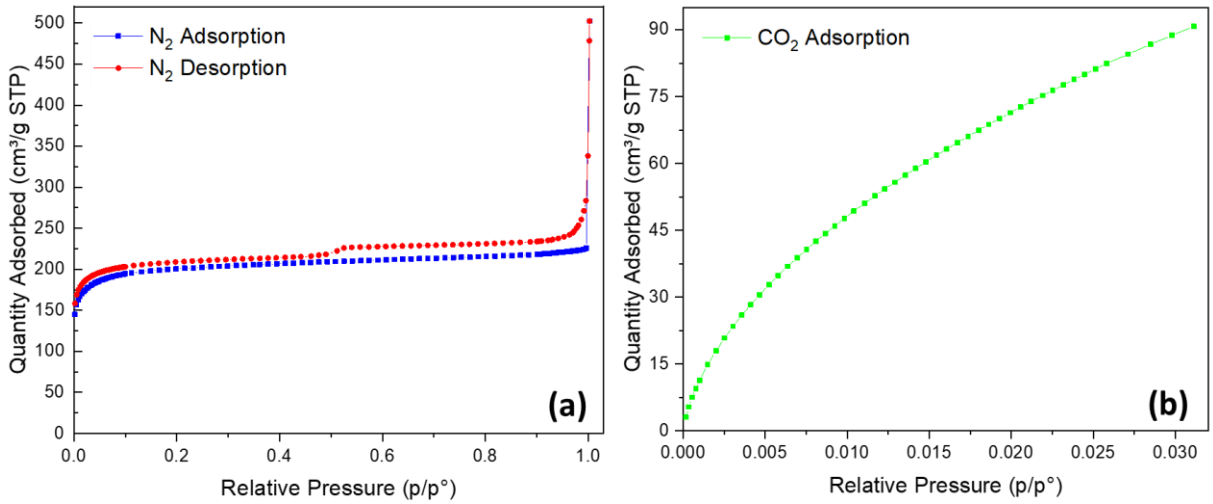

Figure 3.9: (a) N_2 adsorption and desorption isotherm for sample <0.3 Raw; (b) CO_2 adsorption isotherm for sample <0.3 Raw.

Looking at the N_2 isotherm for all Raw samples the first thing that can be noticed is the resemblance of the curves with the Type I IUPAC classification [34]. Although most of the vertical part of the curve is missing due to the problems previously explained, one could still appreciate the initial steep uptake at very low p/p^0, followed by a plateau. This is indicative of the highly microporous nature of all the samples, whose micropores are completely filled at extremely low relative pressures and govern the limiting value of gas adsorbed. The knee of the curves is neither too steep or too broad, and as such resulting a hybrid of the Type I(a) and Type I(b) isotherm, indicating the presence of mostly narrow micropores (pore width $\leq$ 1 nm), but also larger micropores and small mesopores (pore width $\leq$ 2.5 nm). As is the case for a lot of materials, the isotherm obtained is not strictly Type I, but appears to be a composite of also Type II and Type IV. In fact, after the initial steep uptake, one does not observe a completely flat plateau, but instead a small and gradual growth of the amount of gas adsorbed. This happens both at intermediate relative pressures, indicating the presence of mesopores, related to Type IV, and at $p/p^0 \rightarrow 1$, where a slightly steeper growth can be observed, typical when in presence of macropores (Type II). Another important feature of the curve is the presence of a hysteresis loop, which is a further confirmation of the presence of mesopores in the material, since pores of these widths typically fill via capillary condensation. This results in a desorption branch which is separated from the adsorption one due to the different phenomena involved in the two processes (multilayer adsorption and condensation for adsorption, evaporation for desorption, as explained in detail in Paragraph 1.2.3). In particular, the hysteresis loop in question clearly matches the Type H4, with the desorption branch reuniting abruptly with the adsorption branch in the range $0.4 < p/p^0 < 0.5$, which is typical of nitrogen at 77 K. This type of loop denotes the presence of cavitation (i.e the mechanism of desorption from larger pores that involves the spontaneous nucleation and growth of gas bubbles in the metastable condensed fluid [36], [37], [42]), which suggests the presence of pore necks smaller than 5-6 nm, and also renders the desorption branch useless for the determination of neck pore size. As explained in Paragraph 2.3.1.2, the point taken at $p/p^0 = 1$ is fictitious and should not be considered in the analysis, since a lot of gas condensation happens, and the quantity adsorbed at this point is not properly indicative of the textural features of the materials. As consequence of this, physisorption analysis can be used for pores with sizes up to 300 nm. This erroneous point could also result in an exaggerated hysteresis loop, since all the excess condensed gas has to be desorbed, and the presence of macropores that are not completely filled with adsorbate can contribute to the loop, as it happens in Type H3.

In the CO_2 isotherms, only a small curve is observed due to the small range of relative pressures available for this gas. The quantity adsorbed at the same pressures is considerably lower for these isotherms compared to the N_2 ones, simply due to the much higher analysis temperature. Since physisorption is a highly chaotic phenomenon based on weak Van der Waals interactions (4-5 kJ/mol), raising the temperature from 77 K to 273.15 K reduces greatly the amount of gas that stays adsorbed on the surface of the material.

3.1.2 SSA and PSD

Starting from the N_2 isotherms, the SSA of all the Raw samples was determined following the procedure described in Paragraph 2.3.1.3. As already specified, the range in which the BET equation proved to be applicable was $0.01 \leq p/p^0 \leq 0.1$. The as-obtained SSA_{BET} values are reported in **Table 3.1**

Table 3.1: List of Raw samples and relative SSA_{BET} values.

Sample	SSA_{BET} (m^2/g)
2.83-2	736
2-1.4	739
1.4-1	714
1-0.8	674
0.8-0.6	755
0.6-0.5	763
0.5-0.4	795
0.4-0.3	609
<0.3	798

The SSA_{BET} of the Raw samples ranges from 609 to 798 m^2/g, with no clear trend observed as the particle size is decreased. To better observe this, the different values are plotted in a column graph in **Figure 3.10**.

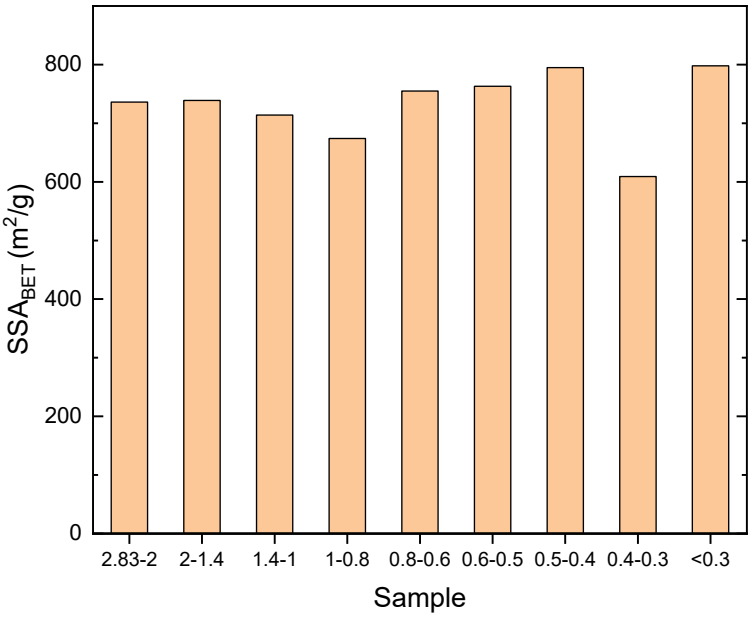

Figure 3.10: Column graph of Raw samples and relative SSA_{BET} values.

All the specific surface area values seem to fluctuate around quite a restricted range, with no discernible trend. This can be explained with the concurrence of two different factors. While on one hand the surface area of a material is expected to increase with decreasing particle size, due to smaller particles having a larger portion of atoms on their surface [68], on the other, the highly microporous nature of the material is the reason behind the absence of this expected increase. What actually happens is that a higher degree of comminution causes the destruction of part of the internal porous structure [69]. Thus, bigger particles provide a better matrix for the development of a complex pore structure [70], [71], which, in the case of a microporous material such as the one in analysis, determines the limiting value of the surface area, since the external area is negligible in comparison. These two factors compete with each other, causing the fluctuating values of SSA with decreasing particle size. An observation that can be made is that, in the works already cited that investigate this, a clearer increasing trend of specific surface area is observed with smaller particles. The absence of this in the Raw samples analyzed can be explained by the fact that the studied material seems to generally have quite a low surface area when compared to the general value of ordinary activated carbons, which is around 1000-1500 m^2/g [72]. This is intuitively due to the composition of the material analyzed. As a matter of fact, what we are presented with is a form of AC that was used as an adsorbent in water filters. As consequence of this, one can expect the presence of impurities caused by polymeric materials (added to the mixture during the extrusion process to bind the AC used in the filter, as

reported by Think:Water) and ions that stay adsorbed in the carbon during use, which both contribute negatively to the porosity of the material. Thus, the microporous network is not as developed as in ordinary ACs, and the external area has a higher contribution, resulting in SSA not clearly raising or lowering with decreasing particle size for the competing factors explained above.

The PSD of the Raw samples was instead determined with the NLDFT models listed in Paragraph 2.3.1.3. Using a model that can match and combine the N_2 and CO_2 isotherms, a complete differential pore size distribution could be obtained for all samples, illustrated in **Figure 3.11**. To better appreciate the different PSD of each Raw sample, the same curves can be found shown individually in **Appendix B**.

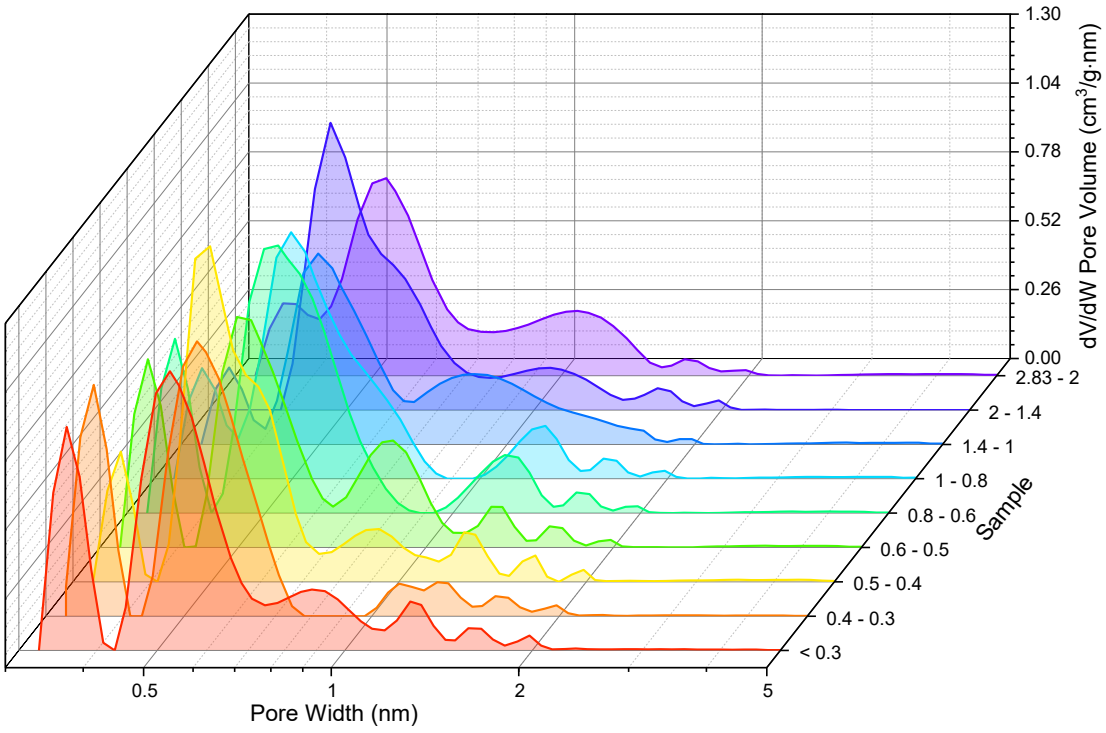

Figure 3.11: Differential pore size distributions for all Raw samples.

These curves were analyzed to determine different structural parameters that characterize the samples, which are the following:

- DFT total pore volume (cm^3/g), calculated by integration of the whole PSD;
- DFT pore size (nm), corresponding to the maxima of the PSDs;
- DFT ultra-micropore cumulative pore volume (cm^3/g), calculated by integrating the PSD from the minimum pore width value to up to 0.7 nm;

- DFT micropore cumulative pore volume (cm^3/g), calculated by integrating the PSD from the minimum pore width value to up to 2 nm;
- Micropore %, calculated dividing the micropore pore volume by the total pore volume.

All these quantities are reported for each Raw sample in **Table 3.2**.

Table 3.2: List of Raw samples and relative structural parameters obtained from their differential pore size distribution.

Sample	DFT total pore volume (cm^3/g)	DFT pore size (nm)	DFT cumulative pore volume (cm^3/g)		Micropore %
			Ultra-micropores	Micropores	
2.83-2	0.33	0.52	0.15	0.30	91
2-1.4	0.30	0.47	0.18	0.30	100
1.4-1	0.32	0.50	0.14	0.29	91
1-0.8	0.33	0.50	0.19	0.28	85
0.8-0.6	0.35	0.52	0.23	0.33	94
0.6-0.5	0.35	0.50	0.17	0.33	94
0.5-0.4	0.39	0.50	0.22	0.34	87
0.4-0.3	0.31	0.52	0.22	0.29	94
<0.3	0.38	0.52	0.21	0.35	92

Looking at both **Figure 3.11** and **Table 3.2**, the first thing that can be noticed is the extremely high microporous nature of the carbons studied, since the curves become basically flat after the 2 nm pore width, fact that is reflected in the values of micropore % obtained, which range from 85-100 %. The maxima of the PSD stay pretty steadily around the 0.50 value, which proves that the degree of comminution does not alter the PSD in such a dramatic way that results in a strong shift of the major fraction of pores. What can be observed from the curves with decreasing particle size is instead the development of a peak centered at around 0.35 nm, and the separation of the broader peak centered around 1 nm into different and sharper peaks, present in the range of super-micropores (0.7 - 2 nm). In general, the milling process seems to differentiate broad distribution of pores into more numerous and sharper pore fractions. This is partly reflected in the parameters obtained. As a matter

of fact, as for the SSA, a precise trend cannot be found for the calculated volumes, probably due to the aforementioned presence of impurities in the samples. This results in quite small pore volumes if compared with typical ACs, that vary so little with the particle size (0.09 cm^3/g for total pore volume) that spotting a clear and discernible trend is made very difficult. Additionally, a general increase in the pore volumes at smaller particle sizes can be noticed, which is not clearly reflected in the SSA_{BET}. This could be explained by the fact that a higher milling degree generally results in the development of larger pores [70], [71], which contribute greatly to the total pore volume of the material, but not as much to its surface area when compared to pores of small widths.

3.2 Chemically activated samples

After evaluating the SSAs and PSDs obtained for the Raw samples, some of them were chosen to be chemically activated following the procedure explained in Paragraph 2.2.1. The followed criteria was the selection of the ones that allowed the investigation of the broadest range of different SSA, but still making use of most of the various particle sizes available, so as to investigate the effect of this parameter on the activation. The Raw samples chosen were the 2.83-2 Raw, 2-1.4 Raw, 1-0.8 Raw and <0.3 Raw.

The yield of the activation process was found to be around 18% for all samples, considering the sum of the mass obtained for the samples washed with water (W) and the ones washed with acetic acid and water (AcOH). This is quite a high yield when compared for example to the one found by Andas et al. for the same C:KOH ratio 1:2 (9%, [73]), probably due to the different nature of the carbon precursor used. One thing that could be observed was actually the fact that the grains, once activated, tend to retain their structure, while still decreasing sensibly in particle size. So what was obtained, instead of a fine powder for all samples, were materials with grains of different size for each different granulometry, in accordance with the starting size of the particles. This fact can be explained with the nature of the ACs extracted from the exhausted filters, which are already granular to start with, and also with the use of KOH in pellet form instead of powder.

3.2.1 Adsorption Isotherms

For all activated samples, N_2 adsorption and desorption isotherms were successfully obtained using the Dosing function, as described in Paragraph 2.3.1.2. In order to clearly observe the curves obtained, in **Figures 3.12-3.15**, for each activation, the N_2 isotherms are reported for the Raw sample, the activated sample washed with only water (W), and the activated sample washed with acetic acid and water (AcOH). For the <0.3 sample, the whole activated product was only washed with acetic acid and water, for reasons that will be explained later in Paragraph 3.2.7. For the analysis of the activated samples the point corresponding to $p/p^0 = 1$ was excluded, stopping the adsorption at the relative pressure value of 0.995, resulting in correct curves without excessive condensation at the saturation point that was instead present in the Raw isotherms.

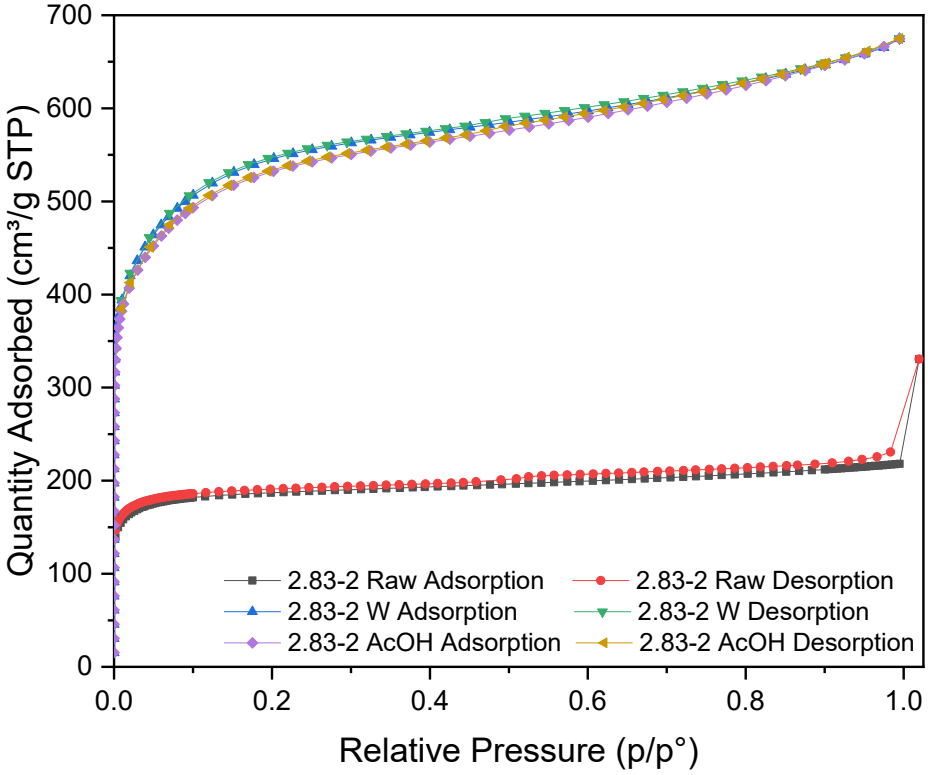

Figure 3.12: N_2 adsorption and desorption isotherms for sample 2.83-2 Raw, 2.83-2 W and 2.83-2 AcOH.

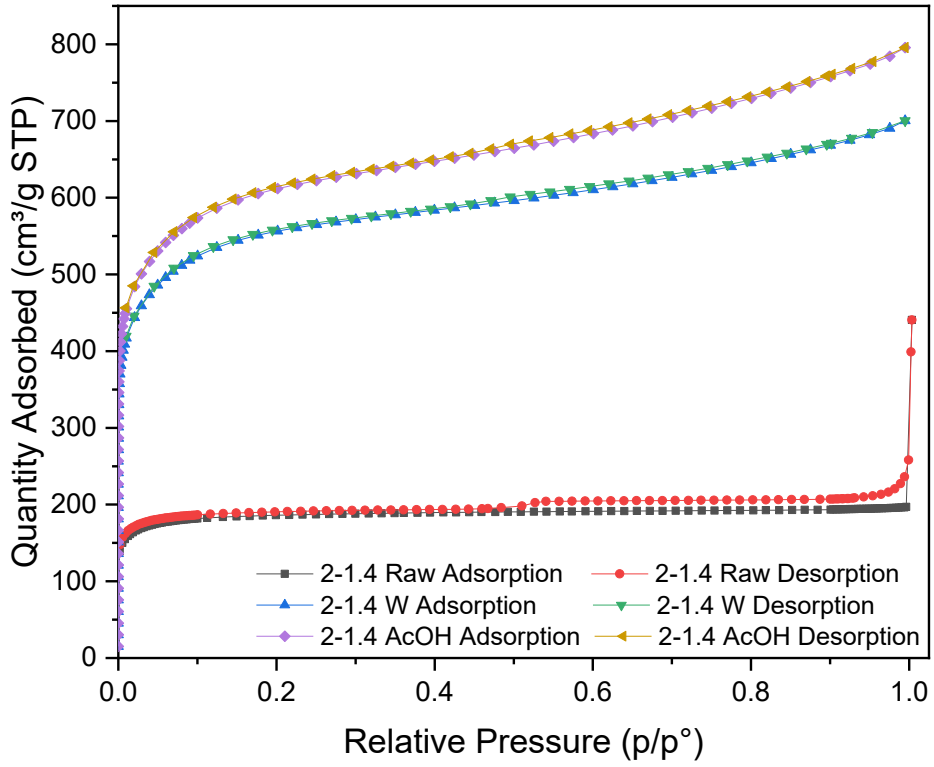

Figure 3.13: N_2 adsorption and desorption isotherms for sample 2-1.4 Raw, 2-1.4 W and 2-1.4 AcOH.

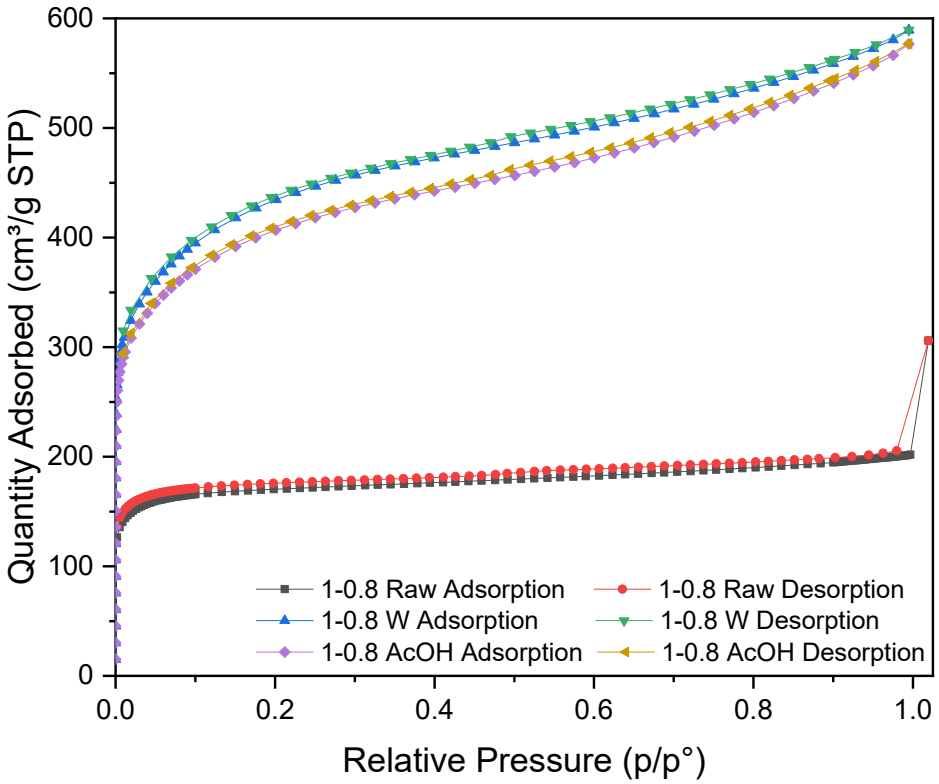

Figure 3.14: N_2 adsorption and desorption isotherms for sample 1-0.8 Raw, 1-0.8 W and 2. 1-0.8 AcOH.

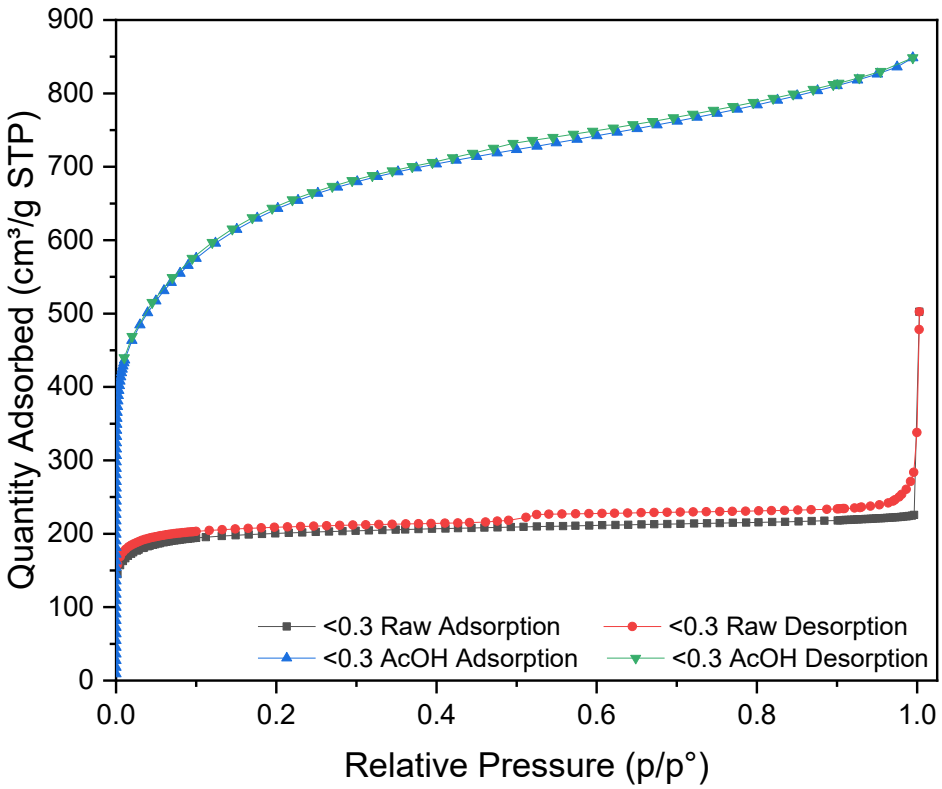

Figure 3.15: N_2 adsorption and desorption isotherms for sample <0.3 Raw, and 2. <0.3 AcOH.

For all activated samples the isotherms appear to be quite similar, and, for most aspects, analogous with the analysis reported for the Raw samples in Paragraph 3.1.1. In fact, all isotherms clearly exhibit mostly Type I character, denoting the highly microporous nature of the samples. In the W and AcOH cases though, compared with the Raw, the knee of the curves appears less steep, clearly as for Type I(b), indicating the presence a pore size distribution that spans over a broader range including wider micropores and narrow mesopores (< 2.5 nm) [34]. The curves of the activated samples also reach much higher values of quantity of gas adsorbed, clearly showing a much higher surface area and pore volumes obtained with the activation process. This is probably the factor that made it possible to obtain the vertical part at low relative pressures, since higher amounts adsorbed are more easily detected and equilibrated by the instrument. Another possible cause of this, related with the impure nature of the non-activated sample when compared to the one treated with KOH, will be discussed more in depth later. Differently from the Raw isotherms, the activated ones show a less defined plateau after the initial steep uptake, with a more pronounced increase of gas adsorbed at both medium and high relative pressures. This is telling of the presence of a bigger fraction of meso- and macropores in the samples when compared to the non-activated material, denoting Type II and Type IV character. Furthermore, even after

activation hysteresis of type H4 can be observed, with the desorption branch reuniting with the adsorption one due to cavitation in the 0.4-0.5 p/p^0 range. These hysteresis loops, though, appear way thinner when compared to the Raw sample ones, confirming the theory explained in Paragraph 3.1.1 about the excessively high hysteresis due to the excessive condensation that occurs at the saturation point.

3.2.2 SSA and PSD

Starting from the N_2 isotherms, the SSA of all the activated samples was determined following same procedure explained for the Raw samples. Once again, the range in which the BET equation proved to be applicable was $0.01 \leq p/p^0 \leq 0.1$. In **Table 3.3** the SSA_{BET} values obtained for the Raw samples and its respective W and AcOH activated version are reported.

Table 3.3: List of Raw and activated samples with relative SSA_{BET} values.

Sample	SSA_{BET} (m^2/g)
2.83-2 Raw	736
2.83-2 W	2042
2.83-2 AcOH	1988
2-1.4 Raw	739
2-1.4 W	2107
2-1.4 AcOH	2302
1-0.8 Raw	674
1-0.8 W	1590
1-0.8 AcOH	1493
<0.3 Raw	798
<0.3 AcOH	2340

The SSA_{BET} of the activated samples is noticeably higher than the one of their Raw counterparts, ranging from 1493 to 2340 m^2/g. To have a clearer picture of the comparison between raw and activated samples, the surface area values are plotted in a column graph in **Figure 3.16**.

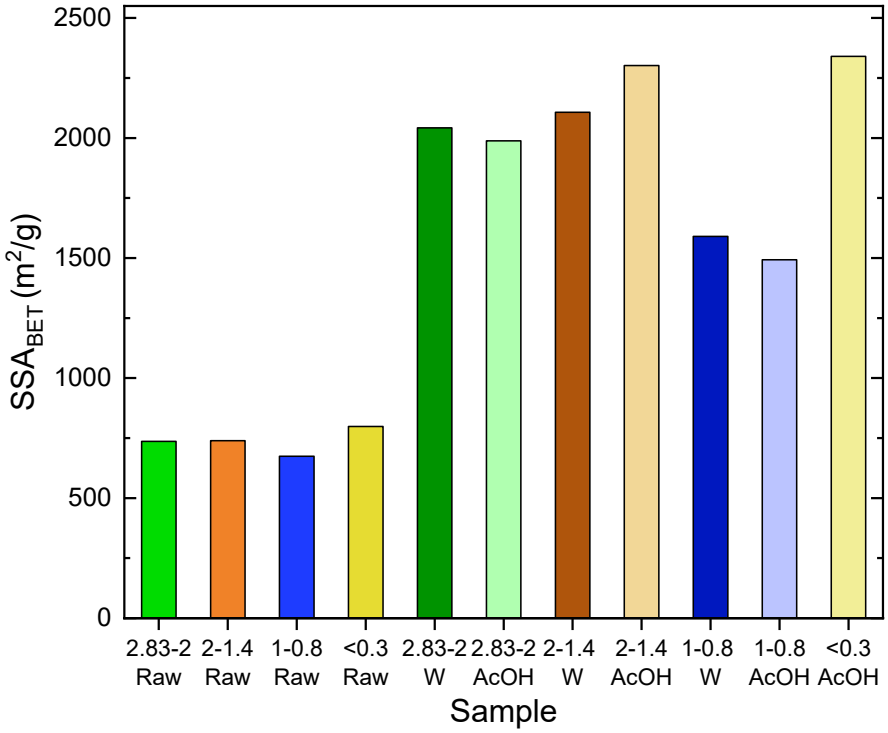

Figure 3.16: Column graph of Raw and activated samples with relative SSA_{BET} values.

For each Raw sample a specific color was chosen, which is the one that is used in a darker shade for the corresponding W activated sample, and in a lighter shade for the AcOH one. The first thing that can be noticed, as already said, is the much higher values of SSA after activation, with an increase factor that ranges from 2.2-2.9, higher than the one obtained by Park et al. for the same activation procedure [53]. This can be explained with the different nature of the starting materials, in terms of amount of different types of impurities. The first factor is the quantity of metal ions present in the SAC, which accumulate during its use as a water filter, and could react as catalysts at high temperature for the reaction between carbon and oxidizing agents, leading to pore development and increased surface area [53]. Another factor can be the different quantities of polymeric materials used as binders for the fabrication of the water filters. In fact, while these materials are non-porous and contribute negatively to the surface area of the Raw materials, they also are a valuable carbon source, and most of the available polymeric materials can be used to prepare activated carbons via a proper activation process [74]. This results in greater increase of surface area compared

to the starting material, since the initially low surface area polymeric material reacts with KOH to give additional porous structures.

Another fact that can be observed is the direct proportionality between the SSA of the non-activated and activated sample; in all cases, considering two Raw samples, one with higher surface area than the other, will respectively yield a W and AcOH sample with higher SSA with respect to the other one.

Something that is instead unclear is the effectiveness of the acid wash in raising the specific surface area value, as reported in literature [53]. In fact, this proves to be the case in only one of the three Raw samples activated, while for the other two the one washed with only water appears to be the one with the highest SSA, with generally small differences found. This fact will be discussed later in this study in paragraph 3.2.7.

The PSD of the activated samples was determined using the NLDFT model mentioned in Paragraph 2.3.1.3. The differential pore size distribution of these is illustrated in **Figure 3.17-3.20**, with each Raw sample compared with its activated W and AcOH counterparts. To have an even additional comparison of the samples after the activation process, the different W and AcOH PSD are shown together, for all the different granulometries, in **Appendix C**.

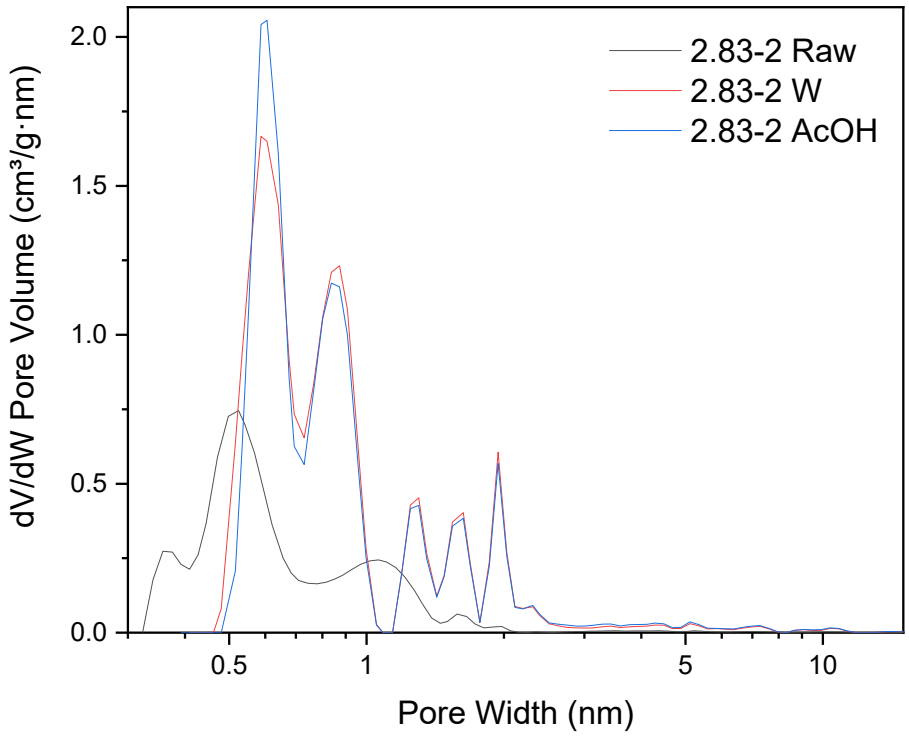

Figure 3.17: Differential pore size distributions for sample 2.83-2 Raw, 2.83-2 W and 2.83-2 AcOH.

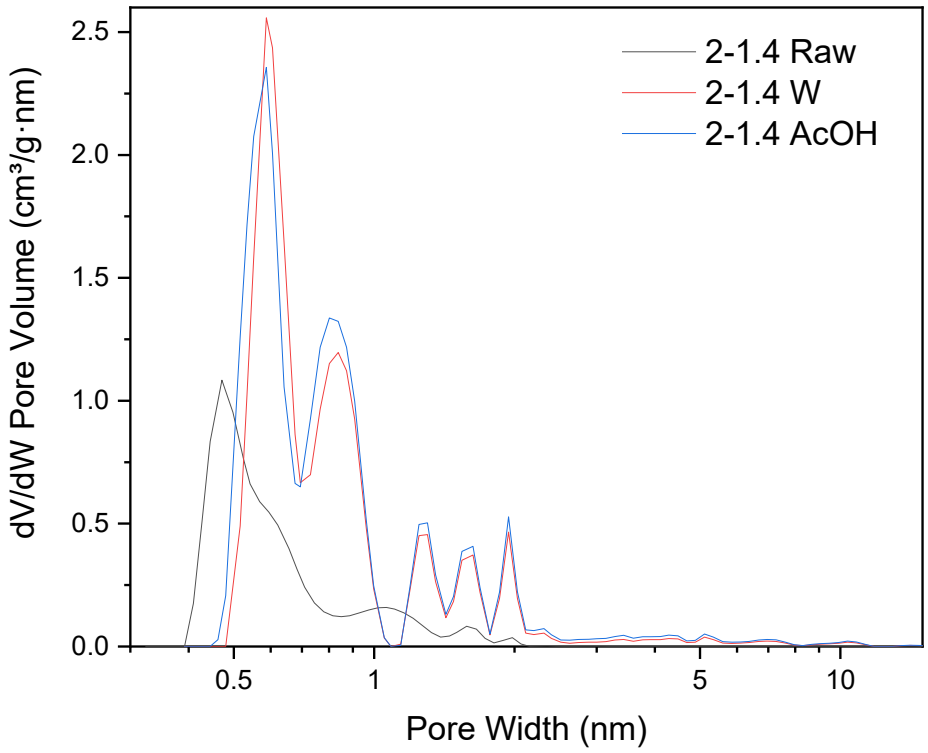

Figure 3.18: Differential pore size distributions for sample 2-1.4 Raw, 2-1.4 W and 2-1.4 AcOH.

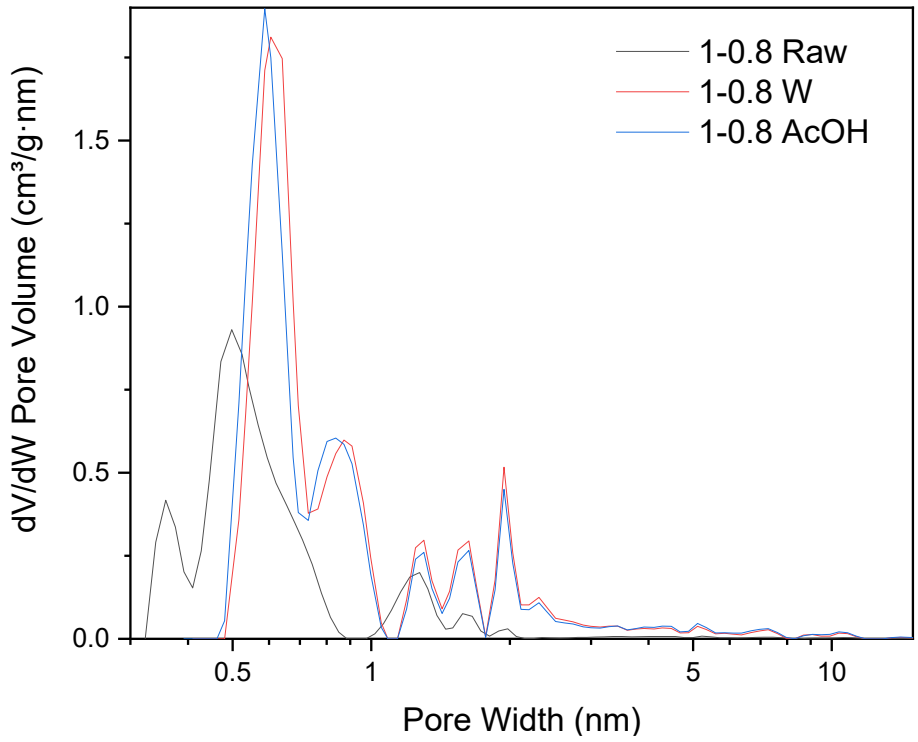

Figure 3.19: Differential pore size distributions for sample 1-0.8 Raw, 1-0.8 W and 1-0.8 AcOH.

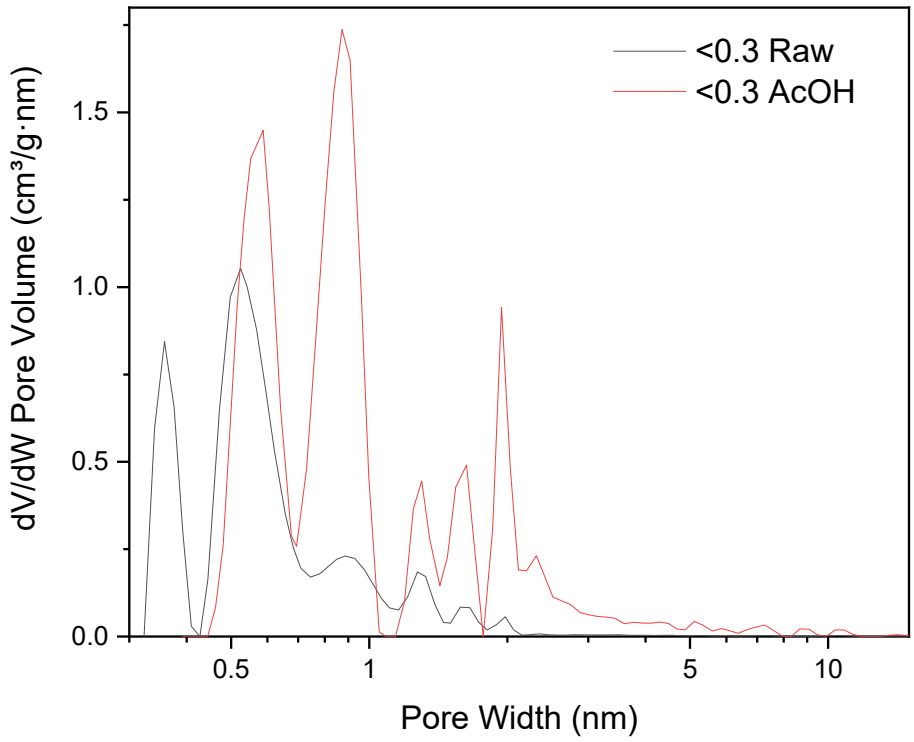

Figure 3.20: Differential pore size distributions for sample <0.3 Raw and <0.3 AcOH.

These curves were analyzed to determine different structural parameters that characterize the samples, which are the same listed in Paragraph 3.1.2. These are reported for each Raw, W and AcOH sample in **Table 3.4**. By looking at both the PSD curves and the values listed in the table, the first thing that can be noticed is the significant increase in pore volume after the activation process, with a factor that ranges from 2,5 to 3,2 even more than the one calculated for the SSA. It is also evident that the reaction with KOH produces an increase in the pore sizes [21], [74], which is reflected in a general shift of the PSD curves toward higher pore size values and the presence of discernible peaks at pore width > 2 nm. This pore size increase is also reflected in more multiple structural parameters:

- the maximum of the pore size is shifted for all samples from ~ 0.5 nm to ~ 0.6 nm;
- the relative increase in pore volume in activated sample is mostly reflected on the total and micropore volume, while a smaller increase is observable for ultra-micropores
- the degree of microporosity is sensibly lower for activated samples (< 80%) when compared to the Raw ones.

All of these confirm the development of bigger pores by the KOH activation, resulting in the production of a lot of bigger micropores and mesopores.

Table 3.4: List of Raw and activated samples and relative structural parameters obtained from their differential pore size distribution.

Sample	DFT total pore volume (cm^3/g)	DFT pore size (nm)	DFT cumulative pore volume (cm^3/g)		Micropore %
			Ultra-micropores	Micropores	
2.83-2 Raw	0.33	0.52	0.15	0.30	90
2.83-2 W	0.98	0.59	0.24	0.77	79
2.83-2 AcOH	0.98	0.61	0.24	0.74	76
2-1.4 Raw	0.30	0.47	0.18	0.30	100
2-1.4 W	1.02	0.59	0.30	0.80	78
2-1.4 AcOH	1.17	0.59	0.30	0.87	74
1-0.8 Raw	0.33	0.50	0.19	0.28	85
1-0.8 W	0.86	0.61	0.24	0.58	67
1-0.8 AcOH	0.84	0.59	0.23	0.55	65
<0.3 Raw	0.38	0.52	0.21	0.35	92
<0.3 AcOH	1.23	0.87	0.20	0.85	69

Another fact that can be noticed is that the development of the pore structure seems to be proportional to the non-activated SSA, which can be quite expected considering that a bigger surface area results in higher reaction kinetics [75]. This results, interestingly, in sample < 0.3 having the most drastic change in PSD. As a matter of fact, it presents the biggest total pore volume (and consequently bigger pores) obtained, and the biggest shift in pore size, going from 0.52 nm to 0.87 nm. As already explained for Raw samples, these major growths are in pore volume are not really reflected in the SSA values, since the development of bigger pores contributes greatly to the total volume of a material, but not quite as much to its surface. As noticed for the specific surface area, a lot of uncertainty is met when deciding what washing method proves to offer the most developed porosity, since, while the differences calculated in pore volume hardly are big, only in the case of 2-1.4 sample the AcOH sample can be identified as the one with bigger porosity.

3.2.3 SEM and EDS

In order to study the morphology of the sample pre and post activation, SEM images were taken for sample 2-1.4 Raw, W and AcOH (shown respectively in Figure **3.21-3.23**, with 5000x magnification images shown in **Appendix D**) and for sample 2.83-2 (shown in Figure **3.24-3.25**, with 10000x magnification shown in **Appendix D**).

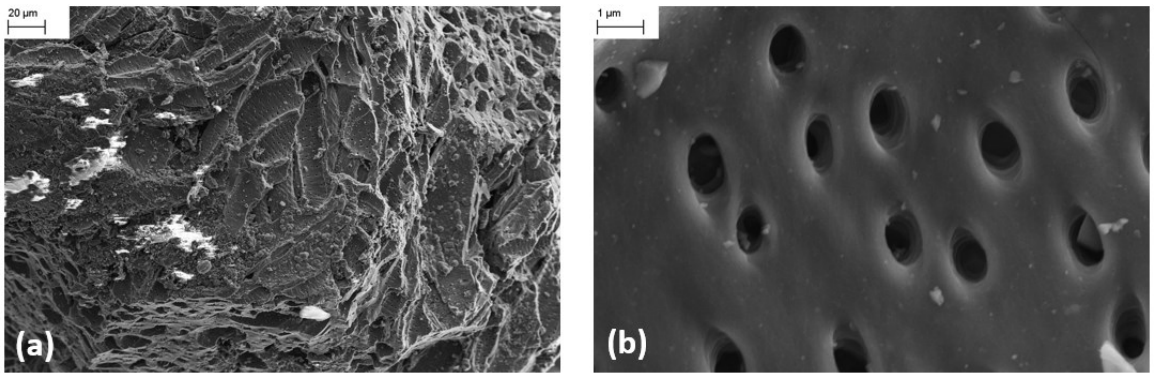

***Figure 3.21*:** (a) SEM image of sample 2-1.4 Raw, 1000x; (b) SEM image of sample 2-1.4 Raw, 25000x.

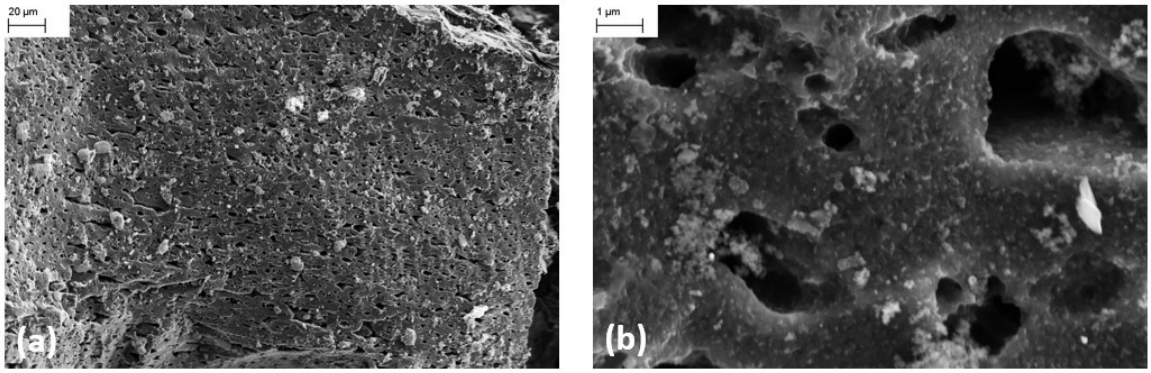

***Figure 3.22*:** (a) SEM image of sample 2-1.4 W, 1000x; (b) SEM image of sample 2-1.4 W, 25000x.

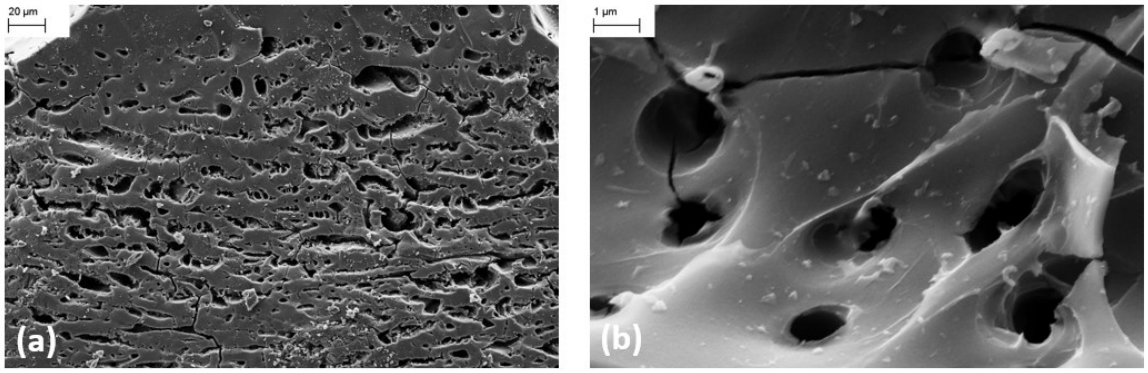

***Figure 3.23*:** (a) SEM image of sample 2-1.4 AcOH, 1000x; (b) SEM image of sample 2-1.4 AcOH, 25000x.

Looking at the various images, the porosity of the structure can be appreciated, visible in the form of big meso- and macropores (in order to see micropores, a HRTEM analysis would be necessary to reach such high magnifications). While for the Raw sample different zones can be found with quite regularly sized and distributed pores of widths ~ 50 nm, a drastic change can be noticed in the activated samples. Here, the pore network appears much more complex and developed, with a broader range of bigger and differently sized pores that are clearly interconnected. An interesting fact is that, compared with the Raw and AcOH samples, the W one appears to have a much more impure surface, observable in the white particles that cover the grains, which are presumably metal compounds (oxides) [76]. The same thing was observed for sample 2.83-2 W and 2.83-2 AcOH, with the surface of the first one appearing much more covered with impurities when compared to the second one. One thing that can be appreciated more clearly in particular for **Figure 3.25** is the roughness of the carbon surface, which, despite appearing to be flat at lower magnifications, is actually made up of really small micropores.

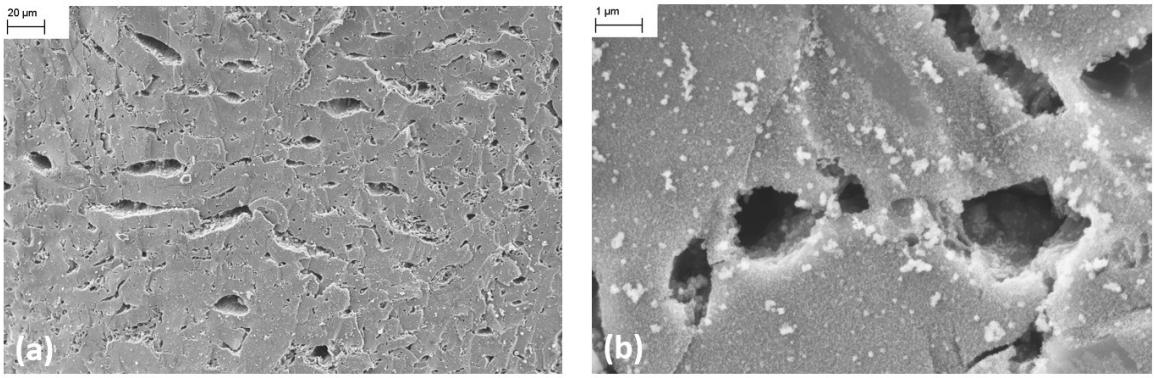

Figure 3.24: (a) SEM image of sample 2.83-2 W, 1000x; (b) SEM image of sample 2.83-2 W, 25000x.

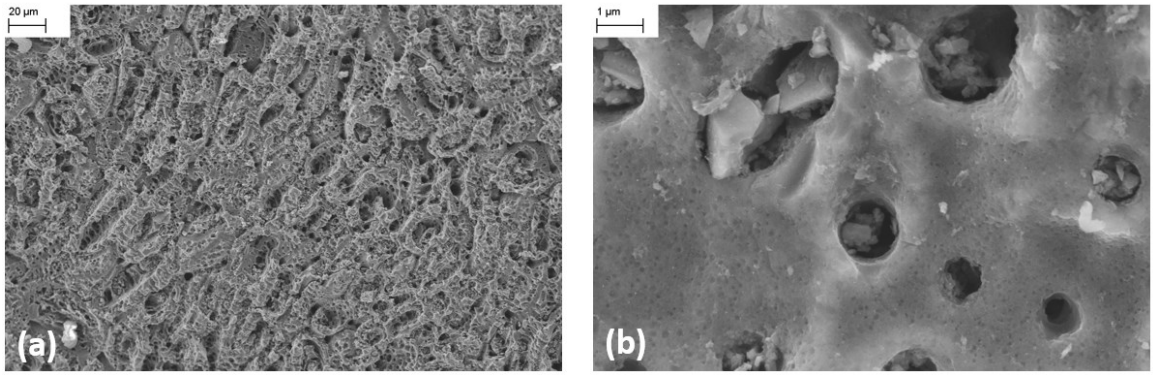

Figure 3.25: (a) SEM image of sample 2.83-2 AcOH, 1000x; (b) SEM image of sample 2.83-2 AcOH, 25000x.

In addition to SEM images, EDS analysis was performed on activated and non-activated 2-1.4 samples, obtaining data about the bulk composition of the sample, listed in **Table 3.5**.

Table 3.5: Composition (atomic%) of the 2-1.4 Raw, W and AcOH sample obtained via EDS analysis.

Element	2-1.4 Raw	2-1.4 W	2-1.4 AcOH
C	95.37	92.66	96.55
O	4.63	7.06	3.45

3.2.4 CHNS analysis

To obtain the most reliable data on the bulk composition of the sample, CHNS analysis was performed, which gave the results listed in **Table 3.6**.

Table 3.6: Composition (weight%) of the 2-1.4 Raw, W and AcOH sample obtained via CHNS analysis.

Element	**2-1.4 Raw**	**2-1.4 W**	**2-1.4 AcOH**	**Ref** [32]
C	77.77	85.78	84.68	95.15
H	2.51	0.15	0.18	0.55
O	19.72	14.07	15.14	4.00

These findings indicate that the SAC have quite a low degree of carbonization, with the presence of a high percentage of hydrogen and mostly oxygen when compared with other commercial ACs present in literature [32]. This can be explained with the previous use of the source material for water purification. The analyzed AC is indeed used for the dechlorination of water, a process that involves the oxidation of the carbon to reduce chlorine in the water into a non-oxidative and innocuous chloride ion, that then gets dissolved in the water [77]. Another factor to consider to explain the relatively lower amount of C in the material is the already mentioned presence of polymeric material in the filter matrix. Looking at the values for the activated samples, it can be seen that this high H and O content gets effectively and sensibly reduced with the production of volatile compounds that takes place during the activation process, raising the C content of the material [78].

3.2.5 XPS

The surface composition of the samples before and after activation was studied via XPS analysis, which was performed on sample 2-1.4 and 2.83-2. Since the results obtained were very similar, only the 2-1.4 will be shown as representative. The XPS Survey spectra obtained for the 2-1.4 Raw, W and AcOH samples are reported in **Figure 3.26**, while the XPS Survey spectra for the 2.83-2 sample can be found in **Appendix E**.

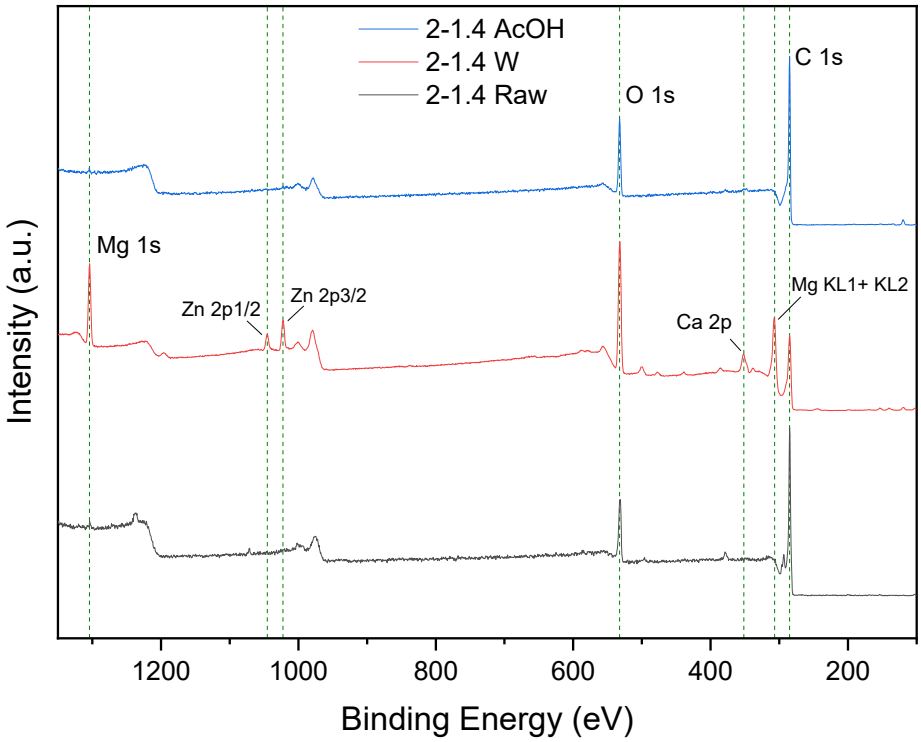

Figure 3.26: XPS Survey spectra obtained for sample 2-1.4 Raw, 2-1.4 W and 2-1.4 AcOH.

The spectrum obtained for the Raw sample clearly matches with the ones reported in literature [64], [79]. The main feature is the presence of two major peaks, one centered at binding energy 284.8 eV and the other at 532.2 eV, associated with, respectively, C1s and O1s. Other minor peaks present are instead around 978 eV and 1223 eV, and correspond to the Auger $KL_{23}L_{23}$ emission of oxygen and carbon. While the exact same peaks were found for the AcOH sample, the same cannot be said for the W one. What can be observed is actually the presence of additional peaks, aside the already mentioned ones. The major ones were found to be the following: Mg KL_1+KL_2 at 307.2eV, Ca2p at 351.5 eV, Zn2p$\frac{3}{2}$ at 1022.4 eV, Zn2p$\frac{1}{2}$ at 1045.0 eV, and Mg1s at 1304.0 eV [64]. All of these peaks were analyzed to have a quantification of the elements present on the surface of the samples. The values obtained are listed in **Table 3.7**. What was found was a surprisingly high amount of impurities, mostly Mg Al and Zn, with Mg reaching 11,70%, present in the W samples, which is instead not observed in both the sample before activation and the one washed with acetic acid. The reason behind this anomaly be discussed later in Paragraph 3.2.7.

Table 3.7: Composition (atomic%) of the 2-1.4 Raw, W and AcOH sample obtained via XPS analysis.

Element	2-1.4 Raw	2-1.4 W	2-1.4 AcOH
C	84.75	49.06	83.12
O	15.25	34.87	16.88
Mg	0.00	11.70	0.00
Al	0.00	2.41	0.00
Zn	0.00	1.96	0.00

3.2.6 XRD

The crystalline structure of the samples before and after activation was investigated via XRD analysis. **Figure 3.27** illustrates the diffraction pattern of the 2-1.4 Raw, W and AcOH samples, after background removal.

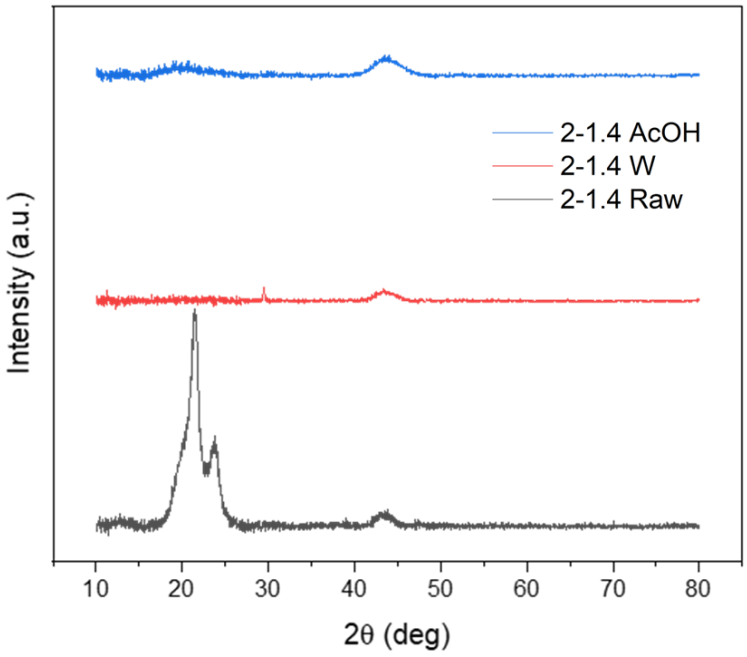

Figure 3.26: Diffraction pattern for sample 2-1.4 Raw, 2-1.4 W and 2-1.4 AcOH.

The pattern obtained for the Raw sample is in good agreement with similar ones reported in literature [69], [80], [81]. The diffractogram shows two very broad and asymmetric reflections, which, according to the X-ray diffraction theory, indicate the presence of defects

in the crystalline structures [82]. The most intense one corresponds to the reflection of (002) planes, and is divided into two different contributions, one centered around 2θ = 21.3°, while the other at 2θ = 23.7°. These can be attributed to, respectively, a mixed combination of crystalline regions with more defects and fewer defects, defined by Lee at al. as less-developed crystalline carbon (LDCC) and more-developed crystalline carbon (MDCC) regions [81]. The other reflection that can be noticed is the one centered at around 2θ = 43.0°, which is the result of the contribution of the (100) and (101) planes. Looking instead at the activated sample, once the background is subtracted the (200) reflection almost completely disappear, with only a small contribution from the (10l) reflections still noticeable. This indicates that the activation with KOH results in the destruction of the crystalline structures present in the starting material due to the intercalation of the K ions in the carbon planes [83], rendering the ACs quasi-exclusively amorphous. Interestingly, in the W pattern, a small reflection at 2θ = 23.7° can be found, probably indicating the presence of calcite, which is further confirmation of the formation of metal compounds on the surface of the material.

3.2.7 Discussion

Considering the results of all the analyses listed above, several conclusions were drawn about the studied materials. The chemical activation process with KOH has indeed produced much higher surface areas and pore volumes. A key role was played by the nature of the SAC in obtaining these high values comparing to the starting ones. Indeed, the particularly low SSA of the spent activated carbon was explained with the presence of polymeric materials (used as binders during fabrication) and metal impurities that stay adsorbed during the water filtration process. This is probably the cause for all the difficulties encountered while trying to obtain N_2 isotherms of all the Raw samples, since the polymeric part reduces greatly the porosity and surface area, resulting in small quantities of gas adsorbed, and ions interact strongly with the quadrupole moment of the nitrogen molecule. These cause the diffusion and equilibration process of N_2 to be very difficult, making it necessary to employ CO_2 as an adsorptive. The activation process results in the carbonization of the polymers, which turn into porous AC, but also in the formation of ashes, composed of metal oxides and other compounds, which tend to accumulate on the surface of the material [53]. This explains the fact that, while the bulk composition of the samples pre and post activation determined via EDS shows no discernible amount of impurities, the XPS results

indicate a strong presence of metal impurities, which is instead not found for the Raw and AcOH sample. This is proof of the fact that the metal impurities are already present in the SAC, but distributed in the bulk of the material and in such low quantities that they are not detected while analyzing the Raw samples. The chemical activation, as already said, causes the reaction of these metals and aggregation of the resulting ashes on the surface, which is at this point much more covered with impurities. The fact that these are not detected for the AcOH sample instead proves that the acid wash successfully dissolves the metal ions, effectively removing the ashes from the surface [53], [76]. This can also explain the uncertainties in determining which washing method results in the highest SSA and pore volume. In fact, while according to Park et al. the removal of the ashes should result in unclogging of the pores and thus higher surface area, these accumulate on the external surface, which is very small when compared to the high surface area of the micropores. Since these are not affected by the presence of ashes because of their extremely small widths, this results in the varying values of SSA observed with these washing procedures. While the external surface area and some bigger pores can be cleaned via treatment with acetic acid, this is not quite that relevant for the increase of SSA and pore volume, but instead, one can even postulate the fact that the ashes, by increasing the roughness of the surface, can bring a positive contribute to its surface area value. Considering all of this, it was concluded that, while not clearly effective in raising the surface area value of the activated product, the acid wash most definitely offers a much more clean and less impure product when compared to the one washed with only water, which is in important factor when considering its application for the storage of hydrogen. For these reasons, sample <0.3 was only washed with acetic acid, and chosen for the doping process due to its higher SSA.

3.3 Doping

As just said, sample <0.3 AcOH was the one chosen to be doped. To try and prevent the waste of any activated material, the doping process, described in Paragraph 2.2.2 was first performed on a Granular Activated Carbon (GAC) commercial sample. This was chosen since GAC is the same type of carbon that is used in the production of wastewater filters. In particular, the sample used was a GAC 1700, with 1700 standing for its iodine number (i.e., a quantity that indicates the surface area and porosity of the activated carbon and it is defined as the amount of iodine adsorbed by 1 g of carbon at the mg level [84]). For both

cases, considering the initial mass of AC, the yield of the doping process after the doping and heat treatment at 1100 °C steps stood around the 80% value.

3.3.1 GAC 1700

3.3.1.1 Adsorption Isotherms

First, N_2 adsorption and desorption isotherms were obtained for both the GAC 1700 and N-doped GAC 1700 samples, which, for clarity, will from now on be named GAC and N-GAC. In these cases, just as for the activated materials, using the Dosing function proved to be successful in obtaining the whole nitrogen isotherm, due to the purity and high surface area of the ACs. **Figure 3.27** shows the N_2 adsorption and desorption isotherm for GAC and N-GAC

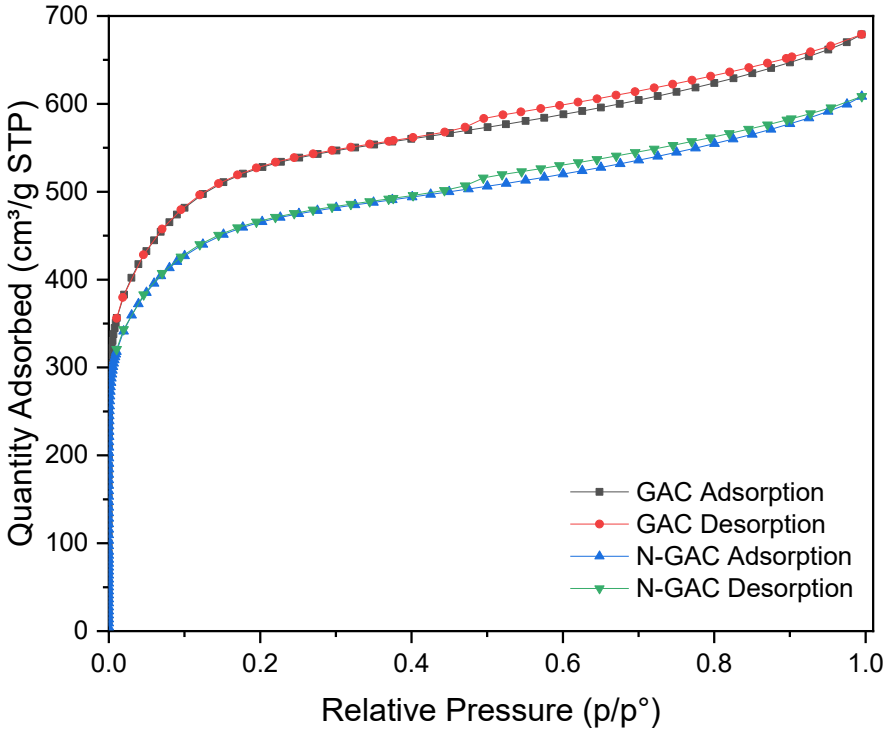

Figure 3.27: N_2 adsorption and desorption isotherms for sample GAC and N-GAC.

The isotherms appear very similar to the ones discussed in Paragraph 3.2.1 for the activated samples. In both cases in fact, a Type (b) curve can be observed, denoting a microporous material with presence of bigger micropores and small mesopores. Furthermore, even in this case the plateau is not really flat, indicating that the isotherm also has partly Type II and IV character, suggesting the presence of some macropores and mesopores.

Mesoporosity is additionally confirmed by the presence of a Type H4 hysteresis loop, with the typical desorption closure due to cavitation in the 0.4-0.5 p/p^0 range.

3.3.1.2 SSA and PSD

The SSA of the GAC and N-GAC was determined following same procedure explained for Raw and activated samples (explained in Paragraph 3.1.2). Again, the range in which the BET equation proved to be applicable was $0.01 \leq p/p^0 \leq 0.1$. In **Table 3.8** the SSA_{BET} values obtained for GAC and N-GAC are reported.

Table 3.8: List of undoped and doped GAC samples with relative SSA_{BET} values.

Sample	SSA_{BET} (m^2/g)
GAC	1961
N-GAC	1737

From the SSA values obtained, one can firstly see the quite high surface area of the commercial GAC, which then decreases after being doped. This is due to the surface functional nitrogen groups that are introduced in the material, which block part of the porosity [32]. The exact same thing was observed studying the PSD of the two samples, which is reported in **Figure 3.28**, with correlated structural parameters calculated as explained in Paragraph 3.1.2 and listed in **Table 3.9**.

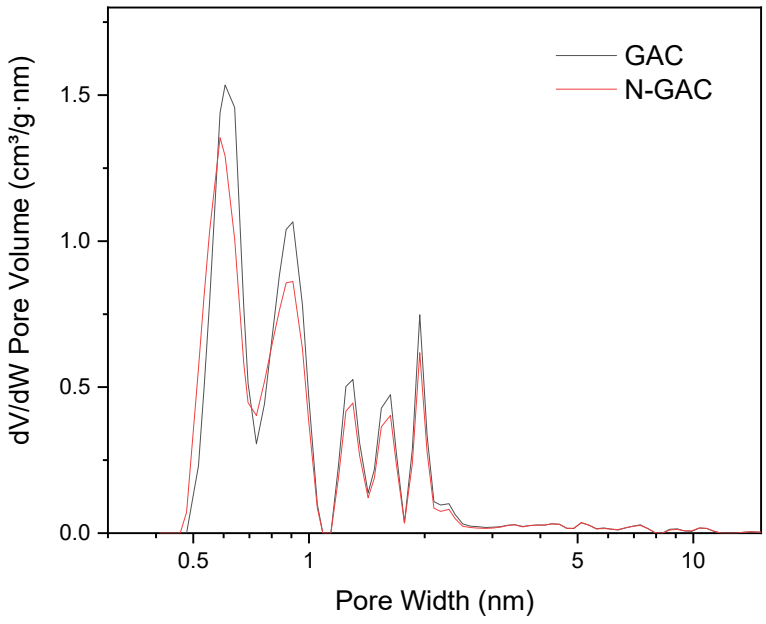

Figure 3.28: Differential pore size distributions for sample GAC and N-GAC.

Table 3.9: List of structural parameters obtained from the differential pore size distribution of GAC and N-GAC.

Sample	DFT total pore volume (cm^3/g)	DFT pore size (nm)	DFT cumulative pore volume (cm^3/g)		Micropore %
			Ultra-micropores	Micropores	
GAC	0.98	0.61	0.19	0.73	74
N-GAC	0.88	0.59	0.19	0.65	74

As mentioned above, the partial blockage of porosity can be observed in the lowering of the peaks of the differential pore size distribution, corroborated by the lower total pore volume, which goes from 0.98 to 0.88 cm^3/g, and the slight shift of the highest peak's maximum from 0.61 to 0.59 nm. Interestingly, this blockage seems to affect only pores with size bigger than 0.7 nm, as it can be seen from the unvaried ultra-micropore pore volume. This is probably due to steric hindrance, which prevents surface functional groups from forming inside, and therefore blocking, such small micropores.

3.3.1.3 CHNS analysis

To obtain the most reliable data on the bulk composition of the sample, CHNS analysis was performed, which gave the results listed in **Table 3.10**.

Table 3.10: Composition (weight%) of the GAC and N-GAC sample obtained via CHNS analysis.

Element	GAC	N-GAC
C	92.25	80.61
O	7.35	18.82
N	0	0.32
H	0.40	0.25

These values indicate that doping the sample with urea at 350 °C successfully introduced N atoms into the bulk of the sample. Along with nitrogen, an increase in the oxygen content can be observed. This is in accordance with the results obtained in the reference article [32],

and suggests that oxygen-containing groups are formed during doping with urea. This will be discussed more in depth later.

3.3.1.4 XPS

The surface composition of the samples during the doping process was studied via XPS analysis, which was performed at different temperatures in order to investigate the evolution of the N content in the material. These analyses were performed at 350 °C, with the sample undergoing just the first doping step of the process, then on a different sample heat treated at 900 °C, and ultimately on the sample treated at 1100 °C. Quantification of the elements present in the sample was performed on the survey spectra, obtaining the values listed in **Table 3.11**.

Table 3.11: Composition (atomic%) of the differently heat treated doped samples obtained via XPS analysis.

Element	350 °C	900 °C	1100 °C
C	86.61	89.22	91.33
O	4.90	5.19	8.15
N	8.49	5.59	0.53

Again, the obtained results proved the successful introduction of nitrogen at the surface of the GAC sample, as a consequence of doping with urea. Looking at the evolution of the composition with increasing temperature it can be noted that the heat treatment step results in a progressive removal of nitrogen species. This can be explained by thermal decomposition reactions involving urea-based functional groups [85]. Interestingly, an increase of oxygen can be observed, which is most presumably not actually due to an increase of absolute content of O atoms, but more a relative increase in the composition due to the removal of nitrogen species. This also suggests that some functional groups that form which contain oxygen might be more stable to high temperatures compared to ones containing only nitrogen. An example of these might be the formation of different chemisorbed nitrogen oxides [86], whose removal needs much higher temperatures. In addition, it was found that after annealing with ammonia, an increase in the concentration of surface carbonyl groups can be observed [87]. The appearance of these groups results from the chemisorption of oxygen when carbons are stored in the presence of moisture at room temperature.

The higher concentration of surface carbonyl groups on ammonia treated carbons suggests their higher ability to chemisorb oxygen with creating carbonyl moieties.

In order to evaluate the nitrogen speciation in the GAC sample, deconvolution of the N1s peak was performed on the samples treated at 900 °C and 1100 °C, the first of which is illustrated below in **Figure 3.29**.

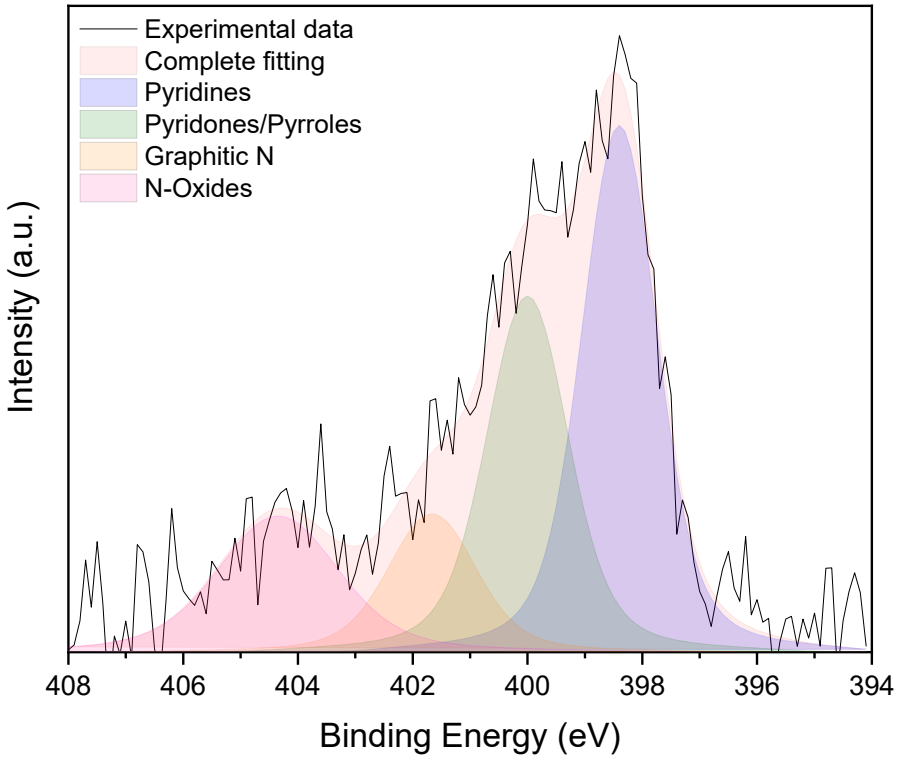

Figure 3.29: N1s spectrum of the N-CAG sample after heat treatment at 900 °C.

The spectrum shows the presence of different types of N species, as reported in literature. In fact, low-temperature treatments in the presence of urea, such as the one performed at 350 °C, lead to the formation of nitrogen groups on the carbon surface, such as amines (-NH_2) and imines (=NH), instead of N atoms embedded in the carbon planes [88]. After heat treatment in an inert atmosphere, these groups are converted into heterocyclic functionalities that can be observed in the N1s spectrum, which was deconvoluted into four different groups according to the literature [32], [86], [89], [90]. The peaks found can be attributed to pyridines (398.4 eV), pyrroles and/or pyridines (400.2 eV), graphitic nitrogen groups (i.e. quaternary nitrogen) (401.6 eV) and oxidized nitrogen functionalities (404.3 eV), with the latter confirming the hypothesis made while looking at the increased oxygen content in the sample after doping. Quantification of these peaks was performed for the 900 °C and 1100 °C treated samples, offering the results listed in **Table 3.12**. These results show a

decrease of the contribution of pyridines and pyridines/pyrroles at higher temperatures, as well as an increase of graphitic nitrogen. These changes can be explained by the greater thermal stability of graphitic nitrogen groups (which also explains the percentage increase of chemisorbed N-oxides) and the conversion of pyridines and pyridone/pyrrole species into graphitic nitrogen species through condensation reactions at high temperature [86], [90].

Table 3.12: Composition (atomic%) for each kind of nitrogen species of the differently heat treated doped samples obtained via XPS analysis, with associated relative percentage (considering the total N content of the sample).

N species	900 °C	1100 °C
Pyridines	2.28 (41%)	0.17 (32%)
Pyridones/Pyrroles	1.67 (30%)	0.00 (0%)
Graphitic N	0.71 (13%)	0.18 (34%)
N-Oxides	0.93 (16%)	0.18 (34%)

This conversion proceeds in the edges of the carbon layers, leading to the formation of edge-type graphitic species, and the mechanism that was proposed by Pels et al. is the following (also represented in **Figure 3.30)**: pyridones and pyrrolic N species tend to convert into pyridines at temperatures above 600 °C through the loss of oxygen from pyridones and the expansion of pyrrole rings; however, such pyridines are also converted into edge-type graphitic nitrogen species if high temperature treatments are used.

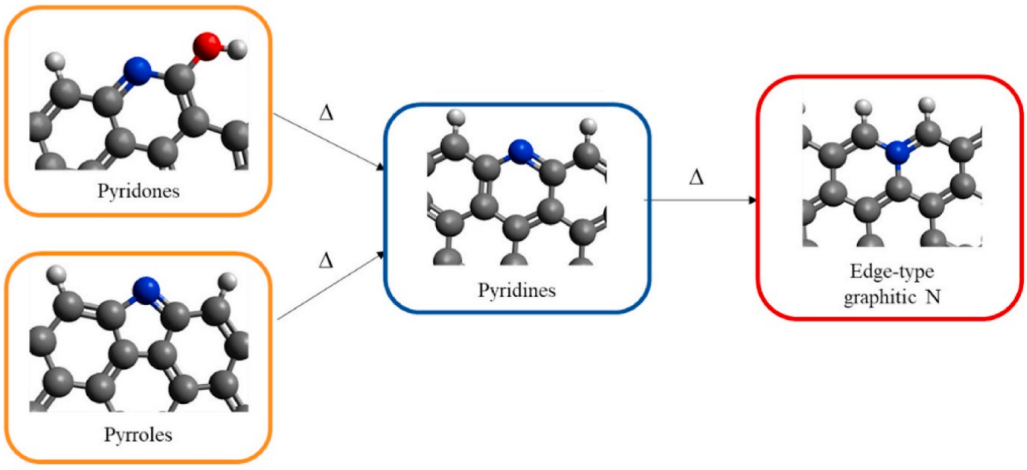

Figure 3.30: Schematic illustration of the conversion of pyrroles and pyridones into pyridines and the conversion of pyridines into edge-type graphitic nitrogen [32].

Considering the loss of surface area and porosity caused by the introduction of nitrogen groups in the material, N species like the one obtained after high temperature treatment, can be the ones that are the most desirable for hydrogen storage applications, considering the lower steric hindrance compared to, for example, pyridone groups.

After all of the results obtained, that proved the successful doping of the GAC sample with nitrogen, doping of the <0.3 AcOH activated sample was performed.

3.3.2 Activated Carbon Doping

3.3.2.1 Adsorption Isotherms

Again, N_2 adsorption and desorption isotherms were firstly obtained for both the <0.3 AcOH and N-doped <0.3 AcOH samples (from now on named N-<0.3 AcOH), and they are shown below in **Figure 3.31**.

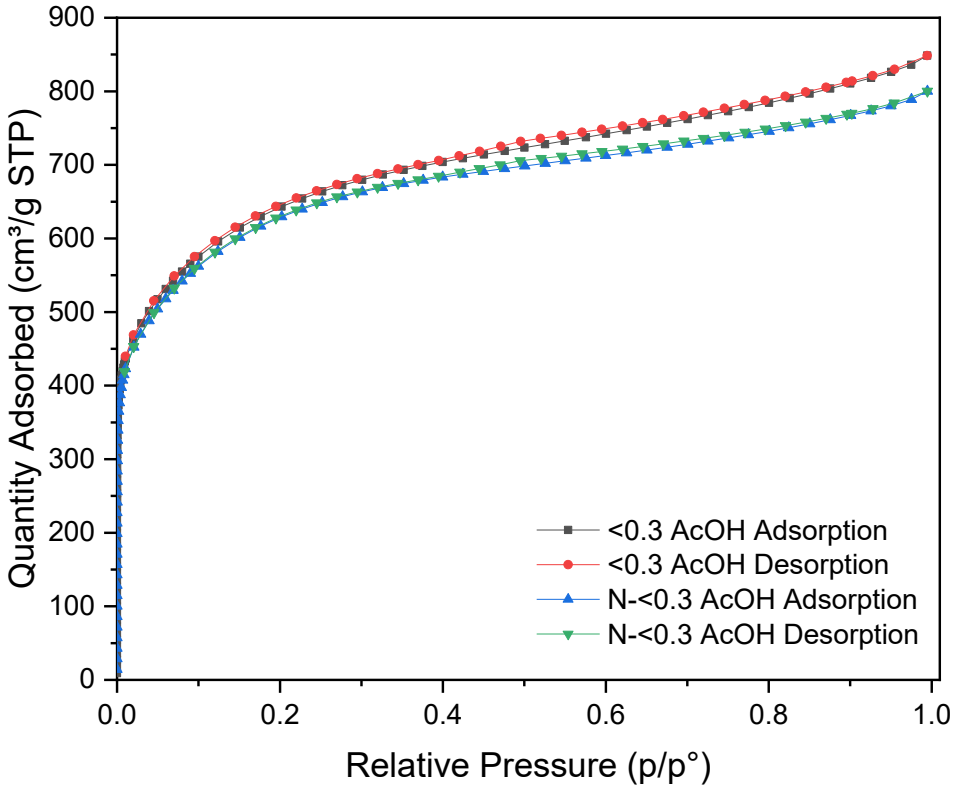

Figure 3.31: N_2 adsorption and desorption isotherms for sample <0.3 AcOH and N-<0.3 AcOH.

Once again, the isotherms are almost identical to the ones obtained for the commercial sample, whose description can be found in Paragraph 3.3.1.1. The only difference that can be spotted is the smaller decrease in the quantity adsorbed for the doped sample compared to the undoped one, which will be discussed more in depth later.

3.3.2.2 SSA and PSD

The SSA of the samples before and after doping was determined following same procedure explained for Raw and activated samples (explained in Paragraph 3.1.2). The range in which the BET equation could be applied was once again $0.01 \leq p/p^0 \leq 0.1$. In **Table 3.13** are reported the SSA_{BET} values obtained for <0.3 AcOH and N-<0.3 AcOH.

Table 3.13: List of undoped and doped <0.3 AcOH samples with relative SSA_{BET} values.

Sample	SSA_{BET} (m^2/g)
<0.3 AcOH	2340
N-<0.3 AcOH	2292

From the SSA values obtained, a decrease of surface area can be noticed going from the undoped to the doped sample, just as observed for GAC, resulting from surface functional nitrogen groups that are introduced in the material, which block part of the porosity. In this case though, the loss of surface area seems to be minor when compared to the one observed for the commercial doped sample. This could be attributed to a greater presence of bigger pores in the activated sample compared to the GAC, which are less likely to be obstructed by nitrogen functionalities. The PSD of the two samples is reported in **Figure 3.32**, with correlated structural parameters calculated as explained in Paragraph 3.1.2 and listed in **Table 3.14**.

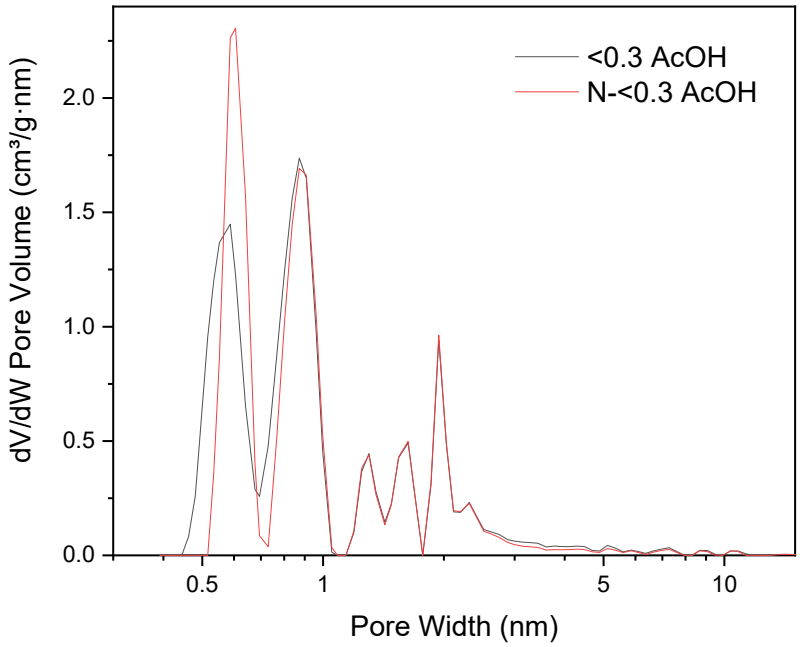

Figure 3.32: Differential pore size distributions for sample <0.3 AcOH and N-<0.3 AcOH.

Table 3.14: List of structural parameters obtained from the differential pore size distribution of <0.3 AcOH and N-<0.3 AcOH.

Sample	DFT total pore volume (cm^3/g)	DFT pore size (nm)	DFT cumulative pore volume (cm^3/g) Ultra-micropores	Micropores	Micropore %
<0.3 AcOH	1.23	0.87	0.20	0.85	69
N-<0.3 AcOH	1.16	0.61	0.22	0.84	72

As for GAC, the partial blockage of porosity is noticeable in the downward shift of some of the peaks of the differential pore size distribution, along with the lower total pore volume, which goes from 1.23 to 1.16 cm^3/g. Quite unexpectedly, after doping, a rearrangement of the peak at 0.6 nm can be observed, which sharpens and becomes higher in intensity than the one at 0.87 which was instead the major one in the undoped sample. This increase of pores with 0.6 nm width can be explained, on one hand, with the partial blockage of bigger pores, that consequently appear to have lower surface area, a fact that is confirmed by the decrease of total and micropore pore volume, along with an increase of ultra-micropore pore volume, and also micropore %. On the other hand, the disappearance of some of the smallest pores present at around 0.5 nm could be due to the reactions involved in the doping process, which produces different volatile compounds (mainly HNCO, NH_3 and CO_2) and could cause the widening of some pores [91]. This is also in accordance with results obtained with carbons annealed in the presence of ammonia (which urea decomposes into) which showed an increase in pore diameter [86].

3.3.2.3 CHNS analysis

CHNS analysis was performed on the <0.3 AcOH and N-<0.3 AcOH samples to determine their bulk composition, obtaining the results listed in **Table 3.15**. These values prove that, similarly to the commercial material, doping with urea at 350 °C was successful in introducing N atoms in the bulk of the activated sample.

Table 3.15: Composition (weight%) of the <0.3 AcOH and N-<0.3 AcOH sample obtained via CHNS analysis.

Element	<0.3 AcOH	N-<0.3 AcOH
C	89.23	93.05
O	10.48	6.39
N	0	0.41
H	0.29	0.15

One thing to note is that the N percentage obtained is higher than the one obtained for the GAC bulk analysis after the same doping process. This can be explained by two facts, with the first one being the much higher SSA of the activated sample, meaning faster reaction kinetics, and the second explanation being instead the higher amount of oxygen present in the <0.3 AcOH sample compared to the GAC. In fact, Pietrzak et al. found that, for a similar doping process with urea, the quantity of incorporated nitrogen is dependent on the oxygen content in the starting sample [92]. In this case, differently from the GAC, the oxygen content decreases after doping and heat treatment at 1100 °C, which is actually the case reported in literature by Quílez-Bermejo et al. [32]. As a matter of fact, while the oxygen content increases after doping with urea, as observed for the commercial sample, the high temperature treatment is expected to carbonize the material, releasing volatiles and increasing its C content [78]. In this case, differently from the previous one, it can be hypothesized that less temperature-resistant oxygen-containing functional groups were formed during the doping process. This will be verified later with via XPS analysis.

3.3.2.4 XPS

The surface composition of the samples after the doping process was studied via XPS analysis, which in this case was only performed at 1100 °C due to the scarce availability of the activated material, which needs to be produced via activation, when compared to the commercial one, of which a large amount was provided by ThinkWater. Quantification of the elements present in the sample was performed on the survey spectrum, which gave the results listed in **Table 3.16**, confirming the introduction of N atoms in the surface of the sample.

Table 3.16: Composition (atomic%) of the N-<0.3 AcOH sample obtained via XPS analysis.

Element	1100 °C
C	82.14
O	15.55
N	2.32

As for the commercial sample, deconvolution of the N1s peak was carried out in order to evaluate the nitrogen speciation. The peaks observed were the same reported for the N-GAC heat treated at 1100 °C, and their quantification gave the results listed in **Table 3.17**. For a clearer comparison, the values previously reported for the N-GAC sample are also reported.

Table 3.17: Composition (atomic%) for the N-<0.3 AcOH and N-GAC samples obtained via XPS analysis, with associated relative percentage (considering the total N content of the sample).

N species	N-<0.3 AcOH 1100 °C	N-GAC 1100 °C
Pyridines	1.39 (60%)	0.17 (32%)
Pyridones/Pyrroles	0.00 (0%)	0.00 (0%)
Graphitic N	0.79 (34%)	0.18 (34%)
N-Oxides	0.14 (6%)	0.18 (34%)

Looking at both tables, the first things that can be noted are the higher quantities of N compared to the N-GAC case, for the same reasons explained during the discussion of the bulk composition. This bigger amount of N is reflected in the higher percentage of pyridines in the N-<0.3 AcOH sample (60% vs 32%), which, being present in higher quantities, are not as much converted into graphitic species as in the previous case, and would need higher heat treatment times or temperatures for further conversion [32]. Additionally, a significantly lower percentage of N-oxides can be observed in the activated sample compared to the commercial sample, confirming the reason hypothesized for the lower presence of oxygen observed for <0.3 AcOH.

In conclusion, all of these results confirm that the activated <0.3 AcOH sample was successfully doped with nitrogen atoms, obtaining species such as graphitic N that do not affect its surface area significantly.

4 HYDROGEN UPTAKE

4.1 Raw and Activated Samples

Ultimately, after all the characterizations of the materials produced, hydrogen uptake measurements were performed as explained in Paragraph 2.3.6. H_2 adsorption isotherms were obtained in the absolute pressure range 0-850 mmHg (the maximum pressure obtainable with the ASAP 2020 Plus instrument) for the Raw 2-1.4 sample and all the activated W and AcOH samples, in order to compare their performance. All these curves are reported below in **Figure 4.1**.

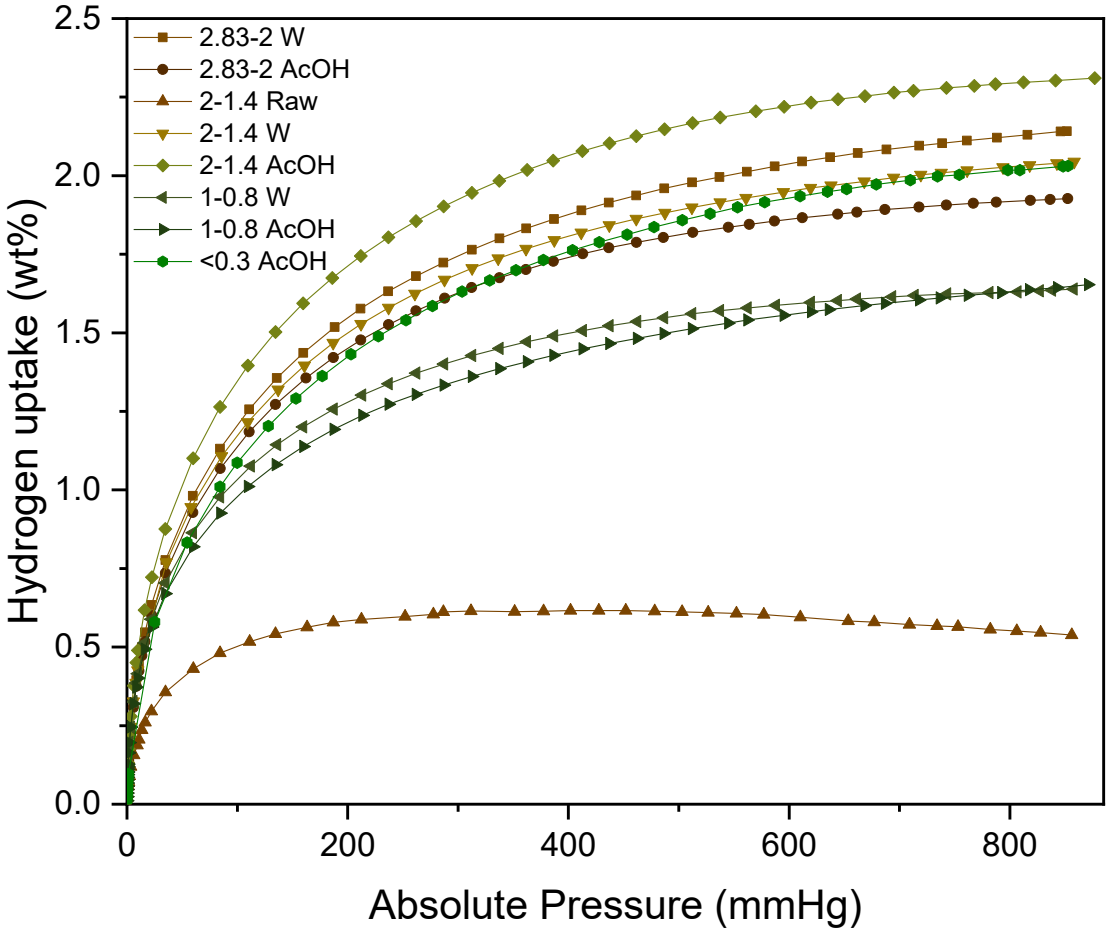

Figure 4.1: H_2 adsorption isotherms for sample 2-1.4 Raw and all activated W and AcOH samples.

To have an optimal confrontation of the H_2 storage capacity of the different samples studied and the values reported in literature, the hydrogen uptake at 1 bar (corresponding to ~750 mmHg) was determined from the isotherms, obtaining the results listed in **Table 4.1**.

Table 4.1: Hydrogen uptake (wt%) at 77 K and 1 bar for the 2-1.4 Raw and activated W and AcOH samples.

Sample	H_2 uptake (wt%)
2.83-2 W	2.11
2.83-2 AcOH	1.91
2-1.4 Raw	0.56
2-1.4 W	2.01
2-1.4 AcOH	2.28
1-0.8 W	1.62
1-0.8 AcOH	1.62
<0.3 AcOH	2.00

Looking at both the isotherms and the hydrogen uptake values, the first thing that can be noticed is the very scarce performance of the Raw sample, with hydrogen capacity only reaching 0.56 %, deriving from its impure nature and low surface area. The small quantities adsorbed serve as an explanation for the fact that its adsorption curve seems to decrease after a certain pressure, indicating an under-equilibrated analysis with erroneous results, which were the same obtained for different analyses on Raw materials. Due to these being non reliable, only the case of the 2-1.4 Raw sample was reported as representative. For the activated samples instead, correct Type I isotherms are obtained, with H_2 storage values ranging from 1.62% to 2.28%. Some irregularities can be found in all the isotherms regarding the spacing of the points taken, caused by the instrument's difficulties in stabilizing at the absolute pressure selected by the user. However, this doesn't affect the validity of the measurements, since the correct corresponding gas quantity adsorbed is calculated for each pressure reached. Also, some differences can be spotted in the slopes of the curves after the initial steep uptake, with some samples exhibiting higher continuous increase in uptake at increasing pressure, indicating weaker interaction between hydrogen molecule and the

surface of samples [93]. The binding energy could instead be represented by the initial slope of the isotherm, and is correlated to the widths of the pores present in the sample [83]. To better investigate this and to determine the parameters that are the most relevant in determining the hydrogen adsorption capacity of these materials, the H_2 uptake values at 77 K and 1 bar were correlated with the SSA_{BET}, the total pore volume, and the ultra-micropore pore volume, respectively shown in **Figure 4.2, 4.3** and **4.4**.

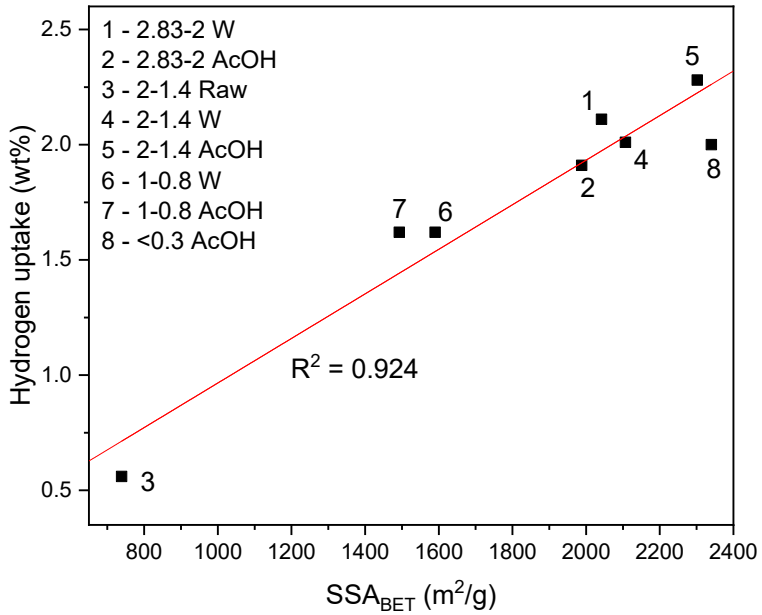

Figure 4.2: Hydrogen uptakes at 77 K and 1 bar as a function of the SSA_{BET} for 2-1.4 Raw and activated samples.

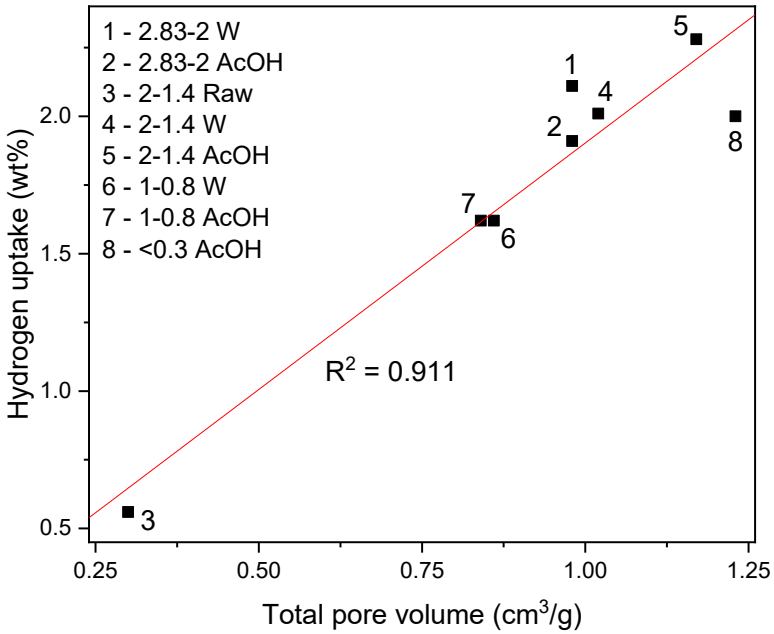

Figure 4.3: Hydrogen uptakes at 77 K and 1 bar as a function of the total pore volume for 2-1.4 Raw and activated samples.

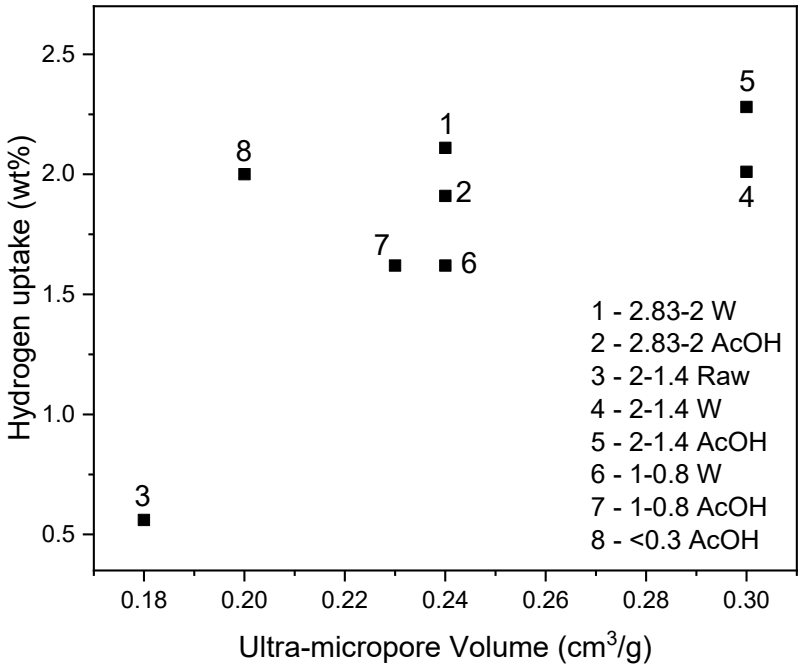

Figure 4.4: Hydrogen uptakes at 77 K and 1 bar as a function of the ultra-micropore pore volume for 2-1.4 Raw and activated samples.

All the samples show a roughly linear correlation of H_2 uptake with the SSA and total pore volume, with R^2 values respectively equal to 0.924 and 0.910, while a linear trend can only vaguely be observed in the case of ultra-micropore pore volume, but not clear enough to perform a satisfying linear fit. The first result agrees with several works [93]–[96] affirming that hydrogen uptake at 77 K linearly increases with BET surface area. The correlation with total pore volume is also in agreement with various results found in literature [93], [97], showing the pore volume is a relevant factor in determining the hydrogen adsorption of the materials. However, as the higher R^2 suggests, the SSA plays a bigger role if compared to the total pore volume, considering that, as already mentioned, bigger pores contribute a lot to pore volume, but not as much to surface area, resulting in a lower interaction between the H_2 molecule and the adsorbent. Interestingly, while the linear relationship between hydrogen uptake and ultra-micropore volume is not quite as strong, differently from other works [74], the influence of their presence can be noted quite clearly observing the discrepancies noted in the H_2 storage-SSA relationship for some samples. In fact, in the most evident example, while the <0.3 AcOH sample was the one with the highest SSA (2340 m^2/g), its performance falls short in comparison with other samples characterized by lower SSA, particularly 2-1.4 AcOH, which reaches the highest hydrogen uptake value (2.28%). This is easily explained by the lower presence of ultra-micropores in the <0.3 AcOH sample (0.20 cm^3/g) when compared to the other activated samples (0.23-0.30 cm^3/g) as was

previously observed and reported in Paragraph 3.3.2 in **Table 3.4**. In fact, as reported in numerous works, micropores [97], and in particular, small micropores in the range 0.5-0.7 nm [74], [93], [98], [99] are the ones that offer the highest hydrogen uptake per accessible surface area, due to the stronger surface-H_2 interactions resulting from the overlap of potential fields from both sides of the pores. In particular, a pore size of about 0.6 nm was found to be the optimal one for H_2 storage, since it can hold two layers of adsorbed hydrogen [100], [101]. Considering all of this, the high hydrogen storage performance of the 2-1.4 AcOH sample can be explained by the presence of a high SSA, aided by a high ultra-micropore volume, which consequently proves to be a relevant parameter in determining the H_2 uptake of a material, despite not as much as its surface area and total pore volume.
In ultimate analysis, for the purpose of comparing the hydrogen performance of the activated samples washed with water or acetic acid, the 1-0.8 W and AcOH samples can be taken into consideration, since the other two pairs differ too much in either SSA or pore volume to give a clear comparison. What can be observed is that the 1-0.8 AcOH sample, while showing a SSA, total pore volume and ultra-micropore volume that are a bit lower than its W counterpart, also presents the same storage capacity as the latter. This indicates that the acid wash with acetic acid offers a purer material with more hydrogen adsorption capacity, even though with not really drastic improvements, which is quite expected considering that the ashes accumulate on the external surface of the material, which represents a very small fraction of the total surface area in comparison to the microporous structure.

4.2 N Doping

Lastly, after the evaluation of H_2 storage capacity for the Raw and activated samples, hydrogen uptake measurements were performed on the samples that were functionalized with nitrogen, in order to verify its effectiveness in raising the quantity of H_2 adsorbed by the sample. As for the previous case, hydrogen adsorption isotherms were obtained in the absolute pressure range 0-850 mmHg, for samples GAC, N-GAC, <0.3 AcOH and N-<0.3 AcOH, which are reported below in **Figure 4.5**.

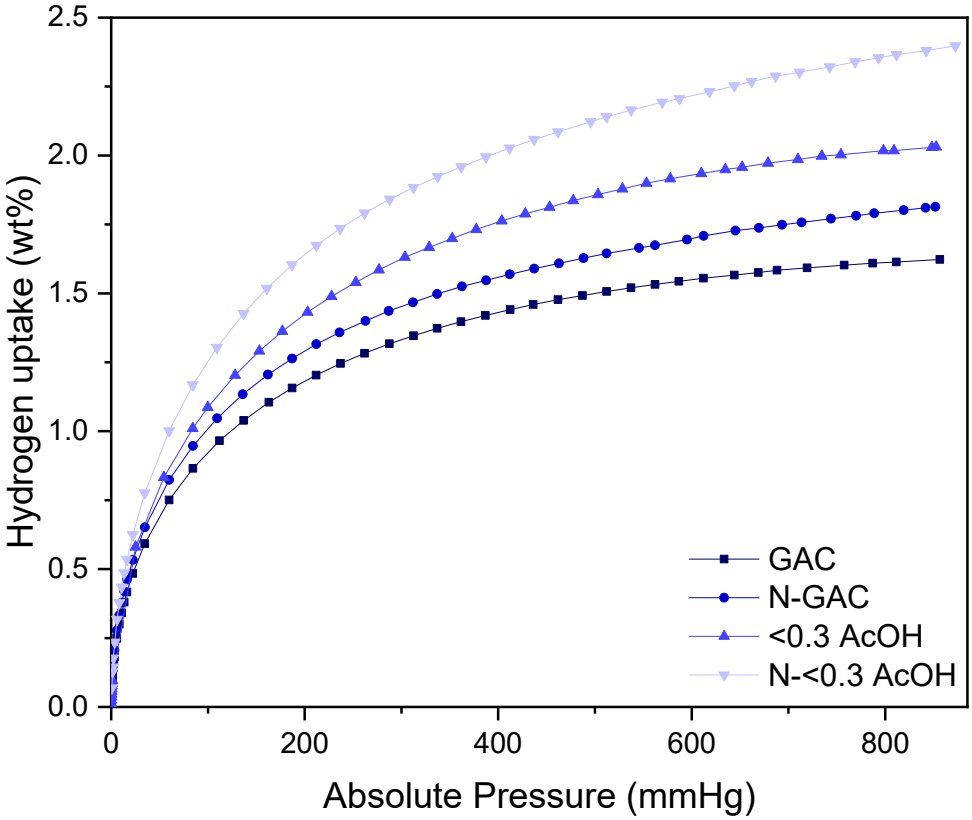

Figure 4.5: *H_2* adsorption isotherms for undoped and doped GAC and <0.3 AcOH samples.

Similarly to what has been done for the previous samples, the hydrogen uptake at 1 bar (corresponding to ~750 mmHg) was determined from the isotherms to better compare the sample's hydrogen storage performances, obtaining the values reported in **Table 4.2**.

Table 4.2: Hydrogen uptake (wt%) at 77 K and 1 bar for the undoped and doped GAC and <0.3 AcOH samples.

Sample	H_2 uptake (wt%)
GAC	1.60
N-GAC	1.77
<0.3 AcOH	2.00
N-<0.3 AcOH	2.33

The Type I isotherms and values obtained show a clear improvement of the hydrogen adsorption capacity after the functionalization with nitrogen, for both the commercial and activated carbon sample. In fact, as already mentioned in Paragraph 1.1, N atoms are among

the most often introduced heteroatoms, due to their positive effect demonstrated by various works [22], [93], [97], [102], [103]. Zhu et al. [104] theoretically investigated the interaction between hydrogen atoms and nitrogen-doped carbon materials and found that the electronic properties of N-doped carbons were theoretically predicted to change drastically by the presence of the heteroatoms due to their higher electronegativity than that of carbon. This results in nitrogen atoms being able to attract electrons of the neighboring carbon atoms, making them electron deficient. Since hydrogen is likely stabilized by transferring an electron to the carbon during the adsorption process, it prefers to adsorb on top of the nitrogen-neighboring carbon atoms. Thus, substituted nitrogen atoms increase the adsorption energy of hydrogen atoms on top of the neighboring carbon atoms rather than provide a new adsorption site on the top of the nitrogen atom, consequently increasing the H_2 storage capacity of the material.

In particular, for the analyzed sample, an 11% increase in the hydrogen uptake value was observed for the GAC sample, while a 17% increase was instead measured for the <0.3 AcOH sample. These different values, could be explained with the smaller loss in surface area after doping for sample <0.3 AcOH, as it was found in Paragraph 3.3.2.2, and also the higher quantity of nitrogen introduced in this sample (0.41%) compared to the commercial one (0.32%).

4.3 Discussion

Considering the results of all the analyses listed above, some conclusions can be drawn about the studied materials. Overall, at first glance the hydrogen uptakes measured for the activated materials might seem quite far from the requirements of the ultimate full fleet (UFF) US Department of Energy (US DOE) on-board hydrogen storage capacity target of 7.5 wt%. In actuality, these appear much more interesting when looking at the results found recently by different studies [98], [105]–[110] investigating a number of microporous carbon materials based on natural and synthetic precursor, which were transformed into porous activated carbons by carbonization followed by KOH activation. These materials were found to exhibit excellent hydrogen adsorption capacity, listed in **Table 4.3,** with the highest hydrogen uptakes at 77 K and 1 bar reported for any natural and synthetic material-derived AC (as of 2015) being 3.28% from hemp stem [110] and 2.85% from petroleum pitch [105].

Table 4.3: Hydrogen storage at 77 K and 1 bar over KOH-activated carbons derived from natural and synthetic precursors.

Activated carbons	Precursor (natural/synthetic)	H_2 uptake (wt%)	Reference
NAC-1.5-600	1,3 bis(cynomethyl imidazolium) chloride	2.96	[98]
PBA	Petroleum residue	2.84	[105]
CAC1	Corncob	2.85	[106]
Ch800/700/3	Chitosan	2.95	[107]
C2-1/4-700	Cellulose	2.50	[108]
CAC4	Corncob	3.21	[109]
AC8b	Hemp stem (Cannabis sativa L.)	3.28	[110]

These results highlight the potential of the ACs produced in the course of this study, mainly taking into consideration the samples produced that gave the best hydrogen adsorption performance, such as 2-1.4 AcOH with its 2.29% value. In fact, this appears very promising, and a good starting point for further optimization of different parameters that could lead to a much better performance, such as the carbon:KOH ratio (W), which, according to literature, gives optimal H_2 uptake when W = 3. Other parameters which proved to be relevant and on which further work can be done to achieve better results are the textural parameters of the material, SSA, pore volume, and in particular volume of pores smaller than 0.7 nm. Relevant improvements were also obtained via doping the ACs with nitrogen, which proved that functionalization with urea can successfully increase the hydrogen adsorption capacity of carbon materials. Considering the very low amount of N heteroatoms introduced in the material (0.32-0.42%), a further increase of H_2 adsorbed can be hypothetically found by functionalizing the material with higher quantities of dopant. However, an optimal degree of nitrogen substitution should be researched, since excessively nitrogen-rich conditions could end up being detrimental. The cause of this can be first found in the decrease of surface area that follows functionalization [111], but also in an observation suggested by Zhu et al. In fact, in their theoretical study, they found that the presence of nitrogen may

act to reduce the overall interaction between hydrogen and the carbon surface thus influencing the overall hydrogen uptake capacity. This, according to Zhu, occurs if hydrogen is adsorbed on neighboring carbon atoms, as discussed, but also on the nitrogen atoms. While adsorption on carbon atoms that neighbor nitrogen is strengthened due to the electron withdrawing nature of the later, this positive effect is counterbalanced and won over by the instability of adsorbing hydrogen atop the nitrogen. Experimentally, such a scenario would exist under high hydrogen coverage conditions, in which a maximum or near maximum of available sites are used for adsorption. This was observed for pressure above 10 bar and high hydrogen coverage conditions (4%) by Xia et al. [97]. Consequently, carbon surfaces that are too nitrogen-rich can result in lower hydrogen storage capacity due to there being less carbon sites for H_2 adsorption.

Ultimately, the hydrogen uptake results obtained by recycling ACs from exhausted water filters appear satisfying, and even more promising considering the recent advancements in the technology of cryo-adsorption and compression of gas [14], [112]. This is a novel approach that involves the adsorption of hydrogen on high surface area materials at cryogenic temperatures and moderate pressures and has several advantages over other methods because the process is performed at higher temperatures, 77 K, compared to liquefaction systems using temperatures around 20 K, and at lower pressures, 10-15 MPa, compared to pure compression systems using 70 MPa. In particular, carbon materials showed high potential for this application, and, considering the higher pressures employed in comparison with the values obtained for this study at 1 bar, much higher hydrogen storage capacities could be obtained by combining the recycled material with this technology. As a matter of fact, considering the use of higher pressures, which allowed reaching hydrogen uptakes as high as 6.6%, as it was shown previously in **Table 1.1**, and all the other optimizable parameters discussed above, the 7.5% DOE target now seems much more approachable.

CONCLUSIONS

Due to its outstanding properties, hydrogen is really attractive as a replacement for the traditional polluting fossil fuels. However, in order to implement a Hydrogen Economy system based on the use of H_2 as an energy vector and fuel, advanced technologies need to be developed for its storage. Among the different solutions studied, storage in solid materials stands out for being particularly safe and efficient, while also being fit for mobile applications. ACs have especially shown excellent candidates for the adsorption of H_2 due to their high surface area and porosity and low weight. The aim of this work was to evaluate the hydrogen storage potential of a recycled AC material recovered from exhausted wastewater filters, and to optimize it for this purpose by operating on its textural properties and atomic composition.

Gas adsorption analysis was used for the determination of the textural parameters of the various sample, and immediately evidenced the highly microporous nature of the SACs (85-100% micropores). Difficulties in obtaining N_2 isotherms for the Raw samples suggested an impure material, characterized by the presence of non-porous polymeric materials (used as binder in the production of the filters) and adsorbed metal ions. In the case of Raw samples, no real correlation was found between their particle size and their SSA and PSD, due to competition between two factors, namely: (i) expected increase of exposed surface area with smaller particle size; (ii) destruction of part of the internal porous structure with higher comminution degree. After chemical activation with KOH, SSA of the samples increased of a factor of 2.2-2.9, starting from around ~650 m^2/g and reaching surface areas higher than 2000 m^2/g, with such a significant increase due to carbonization of the polymeric materials and catalytic activity of the adsorbed metal ions. Also, a direct proportionality between starting and ending SSA values was observed. The PSD evidenced the widening of pores caused by the reaction with KOH, resulting in higher total pore volume and lower microporosity degree. SEM, CHNS and XPS analyses further confirmed the impure nature of the SAC and demonstrated the effectiveness of the acid wash (performed with acetic acid after activation) in the removal of the ashes produced during reaction with KOH. Thus, AcOH activated samples proved to be purer, despite not clearly higher in SSA

compared to the ones washed with water, due to the ashes mainly covering the external surface area, which makes up for a really small fraction of the surface area of such microporous materials. Additionally, XRD analysis showed the loss in crystallinity caused by the intercalation of K ions in the carbon planes during activation. Doping with urea successfully introduced nitrogen in both the commercial and activated sample, and successive heat treatment resulted in removal of N functionalities and enrichment in graphitic N, with reduced decrease of surface area. The nitrogen content introduced also appeared to be proportional with starting oxygen content in the sample. Hydrogen uptake measurements showed interesting results for the activated samples, with values ranging from 1.62-2.28 wt%. The hydrogen adsorption capacity showed a really strong correlation with, firstly, SSA, and secondly with total pore volume, indicating that bigger pores do not contribute strongly to the adsorption of H_2. What was found instead was that, despite not showing a clear linear dependance with H_2 uptake, the amount of ultra-micropores has a strong influence on the hydrogen storage of the material. This is best exemplified by sample 2-1.4 AcOH, which, despite having lower SSA than sample <0.3 AcOH, showed higher H_2 uptake (2.28 wt% vs 2.00 wt%), due to its much higher ultra-micropore volume (0.30 cm^3/g vs 0.20 cm^3/g). Moreover, the AcOH samples appeared to have slightly higher uptakes compared to their W counterparts, presumably due to their purity. Doping the samples also resulted in a significant increase of the performance of the material, of 11% for the commercial sample, doped with 0.32% N content and 17% for the <0.3 AcOH sample, doped with 0.41% N content. This different increase can be correlated to both higher nitrogen content introduced and smaller loss of surface area observed in the case of the second sample.

The results obtained look really promising, and a good starting point for further optimization of this materials by varying different parameters, such as SAC:KOH ratio, structural parameters, and doping amount. Additionally, measurements at higher pressures could be performed in order to achieve much higher H_2 uptake values, which would be way closer to the UFF DOE target. In conclusion, the recycling of spent activated carbon from wastewater filters resulted in a low-cost and sustainable material that shows potential for the storage of hydrogen, and, with further study, could be functional for the development of future hydrogen-based vehicles, such as automobiles [113], trucks [114] and planes [115].

BIBLIOGRAPHY

[1] 'https://www.planete-energies.com/en/media/infographic/global-energy-mix-1990-2035'.

[2] 'United Nations Environment Programme, & International Resource Panel (2011). Decoupling Natural Resource Use and Environmental Impacts from Economic Growth. https://wedocs.unep.org/20.500.11822/9816.'

[3] J. Scheffran, M. Felkers, and R. Froese, 'Economic Growth and the Global Energy Demand', in *Green Energy to Sustainability*, Wiley, 2020, pp. 1–44. doi: 10.1002/9781119152057.ch1.

[4] G. Giannakoudis, A. I. Papadopoulos, P. Seferlis, and S. Voutetakis, 'Optimum design and operation under uncertainty of power systems using renewable energy sources and hydrogen storage', *Int J Hydrogen Energy*, vol. 35, no. 3, pp. 872–891, Feb. 2010, doi: 10.1016/j.ijhydene.2009.11.044.

[5] J. Ren, N. M. Musyoka, H. W. Langmi, M. Mathe, and S. Liao, 'Current research trends and perspectives on materials-based hydrogen storage solutions: A critical review', *Int J Hydrogen Energy*, vol. 42, no. 1, pp. 289–311, Jan. 2017, doi: 10.1016/j.ijhydene.2016.11.195.

[6] J. O. Abe, A. P. I. Popoola, E. Ajenifuja, and O. M. Popoola, 'Hydrogen energy, economy and storage: Review and recommendation', *Int J Hydrogen Energy*, vol. 44, no. 29, pp. 15072–15086, Jun. 2019, doi: 10.1016/j.ijhydene.2019.04.068.

[7] 'https://www.gknhydrogen.com/microgrid/'.

[8] M. Mohan, V. K. Sharma, E. A. Kumar, and V. Gayathri, 'Hydrogen storage in carbon materials—A review', *Energy Storage*, vol. 1, no. 2, Apr. 2019, doi: 10.1002/est2.35.

[9] '"2022 Fit for 55" https://www.consilium.europa.eu/en/policies/green-deal/fit-for-55-the-eu-plan-for-a-green-transition/European Council, Council of the European Union. 2022.'

[10] 'IRENA (2018), Global Energy Transformation: A roadmap to 2050, International Renewable Energy Agency, Abu Dhabi.'

[11] P. Prachi R., W. Mahesh M., and G. Aneesh C., 'A Review on Solid State Hydrogen Storage Material', *Advances in Energy and Power*, vol. 4, no. 2, pp. 11–22, Jun. 2016, doi: 10.13189/aep.2016.040202.

[12] J. Andersson and S. Grönkvist, 'Large-scale storage of hydrogen', *Int J Hydrogen Energy*, vol. 44, no. 23, pp. 11901–11919, May 2019, doi: 10.1016/j.ijhydene.2019.03.063.

[13] 'Office of Energy Efficiency & Renewable Energy: Hydrogen Storage. Available online: https://www.energy.gov/eere/fuelcells/hydrogen-storage (accessed on 25 November 2022).'

[14] P. Ramirez-Vidal, G. Sdanghi, A. Celzard, and V. Fierro, 'High hydrogen release by cryo-adsorption and compression on porous materials', *Int J Hydrogen Energy*, vol. 47, no. 14, pp. 8892–8915, Feb. 2022, doi: 10.1016/j.ijhydene.2021.12.235.

[15] M. Flekiewicz and G. Kubica, 'Hydrogen Onboard Storage Technologies for Vehicles', in *Diesel Engines - Current Challenges and Future Perspectives [Working Title]*, IntechOpen, 2023. doi: 10.5772/intechopen.1003040.

[16] 'https://www.energy.gov/eere/fuelcells/hydrogen-storage'.

[17] 'https://www.energy.gov/eere/fuelcells/doe-technical-targets-onboard-hydrogen-storage-light-duty-vehicles'.

[18] M. Rzepka, P. Lamp, and M. A. de la Casa-Lillo, 'Physisorption of Hydrogen on Microporous Carbon and Carbon Nanotubes', *J Phys Chem B*, vol. 102, no. 52, pp. 10894–10898, Dec. 1998, doi: 10.1021/jp9829602.

[19] R. Ströbel, J. Garche, P. T. Moseley, L. Jörissen, and G. Wolf, 'Hydrogen storage by carbon materials', *J Power Sources*, vol. 159, no. 2, pp. 781–801, Sep. 2006, doi: 10.1016/j.jpowsour.2006.03.047.

[20] M. Lewoyehu, 'Comprehensive review on synthesis and application of activated carbon from agricultural residues for the remediation of venomous pollutants in wastewater', *J Anal Appl Pyrolysis*, vol. 159, p. 105279, Oct. 2021, doi: 10.1016/j.jaap.2021.105279.

[21] W. Zhao, V. Fierro, N. Fernández-Huerta, M. T. Izquierdo, and A. Celzard, 'Impact of synthesis conditions of KOH activated carbons on their hydrogen storage capacities', *Int J Hydrogen Energy*, vol. 37, no. 19, pp. 14278–14284, Oct. 2012, doi: 10.1016/j.ijhydene.2012.06.110.

[22] S. Schaefer *et al.*, 'Oxygen-promoted hydrogen adsorption on activated and hybrid carbon materials', *Int J Hydrogen Energy*, vol. 45, no. 55, pp. 30767–30782, Nov. 2020, doi: 10.1016/j.ijhydene.2020.08.114.

[23] S.-Y. Lee and S.-J. Park, 'Effect of platinum doping of activated carbon on hydrogen storage behaviors of metal-organic frameworks-5', *Int J Hydrogen Energy*, vol. 36, no. 14, pp. 8381–8387, Jul. 2011, doi: 10.1016/j.ijhydene.2011.03.038.

[24] W. Zhao *et al.*, 'Activated carbons doped with Pd nanoparticles for hydrogen storage', *Int J Hydrogen Energy*, vol. 37, no. 6, pp. 5072–5080, Mar. 2012, doi: 10.1016/j.ijhydene.2011.12.058.

[25] W. XU *et al.*, 'Investigation of hydrogen storage capacity of various carbon materials', *Int J Hydrogen Energy*, vol. 32, no. 13, pp. 2504–2512, Sep. 2007, doi: 10.1016/j.ijhydene.2006.11.012.

[26] Y. Wang *et al.*, 'Surface functionalization-enhanced spillover effect on hydrogen storage of Ni–B nanoalloy-doped activated carbon', *Int J Hydrogen Energy*, vol. 36, no. 21, pp. 13663–13668, Oct. 2011, doi: 10.1016/j.ijhydene.2011.08.049.

[27] R. Ströbel *et al.*, 'Hydrogen adsorption on carbon materials', *J Power Sources*, vol. 84, no. 2, pp. 221–224, Dec. 1999, doi: 10.1016/S0378-7753(99)00320-1.

[28] M. Hirscher and B. Panella, 'Nanostructures with high surface area for hydrogen storage', *J Alloys Compd*, vol. 404–406, pp. 399–401, Dec. 2005, doi: 10.1016/j.jallcom.2004.11.109.

[29] J. Jjagwe, P. W. Olupot, E. Menya, and H. M. Kalibbala, 'Synthesis and Application of Granular Activated Carbon from Biomass Waste Materials for Water Treatment:

A Review', *Journal of Bioresources and Bioproducts*, vol. 6, no. 4, pp. 292–322, Nov. 2021, doi: 10.1016/j.jobab.2021.03.003.

[30] 'https://sgc-wwd.s3.amazonaws.com/s3fs-public/WQP%20Activated%20Carbon%201_00.pdf'.

[31] D. A. Gkika, A. C. Mitropoulos, and G. Z. Kyzas, 'Why reuse spent adsorbents? The latest challenges and limitations', *Science of The Total Environment*, vol. 822, p. 153612, May 2022, doi: 10.1016/j.scitotenv.2022.153612.

[32] J. Quílez-Bermejo *et al.*, 'Easy enrichment of graphitic nitrogen to prepare highly catalytic carbons for oxygen reduction reaction', *Carbon N Y*, vol. 196, pp. 708–717, Aug. 2022, doi: 10.1016/j.carbon.2022.05.032.

[33] K. S. W. Sing, 'Reporting physisorption data for gas/solid systems with special reference to the determination of surface area and porosity (Recommendations 1984)', *Pure and Applied Chemistry*, vol. 57, no. 4, pp. 603–619, Jan. 1985, doi: 10.1351/pac198557040603.

[34] M. Thommes *et al.*, 'Physisorption of gases, with special reference to the evaluation of surface area and pore size distribution (IUPAC Technical Report)', *Pure and Applied Chemistry*, vol. 87, no. 9–10, pp. 1051–1069, Oct. 2015, doi: 10.1515/pac-2014-1117.

[35] B. P. Bering, M. M. Dubinin, and V. V. Serpinsky, 'Theory of volume filling for vapor adsorption', *J Colloid Interface Sci*, vol. 21, no. 4, pp. 378–393, Apr. 1966, doi: 10.1016/0095-8522(66)90004-3.

[36] M. Thommes and K. A. Cychosz, 'Physical adsorption characterization of nanoporous materials: progress and challenges', *Adsorption*, vol. 20, no. 2–3, pp. 233–250, Feb. 2014, doi: 10.1007/s10450-014-9606-z.

[37] P. A. Monson, 'Understanding adsorption/desorption hysteresis for fluids in mesoporous materials using simple molecular models and classical density functional theory', *Microporous and Mesoporous Materials*, vol. 160, pp. 47–66, Sep. 2012, doi: 10.1016/j.micromeso.2012.04.043.

[38] 'https://www.micromeritics.com/Repository/Files/Pharma_Excipents_Kenvin_Presentation.pdf'.

[39] S. Brunauer, L. S. Deming, W. E. Deming, and E. Teller, 'On a Theory of the van der Waals Adsorption of Gases', *J Am Chem Soc*, vol. 62, no. 7, pp. 1723–1732, Jul. 1940, doi: 10.1021/ja01864a025.

[40] H. M. Cassel, 'Condensation Coefficient and Adsorption', *J Chem Phys*, vol. 17, no. 10, pp. 1000–1001, Oct. 1949, doi: 10.1063/1.1747063.

[41] A. V. Neimark, P. I. Ravikovitch, and A. Vishnyakov, 'Adsorption hysteresis in nanopores', *Phys Rev E*, vol. 62, no. 2, pp. R1493–R1496, Aug. 2000, doi: 10.1103/PhysRevE.62.R1493.

[42] J. Landers, G. Yu. Gor, and A. V. Neimark, 'Density functional theory methods for characterization of porous materials', *Colloids Surf A Physicochem Eng Asp*, vol. 437, pp. 3–32, Nov. 2013, doi: 10.1016/j.colsurfa.2013.01.007.

[43] S. Brunauer, P. H. Emmett, and E. Teller, 'Adsorption of Gases in Multimolecular Layers', *J Am Chem Soc*, vol. 60, no. 2, pp. 309–319, Feb. 1938, doi: 10.1021/ja01269a023.

[44] I. Langmuir, 'THE ADSORPTION OF GASES ON PLANE SURFACES OF GLASS, MICA AND PLATINUM.', *J Am Chem Soc*, vol. 40, no. 9, pp. 1361–1403, Sep. 1918, doi: 10.1021/ja02242a004.

[45] S. Lowell, J. E. Shields, M. A. Thomas, and M. Thommes, *Characterization of Porous Solids and Powders: Surface Area, Pore Size and Density*, vol. 16. Dordrecht: Springer Netherlands, 2004. doi: 10.1007/978-1-4020-2303-3.

[46] J. Rouquerol, P. Llewellyn, and F. Rouquerol, 'Is the bet equation applicable to microporous adsorbents?', 2007, pp. 49–56. doi: 10.1016/S0167-2991(07)80008-5.

[47] J. Landers, G. Yu. Gor, and A. V. Neimark, 'Density functional theory methods for characterization of porous materials', *Colloids Surf A Physicochem Eng Asp*, vol. 437, pp. 3–32, Nov. 2013, doi: 10.1016/j.colsurfa.2013.01.007.

[48] J. Jagiello and J. P. Olivier, 'A Simple Two-Dimensional NLDFT Model of Gas Adsorption in Finite Carbon Pores. Application to Pore Structure Analysis', *The Journal of Physical Chemistry C*, vol. 113, no. 45, pp. 19382–19385, Nov. 2009, doi: 10.1021/jp9082147.

[49] J. Wang and S. Kaskel, ‘KOH activation of carbon-based materials for energy storage’, *J Mater Chem*, vol. 22, no. 45, p. 23710, 2012, doi: 10.1039/c2jm34066f.

[50] T. Otowa, R. Tanibata, and M. Itoh, ‘Production and adsorption characteristics of MAXSORB: High-surface-area active carbon’, *Gas Separation & Purification*, vol. 7, no. 4, pp. 241–245, Jan. 1993, doi: 10.1016/0950-4214(93)80024-Q.

[51] D. Lozano-Castelló, J. M. Calo, D. Cazorla-Amorós, and A. Linares-Solano, ‘Carbon activation with KOH as explored by temperature programmed techniques, and the effects of hydrogen’, *Carbon N Y*, vol. 45, no. 13, pp. 2529–2536, Nov. 2007, doi: 10.1016/j.carbon.2007.08.021.

[52] E. Raymundo-Piñero, P. Azaïs, T. Cacciaguerra, D. Cazorla-Amorós, A. Linares-Solano, and F. Béguin, ‘KOH and NaOH activation mechanisms of multiwalled carbon nanotubes with different structural organisation’, *Carbon N Y*, vol. 43, no. 4, pp. 786–795, 2005, doi: 10.1016/j.carbon.2004.11.005.

[53] J. E. Park, G. B. Lee, B. U. Hong, and S. Y. Hwang, ‘Regeneration of Activated Carbons Spent by Waste Water Treatment Using KOH Chemical Activation’, *Applied Sciences*, vol. 9, no. 23, p. 5132, Nov. 2019, doi: 10.3390/app9235132.

[54] E. Möller *et al.*, ‘Peat-Derived ZnCl2-Activated Ultramicroporous Carbon Materials for Hydrogen Adsorption’, *Nanomaterials*, vol. 13, no. 21, p. 2883, Oct. 2023, doi: 10.3390/nano13212883.

[55] ‘https://www.micromeritics.com/asap-2020-plus/?utm_term=&utm_campaign=MIC+Corporate+Campaign&utm_source=adwords&utm_medium=ppc&hsa_acc=2339074468&hsa_cam=14939750590&hsa_grp=129885697865&hsa_ad=566070572596&hsa_src=g&hsa_tgt=aud-1534979504286:dsa-1492852222268&hsa_kw=&hsa_mt=&hsa_net=adwords&hsa_ver=3&gad_source=1&gclid=CjwKCAiAvJarBhA1EiwAGgZl0OM2PRTtN5azFdNeEEHWavK9OCzBfgxCICUtoVwLPV1OH5D01bh5hoC8xcQAvD_BwE’.

[56] ‘https://www.micromeritics.com/Repository/Files/ASAP_2020_Operator_Manual_Rev_-_Feb_2019.pdf’.

[57] Jelinek L and sz. Kovats E, ‘True surface areas from nitrogen adsorption experiments’, *Langmuir*, vol. 10, no. 11, pp. 4225–4231, 1994.

[58] S. Mopoung, P. Moonsri, W. Palas, and S. Khumpai, ‘Characterization and Properties of Activated Carbon Prepared from Tamarind Seeds by KOH Activation for Fe(III) Adsorption from Aqueous Solution’, *The Scientific World Journal*, vol. 2015, pp. 1–9, 2015, doi: 10.1155/2015/415961.

[59] D. Cazorla-Amorós, J. Alcañiz-Monge, and A. Linares-Solano, ‘Characterization of Activated Carbon Fibers by CO_2 Adsorption’, *Langmuir*, vol. 12, no. 11, pp. 2820–2824, Jan. 1996, doi: 10.1021/la960022s.

[60] A. Vishnyakov, P. I. Ravikovitch, and A. V. Neimark, ‘Molecular Level Models for CO_2 Sorption in Nanopores’, *Langmuir*, vol. 15, no. 25, pp. 8736–8742, Dec. 1999, doi: 10.1021/la990726c.

[61] P. I. Ravikovitch, A. Vishnyakov, R. Russo, and A. V. Neimark, ‘Unified Approach to Pore Size Characterization of Microporous Carbonaceous Materials from N_2, Ar, and CO_2 Adsorption Isotherms’, *Langmuir*, vol. 16, no. 5, pp. 2311–2320, Mar. 2000, doi: 10.1021/la991011c.

[62] H. Kurig, M. Russina, I. Tallo, M. Siebenbürger, T. Romann, and E. Lust, ‘The suitability of infinite slit-shaped pore model to describe the pores in highly porous carbon materials’, *Carbon N Y*, vol. 100, pp. 617–624, Apr. 2016, doi: 10.1016/j.carbon.2016.01.061.

[63] A. Einstein, ‘Über einen die Erzeugung und Verwandlung des Lichtes betreffenden heuristischen Gesichtspunkt’, *Ann Phys*, vol. 322, no. 6, pp. 132–148, Jan. 1905, doi: 10.1002/andp.19053220607.

[64] Moulder J F, *Handbook of X-ray Photoelectron Spectroscopy: A Reference Book of Standard Spectra for Identification and Interpretation of XPS Data*. 1992.

[65] ‘https://epm.univie.ac.at/research/low-dimensional-quantum-solids/methods/’.

[66] ‘https://www.cinelsrl.it/ad-series/’.

[67] ‘https://www.micromeritics.com/Repository/Files/ap136.pdf’.

[68] M. E. Quadros and L. C. Marr, ‘Environmental and Human Health Risks of Aerosolized Silver Nanoparticles’, *J Air Waste Manage Assoc*, vol. 60, no. 7, pp. 770–781, Jul. 2010, doi: 10.3155/1047-3289.60.7.770.

[69] N. Purhanudin, F. Mohd Idris, and N. Pallan, ‘Effects of Nanometer Particle Size on the Properties of Activated Carbon from Terminalia Catappa Fruits Waste’. Nov. 2022. doi: 10.21203/rs.3.rs-2239940/v1.

[70] S. M. Mak, B. T. Tey, K. Y. Cheah, W. L. Siew, and K. K. Tan, ‘Porosity characteristics and pore developments of various particle sizes palm kernel shells activated carbon (PKSAC) and its potential applications’, *Adsorption*, vol. 15, no. 5–6, pp. 507–519, Dec. 2009, doi: 10.1007/s10450-009-9201-x.

[71] P. M. Satya Sai, J. Ahmed, and K. Krishnaiah, ‘Production of Activated Carbon from Coconut Shell Char in a Fluidized Bed Reactor’, *Ind Eng Chem Res*, vol. 36, no. 9, pp. 3625–3630, Sep. 1997, doi: 10.1021/ie970190v.

[72] Q. Cao, K. Xie, Y. Lv, and W. Bao, ‘Process effects on activated carbon with large specific surface area from corn cob’, *Bioresour Technol*, vol. 97, no. 1, pp. 110–115, Jan. 2006, doi: 10.1016/j.biortech.2005.02.026.

[73] J. Andas, M. L. A. Rahman, and M. S. M. Yahya, ‘Preparation and Characterization of Activated Carbon from Palm Kernel Shell’, *IOP Conf Ser Mater Sci Eng*, vol. 226, p. 012156, Aug. 2017, doi: 10.1088/1757-899X/226/1/012156.

[74] J. Choma, M. Marszewski, L. Osuchowski, J. Jagiello, A. Dziura, and M. Jaroniec, ‘Adsorption Properties of Activated Carbons Prepared from Waste CDs and DVDs’, *ACS Sustain Chem Eng*, vol. 3, no. 4, pp. 733–742, Apr. 2015, doi: 10.1021/acssuschemeng.5b00036.

[75] M. S. Felice and M. B. Freilich, ‘Chemical kinetics: The effect of surface area on reaction rate’, *J Chem Educ*, vol. 55, no. 1, p. 34, Jan. 1978, doi: 10.1021/ed055p34.2.

[76] D. An, Y. Guo, B. Zou, Y. Zhu, and Z. Wang, ‘A study on the consecutive preparation of silica powders and active carbon from rice husk ash’, *Biomass Bioenergy*, vol. 35, no. 3, pp. 1227–1234, Mar. 2011, doi: 10.1016/j.biombioe.2010.12.014.

[77] L. N. Sklivaniotis, P. Economou, H. K. Karapanagioti, and I. D. Manariotis, ‘Chlorine Removal from Water by Biochar Derived from Various Food Waste Natural Materials’, *Environmental Processes*, vol. 10, no. 1, p. 4, Mar. 2023, doi: 10.1007/s40710-022-00617-4.

[78] Z. Yue and J. Economy, ‘Carbonization and activation for production of activated carbon fibers’, in *Activated Carbon Fiber and Textiles*, Elsevier, 2017, pp. 61–139. doi: 10.1016/B978-0-08-100660-3.00004-3.

[79] D. Lennon, D. T. Lundie, S. D. Jackson, G. J. Kelly, and S. F. Parker, ‘Characterization of Activated Carbon Using X-ray Photoelectron Spectroscopy and Inelastic Neutron Scattering Spectroscopy’, *Langmuir*, vol. 18, no. 12, pp. 4667–4673, Jun. 2002, doi: 10.1021/la011324j.

[80] N. K. Kalagatur *et al.*, ‘Application of Activated Carbon Derived from Seed Shells of Jatropha curcas for Decontamination of Zearalenone Mycotoxin’, *Front Pharmacol*, vol. 8, Oct. 2017, doi: 10.3389/fphar.2017.00760.

[81] S.-M. Lee, S.-H. Lee, and J.-S. Roh, ‘Analysis of Activation Process of Carbon Black Based on Structural Parameters Obtained by XRD Analysis’, *Crystals (Basel)*, vol. 11, no. 2, p. 153, Feb. 2021, doi: 10.3390/cryst11020153.

[82] F. Schossberger, ‘Amorphous Solids, Small Particles and Thin Surface Films’, *Advances in X-ray Analysis*, vol. 1, pp. 73–99, Mar. 1957, doi: 10.1154/S0376030800000094.

[83] N. Bader and A. Ouederni, ‘Optimization of biomass-based carbon materials for hydrogen storage’, *J Energy Storage*, vol. 5, pp. 77–84, Feb. 2016, doi: 10.1016/j.est.2015.12.009.

[84] C. Saka, ‘BET, TG–DTG, FT-IR, SEM, iodine number analysis and preparation of activated carbon from acorn shell by chemical activation with ZnCl2’, *J Anal Appl Pyrolysis*, vol. 95, pp. 21–24, May 2012, doi: 10.1016/j.jaap.2011.12.020.

[85] L. Shi *et al.*, ‘Higher Yield Urea-Derived Polymeric Graphitic Carbon Nitride with Mesoporous Structure and Superior Visible-Light-Responsive Activity’, *ACS Sustain Chem Eng*, vol. 3, no. 12, pp. 3412–3419, Dec. 2015, doi: 10.1021/acssuschemeng.5b01139.

[86] S. Biniak, G. Szymański, J. Siedlewski, and A. Świątkowski, 'The characterization of activated carbons with oxygen and nitrogen surface groups', *Carbon N Y*, vol. 35, no. 12, pp. 1799–1810, 1997, doi: 10.1016/S0008-6223(97)00096-1.

[87] H. P. Boehm, 'Some aspects of the surface chemistry of carbon blacks and other carbons', *Carbon N Y*, vol. 32, no. 5, pp. 759–769, 1994, doi: 10.1016/0008-6223(94)90031-0.

[88] L. A. Romero-Cano *et al.*, 'Surface functionalization to abate the irreversible capacity of hard carbons derived from grapefruit peels for sodium-ion batteries', *Electrochim Acta*, vol. 326, p. 134973, Dec. 2019, doi: 10.1016/j.electacta.2019.134973.

[89] J. Quílez-Bermejo, E. Morallón, and D. Cazorla-Amorós, 'Polyaniline-Derived N-Doped Ordered Mesoporous Carbon Thin Films: Efficient Catalysts towards Oxygen Reduction Reaction', *Polymers (Basel)*, vol. 12, no. 10, p. 2382, Oct. 2020, doi: 10.3390/polym12102382.

[90] J. R. Pels, F. Kapteijn, J. A. Moulijn, Q. Zhu, and K. M. Thomas, 'Evolution of nitrogen functionalities in carbonaceous materials during pyrolysis', *Carbon N Y*, vol. 33, no. 11, pp. 1641–1653, 1995, doi: 10.1016/0008-6223(95)00154-6.

[91] W. Yang *et al.*, 'Effect of thermal program on structure–activity relationship of g-C3N4 prepared by urea pyrolysis and its application for controllable production of g-C3N4', *J Solid State Chem*, vol. 304, p. 122545, Dec. 2021, doi: 10.1016/j.jssc.2021.122545.

[92] R. Pietrzak, H. Wachowska, and P. Nowicki, 'Preparation of Nitrogen-Enriched Activated Carbons from Brown Coal', *Energy & Fuels*, vol. 20, no. 3, pp. 1275–1280, May 2006, doi: 10.1021/ef0504164.

[93] K. Y. Kang, B. I. Lee, and J. S. Lee, 'Hydrogen adsorption on nitrogen-doped carbon xerogels', *Carbon N Y*, vol. 47, no. 4, pp. 1171–1180, Apr. 2009, doi: 10.1016/j.carbon.2009.01.001.

[94] K. M. Thomas, 'Hydrogen adsorption and storage on porous materials☆', *Catal Today*, vol. 120, no. 3–4, pp. 389–398, Feb. 2007, doi: 10.1016/j.cattod.2006.09.015.

[95] B. Panella, M. Hirscher, and S. Roth, ‘Hydrogen adsorption in different carbon nanostructures’, *Carbon N Y*, vol. 43, no. 10, pp. 2209–2214, Aug. 2005, doi: 10.1016/j.carbon.2005.03.037.

[96] N. Texier-Mandoki, J. Dentzer, T. Piquero, S. Saadallah, P. David, and C. Vix-Guterl, ‘Hydrogen storage in activated carbon materials: Role of the nanoporous texture’, *Carbon N Y*, vol. 42, no. 12–13, pp. 2744–2747, 2004, doi: 10.1016/j.carbon.2004.05.018.

[97] Y. Xia, G. S. Walker, D. M. Grant, and R. Mokaya, ‘Hydrogen Storage in High Surface Area Carbons: Experimental Demonstration of the Effects of Nitrogen Doping’, *J Am Chem Soc*, vol. 131, no. 45, pp. 16493–16499, Nov. 2009, doi: 10.1021/ja9054838.

[98] G. Sethia and A. Sayari, ‘Activated carbon with optimum pore size distribution for hydrogen storage’, *Carbon N Y*, vol. 99, pp. 289–294, Apr. 2016, doi: 10.1016/j.carbon.2015.12.032.

[99] R. Härmas *et al.*, ‘Transport properties of H2 confined in carbide-derived carbons with different pore shapes and sizes’, *Carbon N Y*, vol. 155, pp. 122–128, Dec. 2019, doi: 10.1016/j.carbon.2019.08.041.

[100] M. Sevilla, A. B. Fuertes, and R. Mokaya, ‘Preparation and hydrogen storage capacity of highly porous activated carbon materials derived from polythiophene’, *Int J Hydrogen Energy*, vol. 36, no. 24, pp. 15658–15663, Dec. 2011, doi: 10.1016/j.ijhydene.2011.09.032.

[101] M. A. de la Casa-Lillo, F. Lamari-Darkrim, D. Cazorla-Amorós, and A. Linares-Solano, ‘Hydrogen Storage in Activated Carbons and Activated Carbon Fibers’, *J Phys Chem B*, vol. 106, no. 42, pp. 10930–10934, Oct. 2002, doi: 10.1021/jp014543m.

[102] L. Wang and R. T. Yang, ‘Hydrogen Storage Properties of N-Doped Microporous Carbon’, *The Journal of Physical Chemistry C*, vol. 113, no. 52, pp. 21883–21888, Dec. 2009, doi: 10.1021/jp908156v.

[103] L. Wang, F. H. Yang, and R. T. Yang, 'Hydrogen storage properties of B- and N-doped microporous carbon', *AIChE Journal*, vol. 55, no. 7, pp. 1823–1833, Jul. 2009, doi: 10.1002/aic.11851.

[104] Z. H. Zhu, H. Hatori, S. B. Wang, and G. Q. Lu, 'Insights into Hydrogen Atom Adsorption on and the Electrochemical Properties of Nitrogen-Substituted Carbon Materials', *J Phys Chem B*, vol. 109, no. 35, pp. 16744–16749, Sep. 2005, doi: 10.1021/jp051787o.

[105] M. M. de Castro, M. Martínez-Escandell, M. Molina-Sabio, and F. Rodríguez-Reinoso, 'Hydrogen adsorption on KOH activated carbons from mesophase pitch containing Si, B, Ti or Fe', *Carbon N Y*, vol. 48, no. 3, pp. 636–644, Mar. 2010, doi: 10.1016/j.carbon.2009.10.005.

[106] C. Zhang *et al.*, 'Microstructure regulation of super activated carbon from biomass source corncob with enhanced hydrogen uptake', *Int J Hydrogen Energy*, vol. 38, no. 22, pp. 9243–9250, Jul. 2013, doi: 10.1016/j.ijhydene.2013.04.163.

[107] I. Wróbel-Iwaniec, N. Díez, and G. Gryglewicz, 'Chitosan-based highly activated carbons for hydrogen storage', *Int J Hydrogen Energy*, vol. 40, no. 17, pp. 5788–5796, May 2015, doi: 10.1016/j.ijhydene.2015.03.034.

[108] M. Sevilla, A. B. Fuertes, and R. Mokaya, 'High density hydrogen storage in super-activated carbons from hydrothermally carbonized renewable organic materials', *Energy Environ Sci*, vol. 4, no. 4, p. 1400, 2011, doi: 10.1039/c0ee00347f.

[109] X. Liu, C. Zhang, Z. Geng, and M. Cai, 'High-pressure hydrogen storage and optimizing fabrication of corncob-derived activated carbon', *Microporous and Mesoporous Materials*, vol. 194, pp. 60–65, Aug. 2014, doi: 10.1016/j.micromeso.2014.04.005.

[110] R. Yang, G. Liu, M. Li, J. Zhang, and X. Hao, 'Preparation and N2, CO2 and H2 adsorption of super activated carbon derived from biomass source hemp (Cannabis sativa L.) stem', *Microporous and Mesoporous Materials*, vol. 158, pp. 108–116, Aug. 2012, doi: 10.1016/j.micromeso.2012.03.004.

[111] W. Zhao, V. Fierro, N. Fernández-Huerta, M. T. Izquierdo, and A. Celzard, 'Hydrogen uptake of high surface area-activated carbons doped with nitrogen', *Int J*

Hydrogen Energy, vol. 38, no. 25, pp. 10453–10460, Aug. 2013, doi: 10.1016/j.ijhydene.2013.06.048.

[112] G. Sdanghi, R. L. S. Canevesi, A. Celzard, M. Thommes, and V. Fierro, 'Characterization of Carbon Materials for Hydrogen Storage and Compression', *C — Journal of Carbon Research*, vol. 6, no. 3, p. 46, Jul. 2020, doi: 10.3390/c6030046.

[113] D. Mori *et al.*, 'Hydrogen Storage Materials for Fuel Cell Vehicles High-pressure MH System', *Journal of the Japan Institute of Metals*, vol. 69, no. 3, pp. 308–311, 2005, doi: 10.2320/jinstmet.69.308.

[114] R. Parkes, '"Record run" | Daimler's Mercedes-Benz green hydrogen truck drives over 1,000km on a single tank', *Hydrogeninsight*, 2023.

[115] 'https://www.airbus.com/en/innovation/low-carbon-aviation/hydrogen'.

APPENDIX

Appendix A

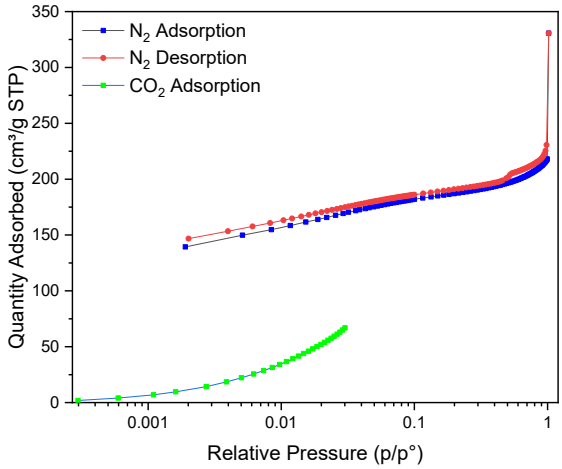

Figure A.1: N_2 adsorption and desorption isotherm and CO_2 adsorption isotherm for sample 2.83-2 Raw.

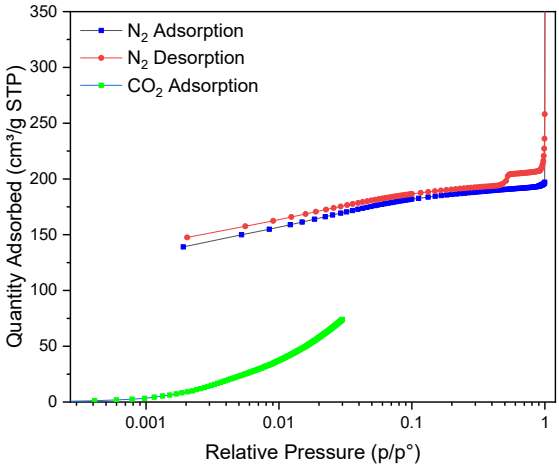

Figure A.2: N_2 adsorption and desorption isotherm *and CO_2 adsorption isotherm* for sample 2-1.4 Raw.

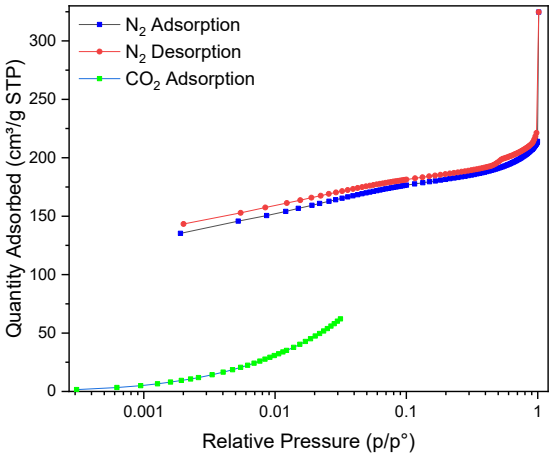

Figure A.3: N_2 adsorption and desorption isotherm *and CO_2 adsorption isotherm* for sample 1.4-1 Raw.

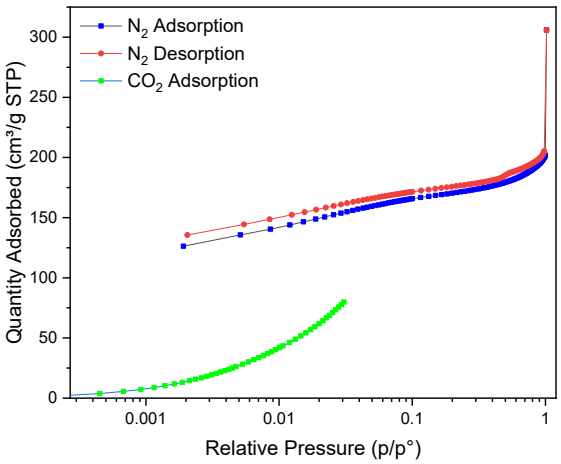

Figure A.4: N_2 adsorption and desorption isotherm *and CO_2 adsorption isotherm* for sample 1-0.8 Raw.

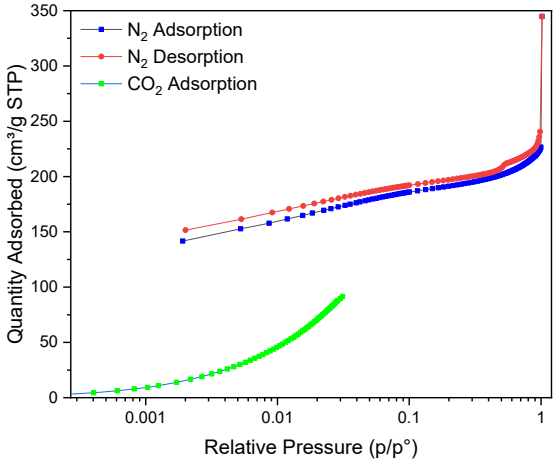

Figure A.5: N_2 adsorption and desorption isotherm *and CO_2 adsorption isotherm* for sample 0.8-0.6 Raw.

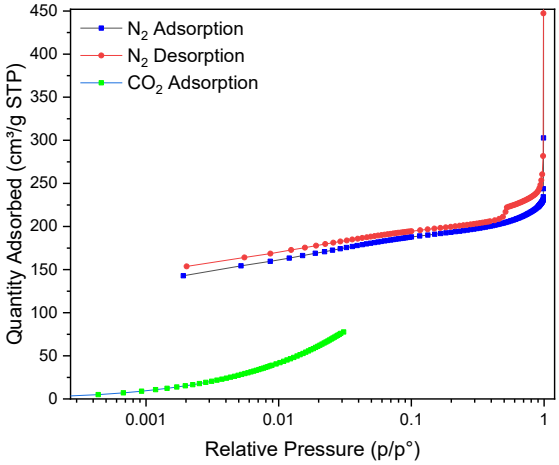

Figure A.6: N_2 adsorption and desorption isotherm *and CO_2 adsorption isotherm* for sample 0.6-0.5 Raw.

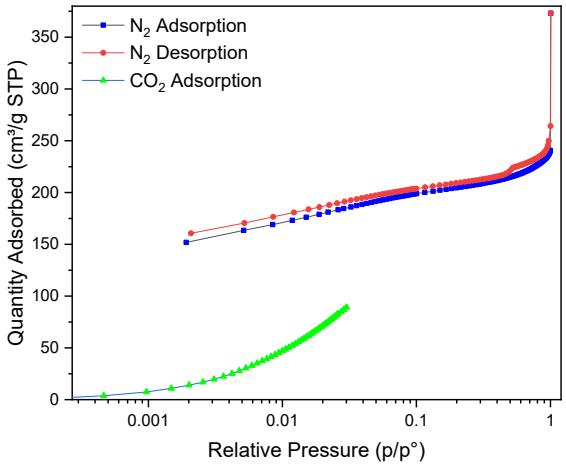

Figure A.7: N_2 adsorption and desorption isotherm *and CO_2 adsorption isotherm* for sample 0.5-0.4 Raw.

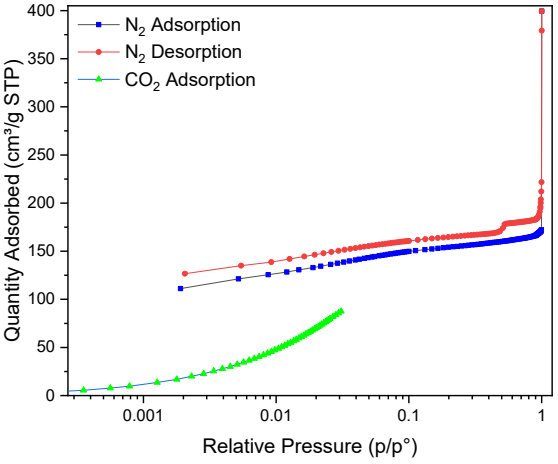

Figure A.8: N_2 adsorption and desorption isotherm *and CO_2 adsorption isotherm* for sample 0.4-0.3 Raw.

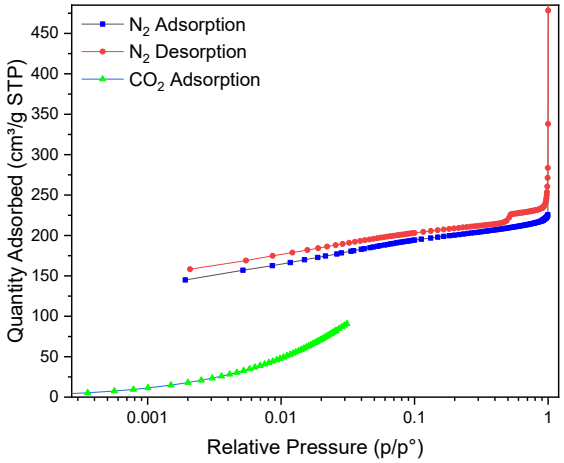

Figure A.9: N_2 adsorption and desorption isotherm *and CO_2 adsorption isotherm* for sample <0.3 Raw.

Appendix B

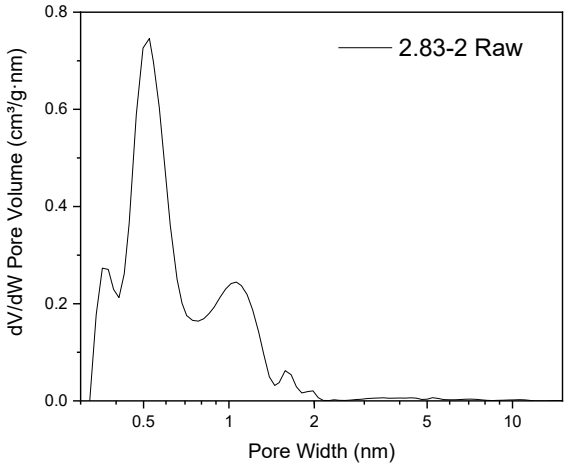

Figure B.1: Differential pore size distribution for sample 2.83-2 Raw.

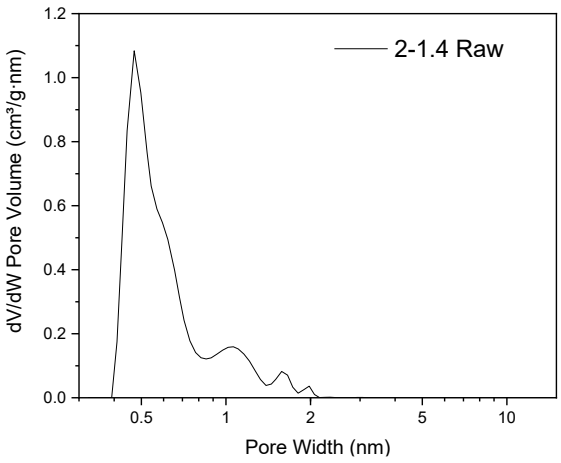

Figure B.2: Differential pore size distribution for sample 2-1.4 Raw.

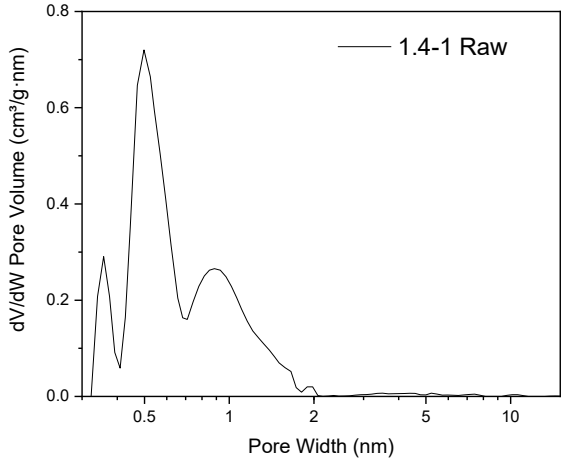

Figure B.3: Differential pore size distribution for sample 1.4-1 Raw.

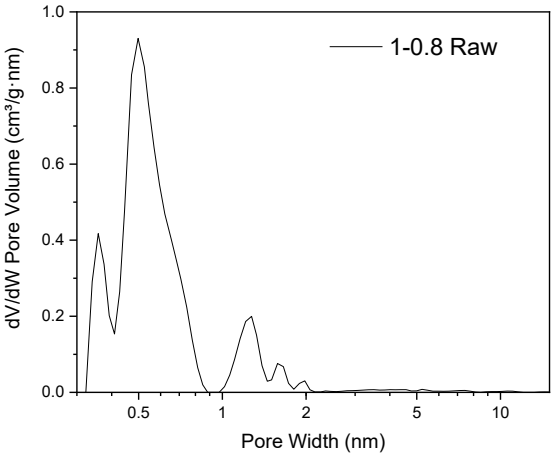

Figure B.4: Differential pore size distribution for sample 1-0.8 Raw.

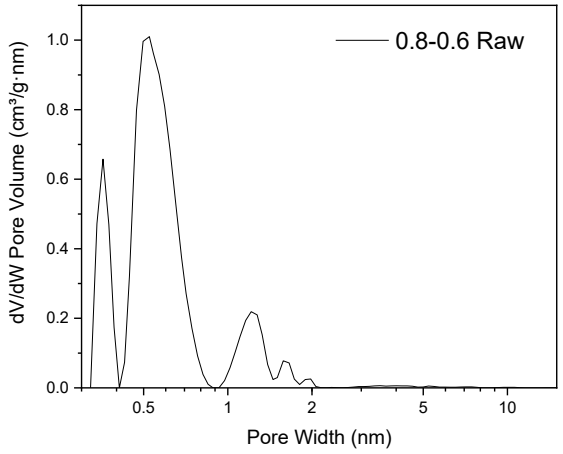

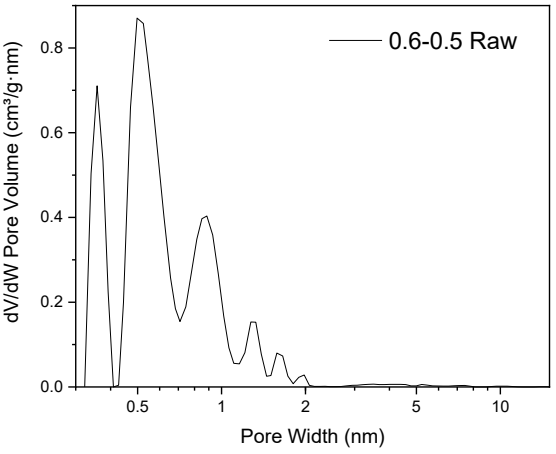

Figure B.5: Differential pore size distribution for sample 0.8-0.6 Raw.

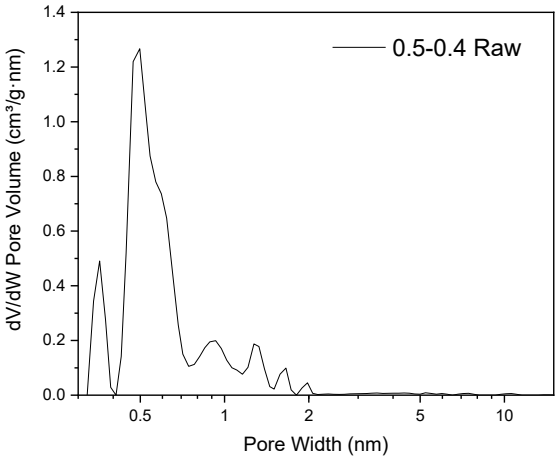

Figure B.6: Differential pore size distribution for sample 0.6-0.5 Raw.

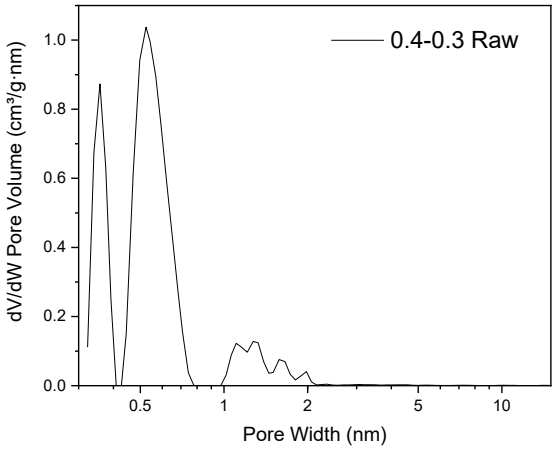

Figure B.7: Differential pore size distribution for sample 0.5-0.4 Raw.

Figure B.8: Differential pore size distribution for sample 0.4-0.3 Raw.

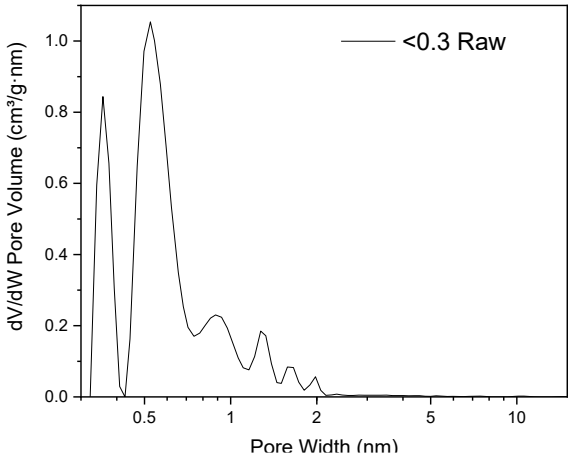

Figure B.9: Differential pore size distribution for sample <0.3 Raw.

Appendix C

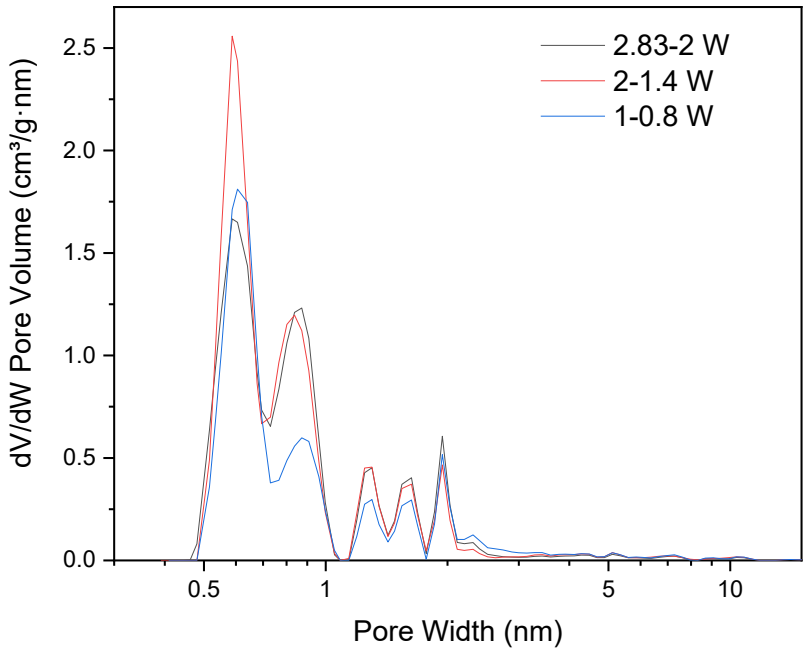

Figure C.1: Differential pore size distributions for sample 2.83-2 W, 2-1.4 W and 1-0.8 W.

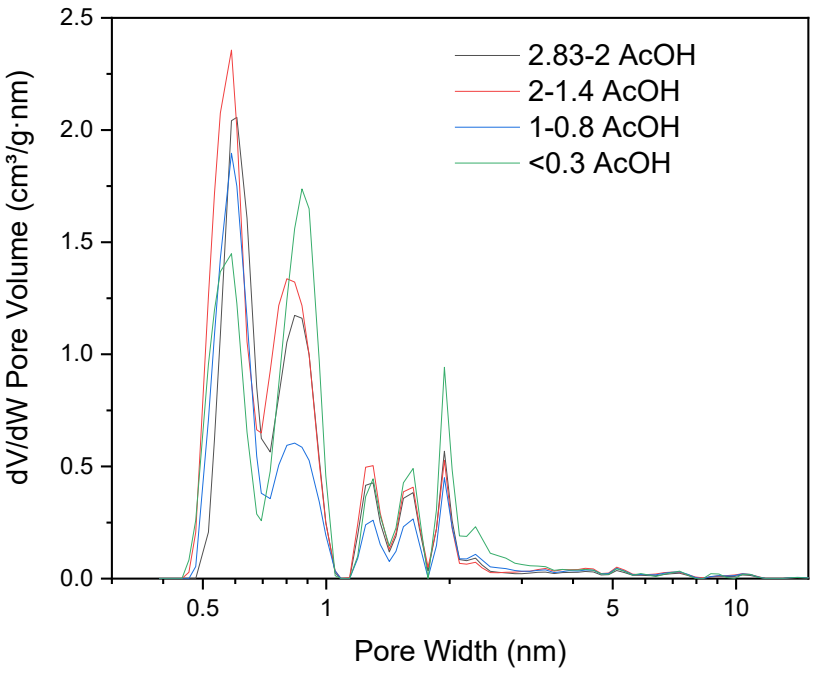

Figure C.1: Differential pore size distributions for sample 2.83-2 AcOH, 2-1.4 AcOH, 1-0.8 AcOH and <0.3 AcOH.

Appendix D

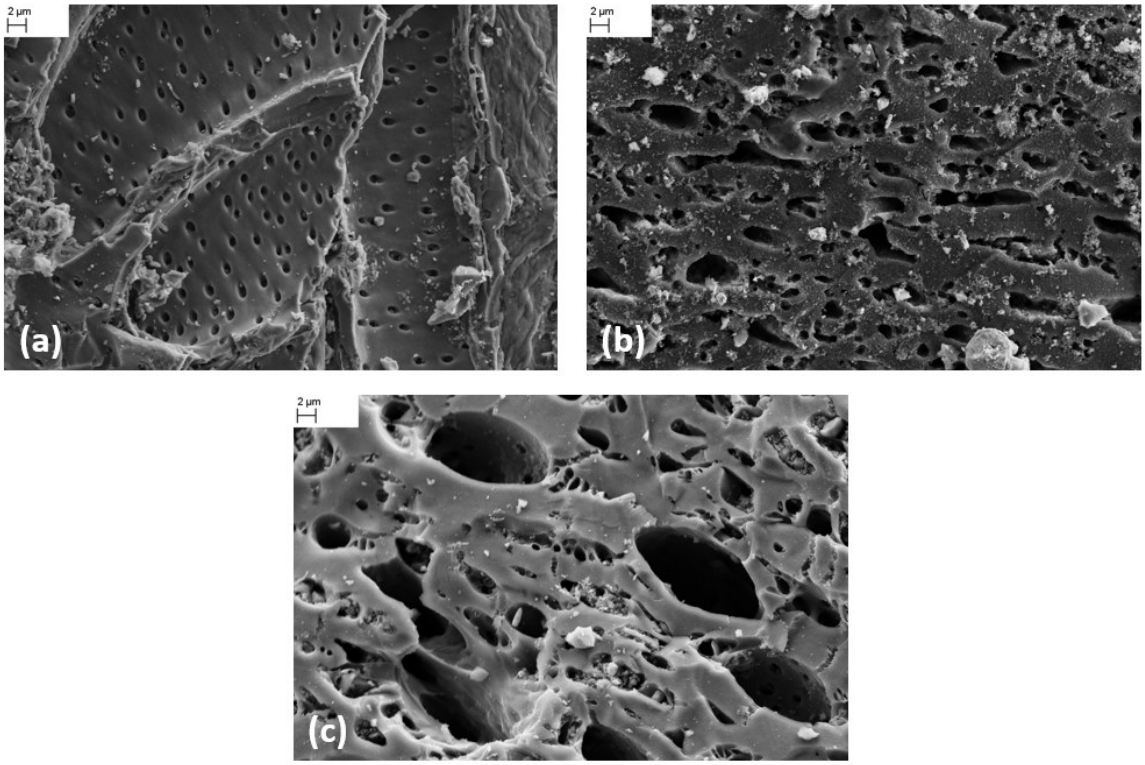

***Figure D.1*:** (a) SEM image of sample 2-1.4 Raw, 5000x; (b) SEM image of sample 2-1.4 W 5000x; (c) SEM image of sample 2-1.4 AcOH 5000x.

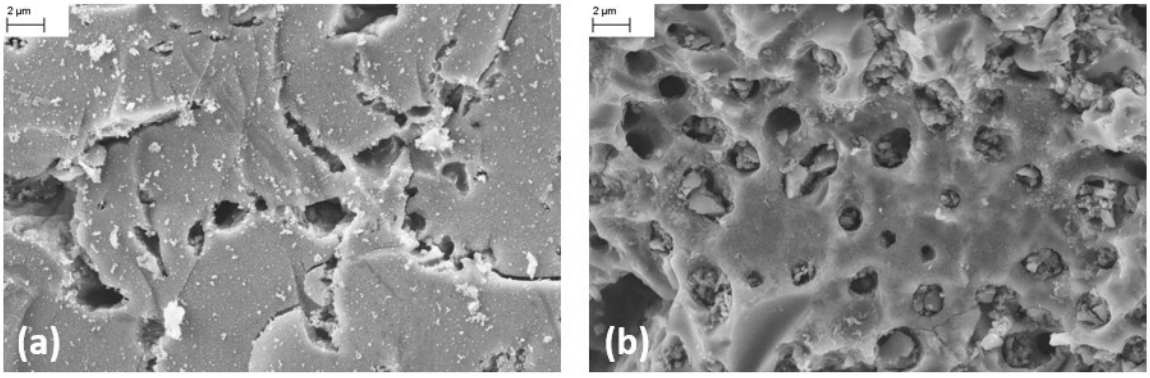

***Figure D.1*:** (a) SEM image of sample 2.83-2 Raw, 10000x; (b) SEM image of sample 2.83-2 W 10000x; (c) SEM image of sample 2.83-2 AcOH 10000x.

Appendix E

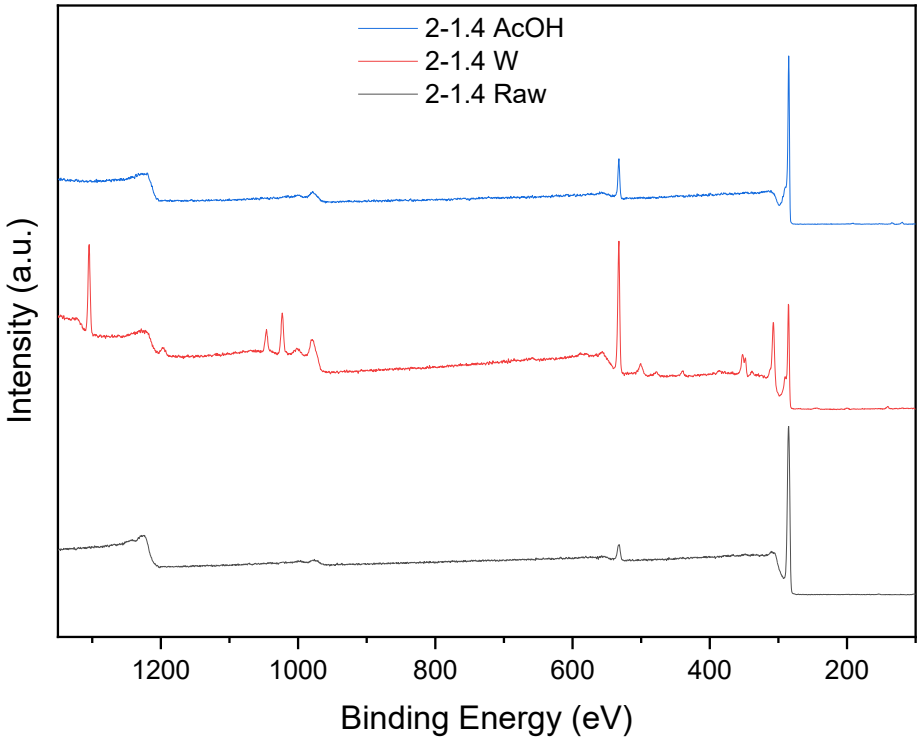

Figure E.1: XPS Survey spectra obtained for sample 2.83-2 Raw, 2-1.4 W and 2-1.4 AcOH.